

---

Electronic Thesis and Dissertation Repository

---

8-12-2022 2:30 PM

## Design and Surface Modification of Noble Metal-based Nanocatalysts

Xuchun Wang, *The University of Western Ontario*


Supervisor: Sham, Tsun-Kong, *The University of Western Ontario*

Co-Supervisor: Zhang, Qiao, *Soochow University*

A thesis submitted in partial fulfillment of the requirements for the Doctor of Philosophy degree in Chemistry

© Xuchun Wang 2022

Follow this and additional works at: <https://ir.lib.uwo.ca/etd>

 Part of the [Inorganic Chemistry Commons](#), [Materials Chemistry Commons](#), and the [Physical Chemistry Commons](#)

---

### Recommended Citation

Wang, Xuchun, "Design and Surface Modification of Noble Metal-based Nanocatalysts" (2022). *Electronic Thesis and Dissertation Repository*. 8794.

<https://ir.lib.uwo.ca/etd/8794>

This Dissertation/Thesis is brought to you for free and open access by Scholarship@Western. It has been accepted for inclusion in Electronic Thesis and Dissertation Repository by an authorized administrator of Scholarship@Western. For more information, please contact [wlsadmin@uwo.ca](mailto:wlsadmin@uwo.ca).

## Abstract

This thesis investigates approaches to modifying the surface structure of noble metal-based nanocatalysts. Noble metal-based nanocatalysts, such as Pt and Pd, play a significant role in heterogeneous catalysis due to their capabilities in activating the cleavage or formation of chemical bonds, but still suffer from the high-cost issue and unsatisfied catalytic performance due to too strong or too weak adsorption of intermediates. Considering the surface specificity of heterogeneous catalysis, Bi, a cheap metal, was used to modify the surface of Pt- and Pd-based nanocatalysts. This thesis aims to unveil the role of Bi in improving their catalytic performance from both experimental and theoretical perspectives.

In methanol electrooxidation reaction, Pt-based electrocatalysts suffer from the CO-poisoning issue due to the intrinsic strong adsorption of CO at Pt active sites. To alleviate the CO-poisoning effect, Bi was used to modify the Pt catalysts by an electrochemical reconstruction strategy. It was found that the bismuth hydroxide species formed on the Pt surface can efficiently weaken the CO adsorption while strengthening the OH adsorption at Pt sites. Following, a PtBi model catalyst with a PtBi surface alloy and a Pt-rich core was contrived to study the role of Bi in improving the methanol electrooxidation on Pt. Combining electrochemistry and spectroscopy characterizations, it was confirmed that Bi-modified Pt catalysts can completely inhibit the CO-pathway while enhancing the formate-pathway, thereby circumventing the CO-poisoning effect. The key role of Bi is enriching OH adsorbates on the catalyst surface, and the competitive adsorption between CO and OH adsorbates switches the intermediate from CO to formate, which even overwhelms the electronic effect brought by alloying Bi with Pt. More importantly, we have successfully extended this concept to modify the commercial Pt/C catalyst and realize its facile and large-scale production by a microwave-assisted method. This work deepens the understanding of the CO-poisoning issue and offers new opportunities for the design and practical production of CO-tolerance electrocatalysts in an industrial orientation

In selective hydrogenation of propyne, the over-hydrogenation occurring on Pd catalysts is blamed for the poor selectivity toward propene. Herein, a PdBi surface alloy structural model, by tuning the deposition rate of Bi atoms relative to the atomic interdiffusion rate at

the interface, realizes a continuous modulation of the electronic structure of Pd. Using advanced X-ray characterization techniques, we provide a precise depiction of the electronic structure of the PdBi surface alloy. As a result, the PdBi catalysts show enhanced propene selectivity compared with the pure Pd catalyst in the selective hydrogenation of propyne. The prevented formation of saturated  $\beta$ -hydrides in the subsurface layers and weakened propene adsorption on the surface contribute to the high selectivity. This work emphasizes the in-depth understanding of the electronic properties of surface alloy structure and underlies the study of the electronic structure-performance relationship in bimetallic catalysts.

## Keywords

Bimetallic, platinum, palladium, bismuth, surface alloy, methanol oxidation, selective hydrogenation, electrochemical reconstruction, interatomic diffusion, synchrotron, X-ray absorption spectroscopy, X-ray photoelectron spectroscopy, infrared absorption spectroscopy

## Summary for Lay Audience

Noble metals (such as platinum and palladium) play great roles in present life, especially in the catalysis field. However, their widespread applications are still facing the challenges of high cost and unsatisfied catalytic performance. Alloying noble metals with a second cheap metal is a solution to address these issues. Given chemical reactions take place on the surface of catalysts, directly modifying the surface properties of catalysts is a promising strategy to enhance their catalytic performance. However, methods of direct surface modification are lacking, and mechanistic study is not enough to explain how the second metal works.

In this thesis, bismuth, a cheap metal, was used to modify the surface of platinum and palladium by various methods, including the electrochemical reconstruction method and the seed-growth method. Bismuth-modified platinum and palladium were tested in the methanol electrooxidation and selective hydrogenation of propyne reactions, respectively. Combining advanced synchrotron X-ray techniques and laboratory characterizations, Systematic studies were carried out to elucidate the role of bismuth in each case and build reliable a structure-performance relationship.

As a result, in the methanol electrooxidation reaction, bismuth induces the competitive adsorption of hydroxyl (OH) and poisoning intermediate (carbon monoxide, CO), resulting in the reaction switching from the CO-pathway to the formate-pathway. This concept has even been extended to modify commercial platinum catalysts with a microwave-assisted method, showing great potential in practical applications. In the selective hydrogenation of propyne, the electronic structure of palladium is continuously tuned by bismuth. The palladium-bismuth surface alloy provides a good structure model for building a reliable structure-performance relationship.

## Co-Authorship Statement

Chapter 3 contains materials from a previously published manuscript. Dr. Tsun-Kong Sham and Dr. Qiao Zhang are co-authors, and they played a major role in revising the content presented in this thesis.

In Chapter 3, the density functional theoretical simulations were conducted by Dr. Miao Xie and Dr. Tao Cheng, Soochow University, China.

In Chapter 4, the in situ infrared absorption spectroscopy measurements were performed by Xingyu Ma who is supervised by Dr. Yaoyue Yang, Southwest Minzu University, China. The PtBi nanoparticles were synthesized by Yu Liu who is supervised by Dr. Qiao Zhang, Soochow University, China

In Chapter 5, the catalytic performance test and temperature-programmed desorption of hydrogen measurements were conducted by Mingyu Chu, Soochow University, China. The density function theoretical simulation was conducted by Mengwen Wang who is supervised by Dr. Tao Cheng, Soochow University.

Technical support with synchrotron X-ray experiments was provided by the following people: Dr. Mohsen Shakouri and Dr. Qunfeng Xiao (SXRMB, CLS), Dr. Zou Finfrock and Dr. Debora Meira (Sector 20, APS), Dr. Lo-Yueh Chang (41A, TPS), and Dr. Chih-Wen Pao (44A, TPS).

## Acknowledgments

First of all, I would like to thank Dr. Qiao Zhang and Dr. Tsun-Kong Sham for guiding me in my four-year doctoral study. As my supervisor from Soochow University, Dr. Qiao Zhang leads me into the world of science. He is not only a supervisor whom I can ask for professional suggestions but also a friend with whom I can seek spiritual support. Under his guidance, I started my research career and got the chance to see the world in a different way. It is so nice to have Dr. Qiao Zhang as my supervisor, and thanks are never enough for his academic and mental support. It was also because of him that I met Dr. Tsun-Kong Sham, my supervisor from the University of Western Ontario. I would like to express my most sincere thanks to Dr. Tsun-Kong Sham. As a super expert, T.K. opens the synchrotron world for me. Under his guidance, I get the chance to gain lots of experimental and theoretical knowledge of synchrotron techniques. T.K. has always been supportive of us attending conferences and communicating with brilliant people around the world. It is a great honor to work with Dr. Qiao Zhang and Dr. Tsun-Kong Sham.

Next, I would like to thank my current and former group members: Dr. Yun-Mui Yiu, Dr. Zhiqiang Wang, Dr. Mohammad Norouzi Banis, Dr. Madalena Sophia Kozachuk, Dr. Jinxing Chen, Dr. Yong Xu, Dr. Muhan Cao, Dr. Fenglei Lyu, Dr. Xiaolei Yuan, Dr. Lei Chen, Dr. Di Yang, Dr. Huicheng Hu, Dr. Min Chen, Dr. Qixuan Zhong, Dr. Linzhong Wu, Mr. Yu Liu, Ms. Pengli Li, Mr. Qi pan, Mr. Mingyu Chu, Ms. Xiaojing Jiang, Mr. Jin Gong, Mr. Wenhao Guan, Mr. Yong Zhang, Mr. Jianian Chen, Ms. Jun Liu, Ms. Shuhua Chen, Mr. Yinghua Qiu, Mr. Jie Fu, Dr. Weihan Li, Dr. Ms. Minsi Li, Ms. Lu Yao, Dr. Xuejie Gao, Dr. Shumin Zhang, Dr. Yipeng Sun, Mr. Zhiliang Dong, Mr. Jiamin Fu, Ms. Bingyu Dong, Mr. Jiabin Xu, Mr. Ali Feizabadi, Dr. Jiwei Wang, Dr. Fei Sun, and Mr. Congyang Zhang.

Following, I want to thank the technical support from a group of people: Dr. Mohsen Shakouri Dr. Qunfeng Xiao from CLS; Dr. Zou Finfrock, and Dr. Debora Meira from APS; Dr. Lo-Yueh Chang and Dr. Chih-Wen Pao from TPS.

I also want to thank our cooperators: Dr. Tao Cheng, Dr. Yaoyue Yang, Dr. Yujian Xia, Dr. Miao Xie, Dr. Hao Yang, Ms. Xingyu Ma, and Ms. Mengwen Wang.

Research at the Soochow University is supported by the National Natural Science Foundation of China, the Natural Science Foundation of Jiangsu Province the Jiangsu Province High-Level Talents, and the China Postdoctoral Science Foundation. the 111 Project, Collaborative Innovation Center of Suzhou Nano Science and Technology (NANO-CIC), and the Priority Academic Program Development of Jiangsu Higher Education Institutions (PAPD). Research at the University of Western Ontario is supported by NSERC, CFI, OIT, OMRI, and CRC (TKS). CLS is supported by CFI, NSERC, CHIR, NRC, and the University of Saskatchewan. I acknowledge the receipt of support from the CLS Graduate and PostDoctoral Student Travel Support Program. This research used resources of the Advanced Photon Source, a U.S. Department of Energy (DOE) Office of Science User Facility operated for the DOE Office of Science by Argonne National Laboratory under Contract No. DEAC02 06CH11357, Taiwan Light Source, Taiwan Photon Source, and the Canadian Light Source and its funding partners.

Last but not least, I would like to thank my parents for their unconditional support during my graduate study, and my dear wife, Ms. Shuang Chen, for her company and spiritual support. I would also like to thank my all friends in China and Canada for their encouragement and support.

# Table of Contents

Abstract.....	ii
Summary for Lay Audience.....	iv
Co-Authorship Statement.....	v
Acknowledgments.....	vi
Table of Contents.....	viii
List of Abbreviations.....	xiii
List of Tables.....	xv
List of Figures.....	xvi
Chapter 1.....	1
1 Introduction.....	1
1.1 Introduction to the noble metal based-nanocatalysts.....	1
1.2 Strategies of surface modification toward noble metal-based nanocatalysts.....	2
1.2.1 Electrochemical reconstruction.....	2
1.2.2 Epitaxial growth.....	4
1.2.3 Modifications based on the interfacial diffusion of atoms.....	6
1.3 Applications.....	9
1.3.1 Direct methanol fuel cells.....	9
1.3.2 Selective hydrogenation of alkynes.....	12
1.4 Thesis objectives.....	14
1.5 Thesis outline.....	15
1.6 References.....	15
Chapter 2.....	21
2 Synchrotron Instruments.....	21
2.1 Synchrotron overview.....	21



2.2	Synchrotron Facilities .....	23
2.2.1	Canadian Light Source (CLS).....	23
2.2.2	Advanced Photon Source (APS).....	23
2.2.3	Taiwan Light Source (TLS) and Taiwan Photon Source (TPS) .....	23
2.3	Beamlines.....	24
2.3.1	Beamline Sector 20-BM at APS .....	24
2.3.2	Soft X-ray microcharacterization beamline (SXRMB) at CLS .....	24
2.3.3	Beamline sector 24A1 at TLS.....	25
2.3.4	Beamline sector 44A at TPS .....	26
2.4	Synchrotron X-ray techniques .....	26
2.4.1	X-ray absorption spectroscopy (XAS).....	26
2.4.2	Synchrotron X-ray photoelectron spectroscopy (XPS).....	31
2.5	References .....	33
Chapter 3.....		35
3	Bismuth Oxyhydroxide-Pt Inverse Interface for Enhanced Methanol Electrooxidation Performance .....	35
3.1	Introduction.....	35
3.2	Experimental section.....	37
3.2.1	Chemicals.....	37
3.2.2	Synthesis of Pt <sub>2</sub> Bi nanoparticles .....	37
3.2.3	Characterizations.....	38
3.2.4	Electrochemical tests .....	38
3.2.5	CO-stripping experiments.....	39
3.2.6	DFT simulations.....	39
3.2.7	Fourier transform (FT) and Wavelet transform (WT) of EXAFS .....	40
3.3	Results and discussion .....	41

3.3.1	DFT simulations.....	41
3.3.2	Morphology and composition studies.....	42
3.3.3	Electronic structure study .....	44
3.3.4	Local structure study.....	46
3.3.5	CO resistance tests .....	48
3.3.6	Electrochemical tests .....	50
3.4	Conclusions.....	52
3.5	Reference .....	53
Chapter 4.....		58
4	The Role of Bismuth in Suppressing the CO-poisoning in Alkaline Methanol Electrooxidation: Switching the Reaction from CO to Formate Pathway .....	58
4.1	Introduction.....	58
4.2	Experimental section.....	59
4.2.1	Chemicals.....	59
4.2.2	Synthesis of Pt NPs.....	60
4.2.3	Synthesis of Bi-modified Pt catalysts .....	60
4.2.4	Synthesis of Bi-modified commercial Pt/C catalysts (PtBi/C).....	60
4.2.5	Characterizations.....	61
4.2.6	Data analysis of XAS spectra .....	61
4.2.7	Catalytic performance tests.....	61
4.2.8	CO-stripping experiments.....	62
4.2.9	In situ electrochemical Fourier-transform infrared (FTIR) absorption spectroscopy.....	62
4.3	Results and discussion .....	63
4.3.1	Morphology and crystalline structure study .....	63
4.3.2	Electronic structure study .....	66
4.3.3	Electrochemical tests .....	70

4.3.4	In situ FTIR results .....	73
4.3.5	Reaction pathways .....	76
4.3.6	Extension of the concept.....	78
4.4	Conclusions.....	78
4.5	References.....	79
Chapter 5	.....	84
5	Unveiling the Local Structure and Electronic Properties of PdBi Surface Alloy for Selective Hydrogenation of Propyne .....	84
5.1	Introduction.....	84
5.2	Experimental section.....	85
5.2.1	Chemicals.....	85
5.2.2	Synthesis of Pd cubes.....	86
5.2.3	Synthesis of PdBi nanoparticles with a surface alloy structure .....	86
5.2.4	Synthesis of PdBi nanoparticles with a surface island structure.....	86
5.2.5	Characterization .....	86
5.2.6	Catalytic evaluation of supported Pd and PdBi catalysts.....	87
5.2.7	XPS spectrum fitting.....	88
5.2.8	XAFS data analysis.....	88
5.2.9	DFT simulations.....	89
5.3	Results and discussion .....	89
5.3.1	Growth mechanism .....	89
5.3.2	Morphology and composition studies.....	90
5.3.3	Crystalline structure study .....	94
5.3.4	Electronic structure study .....	94
5.3.5	Local structure study.....	97
5.3.6	Selective hydrogenation of propyne .....	102

5.3.7 Simulation results.....	104
5.4 Conclusions.....	106
5.5 References.....	107
Chapter 6.....	112
6 Conclusions and Future Work.....	112
6.1 Conclusions.....	112
6.2 Future work.....	113
Appendices.....	114
Appendix A: Copyright release from ACS publications.....	114
Curriculum Vitae .....	115

## List of Abbreviations

APS	Advanced Photon Source
APXPS	Ambient pressure X-ray photoelectron spectroscopy
ATR	Attenuated total reflection
BE	Binding energy
CLS	Canadian light source
CN	Coordination number
DEG	Diethylene glycol
DFT	Density functional theory
DMFC	Direct methanol fuel cell
EDS	Energy dispersive spectroscopy
EG	Ethylene glycol
EXAFS	Extended X-ray absorption fine structure
FID	Flame ionization detector
FW	Fran van der Merve
FWHM	Full width at half maximum
FT	Fourier transform
FTIR	Fourier-transform infrared spectroscopy
FY	Fluorescence yield
HAADF	High-angle annular dark field
HER	Hydrogen evolution reaction
HRTEM	High-resolution transmission electron microscopy
ICP-AES	Inductively coupled plasma-atomic emission spectroscopy
ICP-OES	Inductively coupled plasma-optical emission spectroscopy
IMFP	Inelastic mean free path
IR	Infrared spectroscopy
IRAS	Infrared reflection absorption spectroscopy
KE	Kinetic energy
MOR	Methanol oxidation reaction
NEXAFS	Near edge X-ray absorption fine structure

NPs	Nanoparticles
NSRRC	National Synchrotron Radiation Research Center
ORR	Oxygen reduction reaction
PVP	Polyvinylpyrrolidone
RF	Radiofrequency
RHE	Reversible hydrogen electrode
SCE	Saturated calomel electrode
SEIRA	Surface-enhanced infrared absorption
SHE	Standard hydrogen electrode
STY	Space time yield
SXRMB	Soft X-ray micro-characterization beamline
TCD	Thermal conductivity detector
TEM	Transmission electron microscope
TEY	Total electron yield
TLC	Taiwan light source
TMAB	Tetramethylammonium bromide
TPD	Temperature programmed deposition
TPD	Temperature programmed desorption
TPS	Taiwan photon source
TRXEOL	Time-resolved X-ray excited optical luminescence
UHV	Ultra-high vacuum
VW	Volmer-Weber
WE	Working electrode
WL	Whiteline
WT	Wavelet transform
XAFS	X-ray absorption fine structure
XAS	X-ray absorption spectroscopy
XPS	X-ray photoelectron spectroscopy
XRD	X-ray diffraction

## List of Tables

Table 1-1. Chemical and electrochemical data of various fuels. Adapted with permission from reference [44]. Copyright 2006 Universities Press (India) Private Ltd. ....	9
Table 3-1 Adsorption properties of CO and OH species on Pt sites of Pt <sub>2</sub> Bi_A based on DFT calculation. ....	41
Table 3-2. A summary of the activities of MOR electrocatalysts in alkaline electrolytes reported in previous literature. ....	52
Table 4-1. The molar ratio of Pt and Bi in precursors and in PtBi nanoparticles determined by various characterization techniques. ....	67
Table 4-2. Fitting result of EXAFS at Pt L <sub>3</sub> -edge. ....	69
Table 4-3. Band assignments from the ATR-SEIRAS and IRAS spectra displayed in Figure 4-8. ....	76
Table 5-1. XPS fitting results of Pd cube and PdBi samples. ....	96
Table 5-2. EXAFS fitting results in R space at Pd K-edge and Bi L <sub>3</sub> -edge. ....	101

## List of Figures

- Figure 1-1. a) The scheme of electrochemical-induced species evolution on Pd@Fe<sub>3</sub>O<sub>4</sub> electrocatalysts (left) and the influence of FeO<sub>x</sub>(OH)<sub>2-2x</sub> coverage on the catalytic performance in HER (right). Reproduced with permission from reference [22]. Copyright 2017 Wiley-VCH. b) The scheme of electrochemical induced lattice strain in dealloyed surface (left) and its influence on the catalytic performance in ORR. The blue and red lines are PtCu bimetallic particles annealing at 950 °C and 800 °C, respectively. The black line is the theoretical trend based on DFT calculations. Reproduced with permission from reference [23]. Copyright 2010 Springer Nature. .... 3
- Figure 1-2. a) Schematic illustration of crystal growth modes, including Frank-van der Merve, Volmer-Weber, and Stranski-Krostanov growth. b) Schematic dependence of the film chemical potential on the film thickness in the number of monolayers for the three modes of growth. Reproduced with permission from reference [27]. Copyright 2002 American Physical Society. .... 5
- Figure 1-3. a) Schematic illustration of the interfacial diffusion. b) Schematic illustration of alloy process of Au@Ag core-shell nanoparticles. Reproduced with permission from reference [34]. Copyright 2021 American Chemical Society. TEM images of i) Au, ii) Au@Ag, iii) Au@Ag@SiO<sub>2</sub>, and iv) AuAg alloy nanoparticles. Reproduced with permission from [37]. Copyright 2014 American Chemical Society. c) Schematic illustration of the formation of the Pd hollow nanocrystals. TEM image of i) PdP<sub>2</sub>. SEM images of ii) Pd hollow structure after one cycle and iv) Pd hollow structure after two cycles. Reproduced with permission from reference [40]. Copyright 2017 Springer Nature Publishing Group. .... 7
- Figure 1-4. a) The schematic illustration of DMFC operated with acidic electrolytes. b) The schematic illustration of DMFC operated with alkaline electrolytes. .... 10
- Figure 1-5. Reaction network for acetylene hydrogenation. Adapted with permission from reference [50]. Copyright 2015 Spring Nature. .... 13



Figure 1-6. Adsorption patterns of ethylene on Pd catalysts with different geometric structures. Adapted with permission from reference [49]. Copyright 2019 America Chemical Society.....	13
Figure 2-1. Schematic of a synchrotron. The synchrotron ring is reprinted from EPSIM 3D/JF Santarelli, Synchrotron Soleil. Copyright @ EPSIM 3D/JF Santarelli, Synchrotron Soleil. .	22
Figure 2-2. The schematic illustrations to a) multi-scattering paths and b) single-scattering path.....	28
Figure 2-3. Optical path of synchrotron X-rays at the endstation showing the three detecting modes. ....	30
Figure 2-4. Schematic illustration of the universal escape depth curve of electrons versus square root of kinetic energy. Measurements at ID32, ESRF (European Synchrotron Radiation Facility) by J. Zegenhagen. ....	32
Figure 3-1. DFT simulations of the binding free energy of CO and OH species on surfaces of pristine Pt (111) (a and c) and Pt (111) with $\text{BiO}_x(\text{OH})_y$ (b and d). ....	41
Figure 3-2. TEM images and HRTEM images of (a) $\text{Pt}_2\text{Bi}_I$ and (b) $\text{Pt}_2\text{Bi}_A$ . HAADF-STEM images and elemental mapping of (c) $\text{Pt}_2\text{Bi}_I$ and (d) $\text{Pt}_2\text{Bi}_A$ . e) EDS spectra and f) XRD patterns of $\text{Pt}_2\text{Bi}_I$ and $\text{Pt}_2\text{Bi}_A$ , respectively. ....	43
Figure 3-3. XPS spectra of $\text{Pt}_2\text{Bi}_I$ and $\text{Pt}_2\text{Bi}_A$ at a) Pt 4f and b) Bi 4f core levels. XPS spectra of c) $\text{Pt}_2\text{Bi}_I$ and d) $\text{Pt}_2\text{Bi}_A$ at O 1s core levels. ....	44
Figure 3-4. XANES spectra of a) Pt/C and b) $\text{Pt}_2\text{Bi}$ before and after electrochemical treatment at Pt $L_3$ -edge. Pt foil and $\text{PtO}_2$ are used as references. Fourier transform c) and wavelet transform d) of Pt $L_3$ -edge EXAFS of $\text{Pt}_2\text{Bi}_I$ and $\text{Pt}_2\text{Bi}_A$ with a $k^3$ weighting. Pt foil and $\text{PtO}_2$ are used as references.....	45
Figure 3-5. WT contour plots of a) $\text{Pt}_4\text{Bi}$ , b) $\text{Pt}_2\text{Bi}$ , and c) PtBi before and after activation..	47
Figure 3-6. a) XANES spectra of $\text{Pt}_2\text{Bi}_I$ and $\text{Pt}_2\text{Bi}_A$ at Bi $L_2$ -edge. Bi foil and Bi powder were used as references. b) and c) are linear combination fitting of XANES spectra of $\text{Pt}_2\text{Bi}_I$	

and Pt<sub>2</sub>Bi\_A, respectively. d) CV curves of Pt/C and Pt<sub>2</sub>Bi\_A in 1 M KOH with a scan rate of 50 mV s<sup>-1</sup>..... 48

Figure 3-7. AP-XPS spectra of a) Pt/C and b) Pt<sub>2</sub>Bi\_A at Pt 4f and c) Bi 4f core levels under three successive atmospheric conditions. 1) Ultra-high vacuum (UHV-1, olive line); 2) CO atmosphere (AP-CO, red line); 3) ultra-high vacuum (UHV-2, blue line). The incipient X-ray energy is 560 eV. CO-stripping experiments of d) Pt/C and e) Pt<sub>2</sub>Bi\_A in 1 M KOH. Scanning rate is 50 mV s<sup>-1</sup>. f) CV curves of Pt/C and Pt<sub>2</sub>Bi\_A in 1 M KOH/1 M CH<sub>3</sub>OH before and after electrochemical treatment. Scanning rate is 50 mV s<sup>-1</sup>. ..... 49

Figure 3-8. TEM images of PtBi nanoparticles with different compositions. a) Pt<sub>4</sub>Bi, b) Pt<sub>2</sub>Bi, and c) PtBi. d) XRD patterns of PtBi nanoparticles with different compositions. e) Mass activity of Pt/C, Pt<sub>4</sub>Bi, Pt<sub>2</sub>Bi, and PtBi towards MOR. f) Chronoamperogram of Pt<sub>2</sub>Bi and Pt/C in 1 M KOH/1 M CH<sub>3</sub>OH at -0.23 V vs. SCE..... 51

Figure 4-1. TEM images of a) Pt NPs and b) Pt<sub>92</sub>Bi<sub>8</sub>, respectively. c) HRTEM images of Pt<sub>92</sub>Bi<sub>8</sub>. d) Elemental mapping images of Pt<sub>92</sub>Bi<sub>8</sub>. e) Line scanning image (top) and profile (bottom) of Pt<sub>92</sub>Bi<sub>8</sub>. f) XRD patterns of Pt NPs and Pt<sub>92</sub>Bi<sub>8</sub> (left) and the zoom-in image of the (111) facet from 37° to 42° (right). ..... 64

Figure 4-2. a) TEM images and size-distribution statistics of Pt NPs, Pt<sub>92</sub>Bi<sub>8</sub>, Pt<sub>95</sub>Bi<sub>5</sub>, and Pt<sub>78</sub>Bi<sub>22</sub>. b) TEM and elemental mapping images of Pt<sub>78</sub>Bi<sub>22</sub>..... 65

Figure 4-3. XPS spectra at a) Pt and b) Bi 4f core levels. c) XNAES spectra at Pt L<sub>3</sub>-edge. The whiteline fitting of d) Pt foil, e) Pt NPs, and f) Pt<sub>92</sub>Bi<sub>8</sub> at Pt L<sub>3</sub>-edge. g) EXAFS spectra at Pt L<sub>3</sub>-edge in k space, a k<sup>2</sup> weighting is used .h) Fourier transformed EXAFS at Pt L<sub>3</sub>-edge in R space. A k<sup>2</sup> weighting is used. i) XANES spectra at Bi L<sub>2</sub>-edge. .... 67

Figure 4-4. The scheme of the PtBi structural model. .... 69

Figure 4-5. a) CV curves of Pt NPs and Pt<sub>92</sub>Bi<sub>8</sub> in 1 M KOH /1 M CH<sub>3</sub>OH at a scan rate of 50 mV s<sup>-1</sup>. b) Long-term durability measurements of Pt NPs and Pt<sub>92</sub>Bi<sub>8</sub> in 1 M KOH /1 M CH<sub>3</sub>OH at 0.81 V versus RHE. c) CV curves of Pt NPs and Pt<sub>92</sub>Bi<sub>8</sub> in 1 M KOH at a scan rate of 50 mV s<sup>-1</sup>. CO-stripping experiments performed on d) Pt NPs and e) Pt<sub>92</sub>Bi<sub>8</sub> in 1 M

KOH at a scan rate of  $50 \text{ mV s}^{-1}$ , respectively. f) CV curves of Pt NPs,  $\text{Pt}_{95}\text{Bi}_5$ ,  $\text{Pt}_{92}\text{Bi}_8$ , and  $\text{Pt}_{78}\text{Bi}_{22}$  in 1 M KOH at a scan rate of  $50 \text{ mV s}^{-1}$ ..... 70

Figure 4-6. The comparison of cyclic voltammograms of a) Pt NPs, b)  $\text{Pt}_{98}\text{Bi}_2$ , c)  $\text{Pt}_{92}\text{Bi}_8$ , and d)  $\text{Pt}_{78}\text{Bi}_{22}$  with that of references, including Bi powdering,  $\text{Bi}_2\text{O}_3$ , and  $\text{Bi}(\text{OH})_3$ . The electrolyte is 1 M KOH..... 72

Figure 4-7. CV curves of Pt NPs and  $\text{Pt}_{92}\text{Bi}_8$  in 0.1 M KOH/1 M  $\text{CH}_3\text{OH}$  under the ATR-SEIRS mode..... 74

Figure 4-8. In situ ATR-SEIRAS spectra taken on a) Pt NPs and b)  $\text{Pt}_{92}\text{Bi}_8$  in 0.1 M KOH/ 1 M  $\text{CH}_3\text{OH}$  over the potential range from 0 to 1.2 V versus RHE. In situ IRAS spectra taken on c) Pt NPs and d)  $\text{Pt}_{92}\text{Bi}_8$  in 0.1 M KOH/ 1 M  $\text{CH}_3\text{OH}$  over the potential range from 0 to 1.2 V vs. RHE. CV curves (black) and peak intensities at 1581 (blue) and  $2432 \text{ cm}^{-1}$  (red) as a function of applied potential taken on e) Pt NPs and f)  $\text{Pt}_{92}\text{Bi}_8$ , respectively..... 74

Figure 4-9. Reaction pathways of methanol oxidation on Pt NPs and PtBi catalysts in the alkaline solution..... 76

Figure 4-10. a) and b) are the TEM images of commercial Pt/C and PtBi/C, respectively. c) Elemental mapping images of PtBi/C. d) and e) are XPS spectra of Pt/C and PtBi/C at Pt and Bi 4f core levels, respectively. f) CV curves of commercial Pt/C and PtBi/C in 1 M KOH at a scan rate of  $50 \text{ mV s}^{-1}$ . g) CV curves of commercial Pt/C and PtBi/C in 1 M KOH/1 M  $\text{CH}_3\text{OH}$  at a scan rate of  $50 \text{ mV s}^{-1}$ . h) Long-term durability measurements of commercial Pt/C and PtBi/C in 1 M KOH /1 M  $\text{CH}_3\text{OH}$  at 0.81 V vs. RHE..... 77

Figure 5-1. TEM image of Pd cubes..... 90

Figure 5-2. a) The schematic illustration of epitaxial growth modes. b) and c) are the TEM and HRTEM images of  $\text{Pd}_{96.9}\text{Bi}_{3.1}$ , respectively. Insets in c) are the fast Fourier transform (top left) and zoom-in image (top right) of the selected area (red dash square), respectively. d) and e) indicate the elemental mapping images and line scanning analysis of  $\text{Pd}_{96.9}\text{Bi}_{3.1}$ , respectively. .... 91

Figure 5-3. Elemental mapping images of PdBi nanoparticles with bismuth acetate used as the precursor.....	93
Figure 5-4. a) TEM images of Pd cube, Pd <sub>98.8</sub> Bi <sub>1.2</sub> , Pd <sub>96.9</sub> Bi <sub>3.1</sub> , and Pd <sub>94.2</sub> Bi <sub>5.8</sub> . b) Elemental mapping images of Pd <sub>98.8</sub> Bi <sub>1.2</sub> , Pd <sub>96.9</sub> Bi <sub>3.1</sub> , and Pd <sub>94.2</sub> Bi <sub>5.8</sub> .....	93
Figure 5-5. a) XRD patterns (left) of PdBi samples and the zoom-in image of the selected yellow region from $2\theta = 39^\circ$ to $41^\circ$ (right). b) and c) are XPS spectra of PdBi samples at Pd 3d and Bi 4f core levels, respectively. d) Comparison of line shapes of Pd 3d peaks after aligning peaks together and ignoring the binding energy shift.....	95
Figure 5-6. XANES spectra of PdBi samples at a) Pd L <sub>3</sub> -edge, b) Pd K-edge, and c) Bi L <sub>3</sub> -edge.....	97
Figure 5-7. a) and b) are the EXAFS spectra of PdBi samples and references in k and R space, respectively. A $k^3$ weighting is used in the Fourier transform. c) The WT contour plots of the Bi-Pd model, Pd cube, Bi powder, and PdBi samples. A $k^3$ weighting is used. ....	99
Figure 5-8. WT contour plots of PdBi samples and references.....	100
Figure 5-9. TEM images of a) Pd/Al <sub>2</sub> O <sub>3</sub> , b) Pd <sub>98.8</sub> Bi <sub>1.2</sub> /Al <sub>2</sub> O <sub>3</sub> , c) Pd <sub>96.9</sub> Bi <sub>3.1</sub> /Al <sub>2</sub> O <sub>3</sub> , and d) Pd <sub>94.2</sub> Bi <sub>5.8</sub> /Al <sub>2</sub> O <sub>3</sub> , respectively. e) The FTIR spectra of PVP, $\gamma$ -Al <sub>2</sub> O <sub>3</sub> , and Pd <sub>96.9</sub> Bi <sub>3.1</sub> /Al <sub>2</sub> O <sub>3</sub> .....	102
Figure 5-10. Catalytic performance of selective hydrogenation of propyne on various PdBi catalysts. a) The histogram of propyne conversion, propene, and propane selectivity over different PdBi samples. b) The histogram of propene STY over different PdBi samples. c) and d) The histogram of propyne conversion, propene and propane selectivity at different temperatures on Pt <sub>96.9</sub> Bi <sub>3.1</sub> /Al <sub>2</sub> O <sub>3</sub> and Pd cube/Al <sub>2</sub> O <sub>3</sub> , respectively. e) Stability test of Pt <sub>96.9</sub> Bi <sub>3.1</sub> /Al <sub>2</sub> O <sub>3</sub> over 24 hours on stream. Reaction conditions: C <sub>3</sub> H <sub>6</sub> /H <sub>2</sub> /N <sub>2</sub> = 6/15/44 mL/min, T = 60 °C except when investigating the influence of reaction temperature, P = 0.1 MPa and catalyst weight = 5 mg.....	103
Figure 5-11. a) DFT simulations of dissociative adsorption energy of hydrogen and adsorption energy of propene on Pd (100) and PdBi (100) surfaces, respectively. b) H <sub>2</sub> -TPD	

curves of Pd cube and PdBi samples. Energy profile of the first hydrogenation step c) and the second hydrogenation step d) on Pd (100) and PdBi (100) surfaces, respectively..... 105

# Chapter 1

## 1 Introduction

### 1.1 Introduction to the noble metal based-nanocatalysts

Noble metal-based catalysts play a significant role in the present life, especially in the fields related to petrochemistry, pharmaceuticals, transportation, environmental remediation, etc.<sup>1-5</sup> In parallel to their successful applications, the fundamental understanding of catalytic processes is also important to further improve their catalytic performance without compromising the costs and environments. However, most industrial catalysts currently in use consist of small metal particles with poor uniformities in sizes, shapes, and compositions, which cannot provide a proper model for fundamental studies. Over the past several decades, unprecedented advancements in nanotechnology makes it possible to controllably prepare nanocrystals with specific sizes, morphologies, facets, and components, paving the way both for the fundamental studies and design of highly efficient catalysts.<sup>5,6</sup> Noble metal-based nanocatalysts, such as Pt, Pd, Rh, Ru, Ir, Ag, and Au, have received extensive investigation owing to their unique physiochemical properties and great potential in electrocatalysis, thermal catalysis, and photocatalysis.<sup>2,7,8</sup> However, their widespread applications are limited by their scarce distribution on earth and high price. What is more, a single noble metal sometimes cannot achieve a satisfying performance.<sup>9,10</sup> For example, their specific electronic properties often induce too strong or too weak adsorption of intermediates, resulting in the deactivation of catalysts or poor selectivity toward targeted products.<sup>11</sup> Additionally, a synergy between metals sometimes is required to complete one reaction process by a bifunctional effect, i.e., each metal has its role.<sup>12</sup> Therefore, combining noble metals with cheap metals or metal oxides/hydroxides would be a good choice to address the above-mentioned issues.<sup>13</sup> The cheap additives can not only reduce the usage of noble metals but also tune their electronic properties or get involved in the reaction directly, thereby improving the catalytic performance. For heterogeneous catalysts, the reaction exclusively occurs on the catalyst surface, of which the catalytic performance is closely linked to the structural and electronic properties of the catalyst surface. Realizing the modification of the surface

properties of noble metal-based nanocatalysts using cheap additives will be a promising way to design highly efficient catalysts.

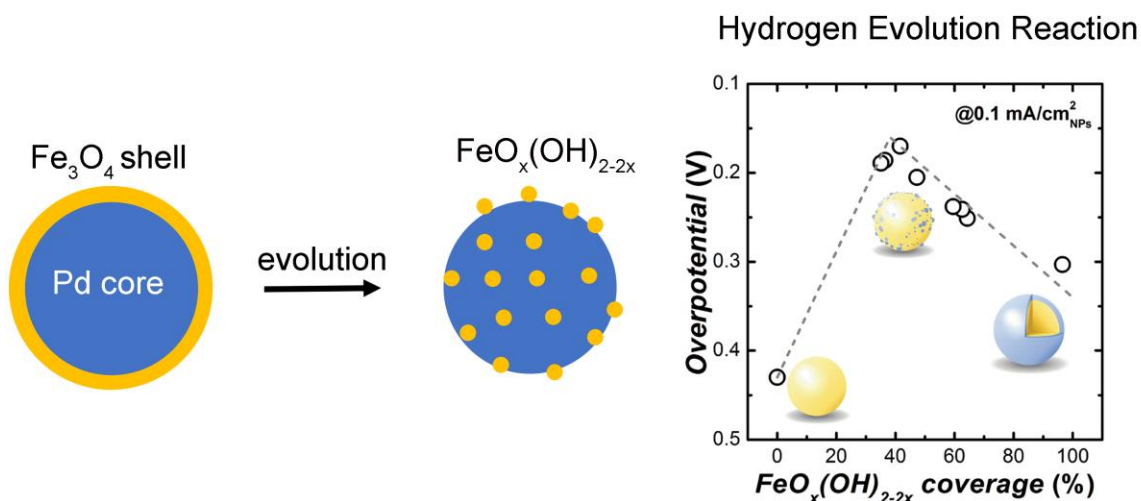
## 1.2 Strategies of surface modification toward noble metal-based nanocatalysts.

### 1.2.1 Electrochemical reconstruction

With recent developments of in situ and operando characterization techniques, it is extensively observed that catalysts undergo structural reconstruction when switching from non-working to working conditions, especially in the electrocatalysis field.<sup>14-16</sup> Since electrocatalysis usually is related to the conversion of molecules under applied potential, experimentally much more negative or positive potentials compared to the equilibrium potentials are often applied to obtain scalable molecule conversions due to nonideal conditions and large kinetics barriers.<sup>17,18</sup> It is found that the applied potentials for driving the corresponding molecule conversions are overlapping with the redox potentials of the employed electrocatalysts to some extent.<sup>19,20</sup> It is the electrically driven oxidation or reduction processes that induce the structural reconstruction of electrocatalysts.<sup>21</sup> As the catalytic reaction exclusively takes place on the surface of electrocatalysts, the structural properties of the catalytic surface mainly determine the catalytic behaviors, including adsorption, activation, and desorption, which provides the possibility to improve the catalytic performance by the surface modification brought by the electrochemical reconstruction.

Due to the unique oxidative or reductive environment endowed by the applied potentials, the surface species sometimes are subjected to the transformation from the relatively inert to active species. Here, we take the Pd@Fe<sub>3</sub>O<sub>4</sub> electrocatalyst for hydrogen evolution reaction (HER) as an example (**Figure 1-1a**).<sup>22</sup> HER is a multiple-step reaction, containing the water dissociation and hydrogen formation steps. Upon electrochemical cycling, the rigid Fe<sub>3</sub>O<sub>4</sub> shell will evolve into Fe<sub>x</sub>(OH)<sub>2-2x</sub> islands, responsible for facilitating the dissociation of water molecules, while the exposed Pd sites contribute to the formation of hydrogen. A subtle balance between the water dissociation rate and the

### a) Creating New Species



### b) Inducing Lattice Strain

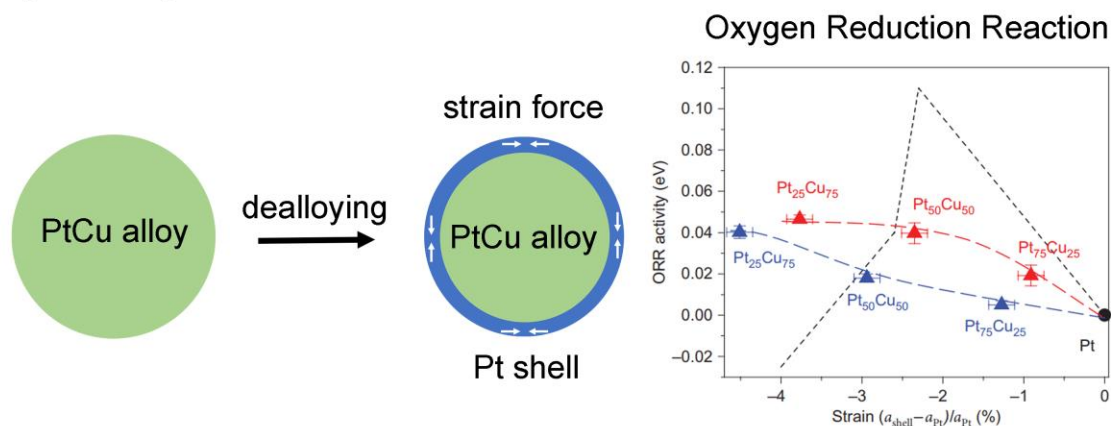


**Figure 1-1. a) The scheme of electrochemical-induced species evolution on Pd@Fe<sub>3</sub>O<sub>4</sub> electrocatalysts (left) and the influence of FeO<sub>x</sub>(OH)<sub>2-2x</sub> coverage on the catalytic performance in HER (right). Reproduced with permission from reference [22]. Copyright 2017 Wiley-VCH. b) The scheme of electrochemical induced lattice strain in dealloyed surface (left) and its influence on the catalytic performance in ORR. The blue and red lines are PtCu bimetallic particles annealing at 950 °C and 800 °C, respectively. The black line is the theoretical trend based on DFT calculations. Reproduced with permission from reference [23]. Copyright 2010 Springer Nature.**



hydrogen formation rate is necessary to reach the highest overall efficiency, which can be achieved by tuning the cycling numbers.

Besides, “dealloying” is another phenomenon brought by the electrochemical treatment, in which the preferential dissolution (removal) of the electrochemically more reactive component takes place from a bimetallic alloy that consists of a less reactive and more reactive metal.<sup>23</sup> This kind of dealloying effect results in the formation of a thin metal layer on the alloy core (**Figure 1-1b**). The lattice mismatch between the surface metal layer and alloy core will induce strain force in the surface layers (compressed or expanded lattice parameters). The lattice strain will impact the valence band structure by changing the overlapping degree of valence orbitals of atoms, and further influence the adsorption behaviors of adsorbates. For example, the electrochemical-induced dissolution of Cu from the PtCu alloy gives rise to the formation of a Pt thin layer on the surface.<sup>24</sup> The compressive strain provided by the PtCu core induces a shift of the electronic band structure of Pt away from the Fermi level and weakens the chemisorption of oxygenated species in the oxygen reduction reaction (ORR). More importantly, the dealloying degree can be finely regulated experimentally, in other words, it is feasible to tune the electronic properties of the catalyst surface by this dealloying strategy, further improving the catalytic performance.

### 1.2.2 Epitaxial growth

Epitaxial growth, which refers to the deposition of crystalline material on the well-defined surface of a crystalline substrate,<sup>25</sup> is another efficient way to directly modify the surface properties of catalysts. It enables a high level of control over the composition, relative arrangement of nanostructures, crystal phases, exposed facets, and interfaces.<sup>26</sup> Typically, as shown in **Figure 1-2a**, the seed-based epitaxial growth follows the Frank-van der Merve growth mode (FM, layer-by-layer growth), Volmer-Weber growth mode (VW, island-like growth), or Stranski-Krostanov growth mode (SK, a combination of FW and VW).<sup>27</sup> Thermodynamic considerations are a necessary step for understanding the process, which can be described as the chemical potential of the system (Eq. 1.1),

$$\mu(n) = \mu_{3D}^0 + [E_{aa} - E_{ab}(n)] = \mu_{3D}^0 + E_{aa}\varphi \quad (1.1)$$

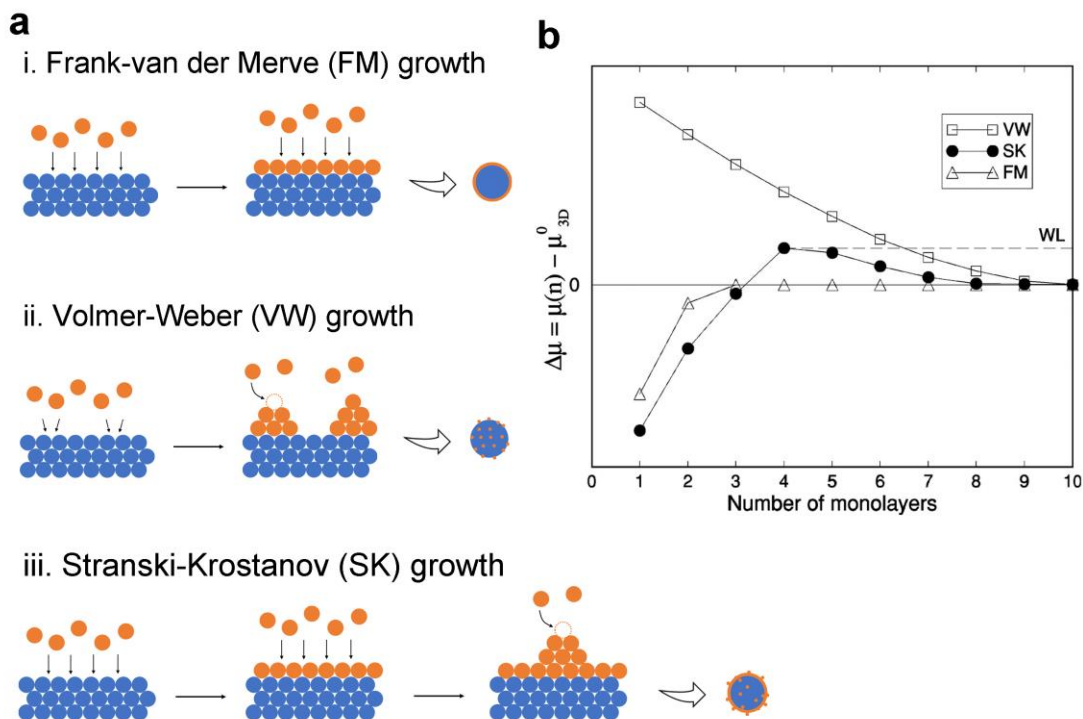


**Figure 1-2. a) Schematic illustration of crystal growth modes, including Frank-van der Merve, Volmer-Weber, and Stranski-Krostanov growth. b) Schematic dependence of the film chemical potential on the film thickness in the number of monolayers for the three modes of growth. Reproduced with permission from reference [27]. Copyright 2002 American Physical Society.**

where  $\mu_{3D}^0$  is the bulk chemical potential of the core material and  $E_{aa}$  and  $E_{ab}$  are the interatomic energies per atom describing the adhesion strength of the newly formed atoms on the same crystal (a) and the metallic seed (b), respectively. The adhesion energy  $E_{ab}$  includes in itself the thickness distribution of the strain energy and the attenuation of the binding with the bulk.  $\varphi = 1 - E_{ab}/E_{aa}$  is the adhesion parameter which accounts for the overgrowth on the bulk crystal. In the two limiting cases of VW ( $0 < \varphi < 1$ ) and FW growth ( $\varphi \leq 0$ ),  $\Delta\mu$  tends asymptotically to zero from above and from below with increasing the film thickness, respectively, but changes its sign in the case of SK growth (**Figure 1-2b**). As long as  $\mu(n) < \mu_{3D}^0$ , i.e.,  $E_{aa} < E_{ab}$ , the foreign metal prefers to deposit on the bulk following the FW growth layer by layer. When  $\mu(n) > \mu_{3D}^0$ , i.e.,

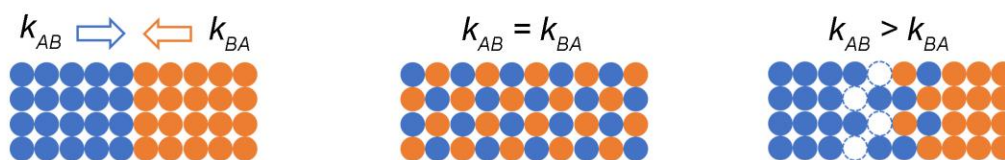
$E_{aa} > E_{ab}$ , islands will form on the bulk crystal following the VW growth. Here, the SK growth is the combination of the FW and VW, in which the foreign metal firstly deposits on the bulk crystal layer by layer. However, lattice dislocations will take place with accumulating the lattice strain caused by the lattice misfit between the overgrowth metal and the bulk crystal, which will result in the decrease of the interface energy and then switch the growth from the FW to VW.<sup>28</sup> Based on these theoretical models, numerous noble metal-based heterogeneous nanostructures have been prepared, from core-shell structure<sup>29,30</sup> to island-like structure<sup>31,32</sup> and to highly branched superstructures,<sup>33</sup> being successfully applied to various fields.

### 1.2.3 Modifications based on the interfacial diffusion of atoms

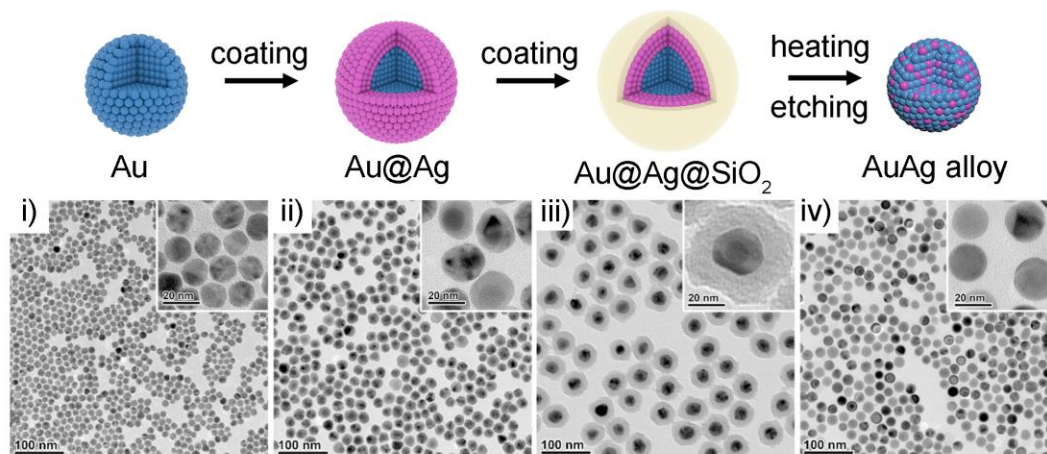
The interfacial diffusion of atoms has received extensive investigation because of its capability to modify the composition of the surface and the bulk of nanoparticles, thereby significantly changing their properties.<sup>34</sup> Finely tuning the interfacial diffusion can offer great opportunities to meet the requirements of various practical applications. As schematically shown in **Figure 1-3a**, the interfacial diffusion will take place at the interface of metals A and B under certain conditions. An equal interfacial diffusion rate of A and B will lead to the formation of an alloy or intermetallic structure. However, it is rare for two metals to have the same diffusion coefficient in each other. Once the diffusion rate of one metal over the other, the flux of atoms from the metal with the higher diffusion rate will exceed its counterpart. The net flux of atoms from the metal with the higher diffusion rate into the one with the lower diffusion rate must be balanced with the vacancies left behind, which results in the motion of the interface. This phenomenon induced by the difference in diffusion rates of the metal atoms is referred to as the Kirkendall effect.<sup>35,36</sup>

The interfacial diffusion of atoms is quite common and can be triggered by various factors, thus offering the possibility to optimize the geometrical and electronic properties of the surface structure of nanocatalysts. High temperature is one of the factors that trigger the interfacial diffusion of atoms. Annealing at high temperatures can induce extensive interdiffusion of two miscible metals and guarantee the homogeneity of the alloy, which usually shows beneficial properties that its single components do not

### a) Scheme of the Interfacial Diffusion



### b) Thermally Driven Interfacial Diffusion



### c) Chemically Driven Interfacial Diffusion

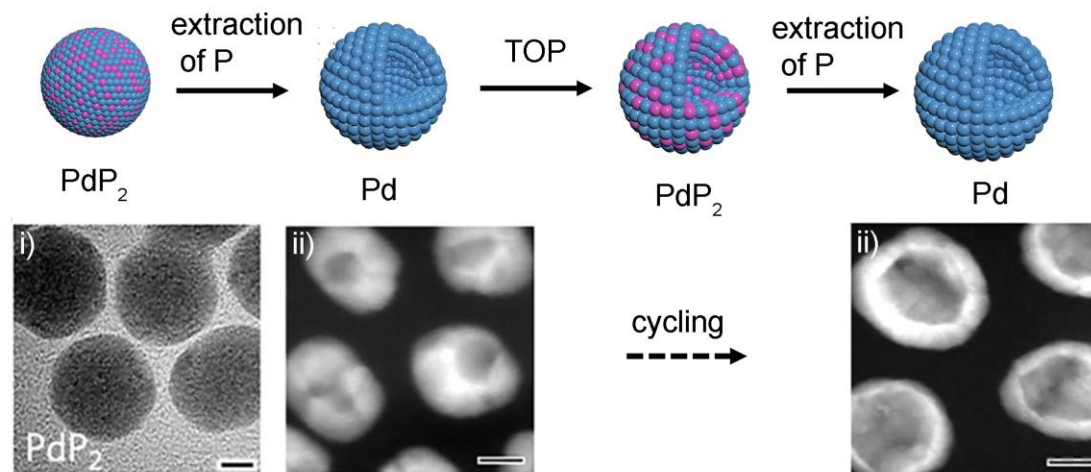


**Figure 1-3. a) Schematic illustration of the interfacial diffusion. b) Schematic illustration of alloy process of Au@Ag core-shell nanoparticles. Reproduced with permission from reference [34]. Copyright 2021 American Chemical Society. TEM images of i) Au, ii) Au@Ag, iii) Au@Ag@SiO<sub>2</sub>, and iv) AuAg alloy nanoparticles.**

**Reproduced with permission from [37]. Copyright 2014 American Chemical Society. c) Schematic illustration of the formation of the Pd hollow nanocrystals. TEM image of i) PdP<sub>2</sub>. SEM images of ii) Pd hollow structure after one cycle and iv) Pd hollow structure after two cycles. Reproduced with permission from reference [40]. Copyright 2017 Springer Nature Publishing Group.**

possess. Taking Au and Ag as an example, the homogenous AuAg nanoalloy integrates the advantages of the strong surface plasmon resonance of Ag and the good chemical stability of Au. Due to the different reduction kinetics of the two metal precursors, conventional co-reduction approaches are difficult to achieve compositional and structural homogeneity. To this end, Gao et al. developed a surface-protected annealing process to enable the full interdiffusion of Au and Ag.<sup>37</sup> As shown in **Figure 1-3b**, Au nanoparticles were coated with an Ag shell and then protected by the SiO<sub>2</sub> layers. After annealing at 1000 °C and etching away the SiO<sub>2</sub> protection layer, the as-prepared AuAg nanoalloy shows an extremely narrow and sharp plasmonic peak, demonstrating its homogeneity in the composition and structure.

Beyond that, chemical reactions may provide a much stronger driving force for the transformation of nanostructures compared to the thermal-driven transformation at relatively low temperatures.<sup>34</sup> This kind of chemically driven interdiffusion of atoms can create unique hollow nanostructures. A good example is the case of the galvanic replacement reaction between Ag and Au. Given the difference in the reduction potential of AuCl<sub>4</sub><sup>-</sup>/Au (0.99 V vs. standard hydrogen electrode (SHE)) and Ag<sup>+</sup>/Ag (0.80 V vs. SHE), Au prefers to deposit on the Ag core to form a shell while surface Ag will be oxidized and dissolved into the solution. Driving by the higher diffusion rate of Ag and the tendency to react with AuCl<sub>4</sub><sup>-</sup>,<sup>38</sup> outward diffusion of Ag atoms in the core takes place and results in the formation of Au hollow nanocrystals.<sup>39</sup> Another example is the formation of the Pd hollow spheres by cyclically inserting P into the Pd lattice and then extracting P out.<sup>40</sup> The affinity of P toward O<sub>2</sub> imposes the driving force on its outward diffusion, which contributes to the coalescence of voids in the core and the formation of the Pd shell. These unique hollow structures expose more active sites than solid nanoparticles, thereby exhibiting much higher catalytic activities.

## 1.3 Applications

### 1.3.1 Direct methanol fuel cells

The environment and energy issues in the present life are urging people to seek alternative clean and sustainable energy resources. Fuel cells, as a promising alternative power generation device, that converts chemical energy to electrical energy through chemical reactions, have gained widespread attention around the world over the passing decades.<sup>41-43</sup> Beyond the eco-friendly and sustainable nature, the advantages of fuel cells lie in their adaptability in terms of operating temperature, fuel types, electrolytes, membranes, and electrodes.<sup>44</sup> Among all the fuels, hydrogen has the highest energy (32.67 kW h kg<sup>-1</sup>), and methanol with an energy density of 6.13 kW h kg<sup>-1</sup> is the next best fuel following hydrogen (**Table 1-1**). Notably, even though methanol is not comparable to hydrogen in terms of energy density, it is cheap, plentiful, and renewable from wood alcohol. What is more, since it is a liquid, it is convenient to store, transport, and distribute using the existing infrastructures. These advantages of methanol as fuel have dramatically driven the development of direct methanol fuel cells (DMFCs).

**Table 1-1. Chemical and electrochemical data of various fuels. Adapted with permission from reference [44]. Copyright 2006 Universities Press (India) Private Ltd.**

fuel	$\Delta G^\circ$ (kcal/mol)	$E^\circ_{\text{theor}}$ (V)	$E^\circ_{\text{max}}$ (V)	energy density [(kW h)/kg]
hydrogen	-56.69	1.23	1.15	32.67
methanol	-166.80	1.21	0.98	6.13
ammonium	-80.80	1.17	0.62	5.52
hydrazine	-143.9	1.56	0.28	5.22
formaldehyde	-124.7	1.35	1.15	4.82
carbon monoxide	-61.60	1.33	1.22	2.04
formic acid	-68.20	1.48	1.14	1.2
methane	-195.50	1.06	0.58	
propane	-503.20	1.08	0.65	

DMFCs are a subcategory of proton-exchange fuel cells in which methanol is used as fuel. Their main advantage is the ease of transport of methanol, an energy-dense yet reasonably stable liquid under all environmental conditions. It consists of electrodes, the

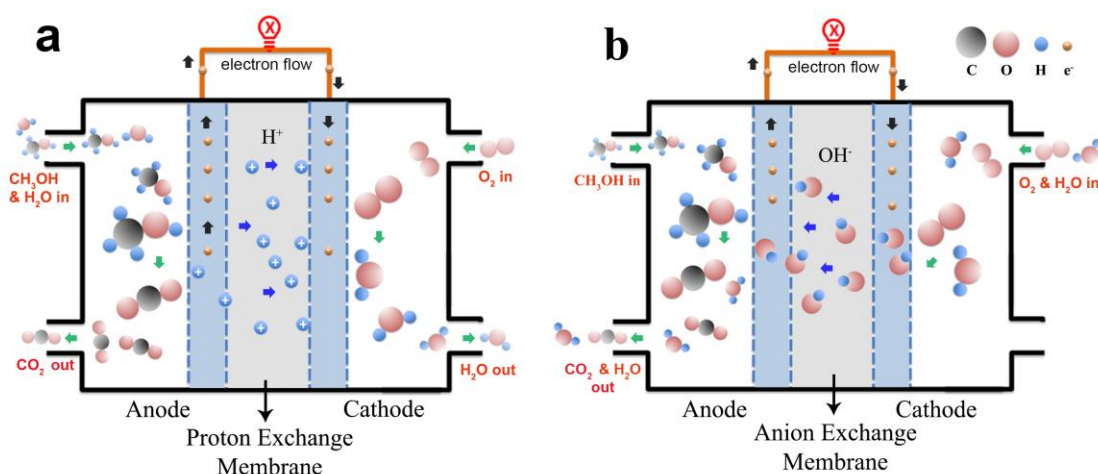
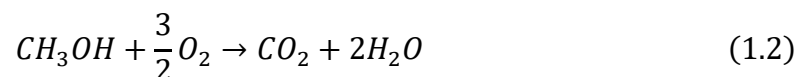


**Figure 1-4. a) The schematic illustration of DMFC operated with acidic electrolytes.**

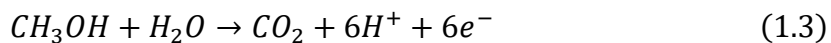
**b) The schematic illustration of DMFC operated with alkaline electrolytes.**

anode and cathode separated by an ion-exchange membrane, and electrolytes (**Figure 1-4**). DMFCs can be operated under either acidic or basic conditions, in which methanol and oxygen are directly fed at the anode and cathode, respectively. The overall reaction is the redox reaction between methanol and oxygen with  $\text{CO}_2$  and water as final products,

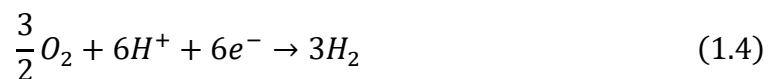


In the acidic electrolyte,  $\text{H}^+$  penetrates the proton-exchange membrane and achieves charge conduction between electrodes (**Figure 1-4a**). The half-reactions can be written as the followings.

The anodic reaction:

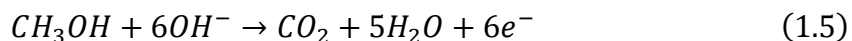


The cathodic reaction:

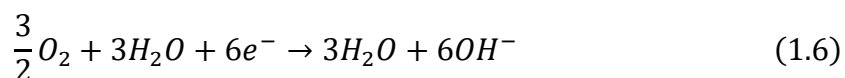


In the alkaline electrolyte,  $\text{OH}^-$  is responsible for the charge conduction, and an anion-exchange membrane is used to separate electrodes (**Figure 1-4b**). The half-reactions can be revised as the followings,

The anodic reaction:



The cathodic reaction:



No matter in the acidic or basic electrolytes, DMFCs are still facing technique issues that retards their large-scale industrial applications. For example, the electrocatalysts loading on the electrode are susceptible to corrosion by the electrolyte, especially under acidic conditions. It is a big challenge for ion-exchange membranes in the alkaline electrolyte because they are prone to degrading in this situation. Another server issue is the methanol crossover from the anode to the cathode, which results in the deactivation of cathodic catalysts.<sup>44</sup>

The heart of DMFCs is the electrocatalysts that catalyze the transformation from the chemical energy of small molecules to available electrical energy. Pt has been proven as the most efficient catalyst for the electrooxidation of methanol, but its commercial success is largely hinging on two factors, the cost, and the catalytic performance. Over the past decades, even though the cost issue can be well addressed through nanostructuring Pt to increase the atomic utilization efficiency and reduce the requiring demand of Pt, the efforts invested in the latter have been far less successful. It is generally accepted that methanol can be oxidized to  $\text{CO}_2$  through a dual-path mechanism, i.e., the direct pathway (formate as the intermediate) and the indirect pathway ( $\text{CO}$  as the intermediate).<sup>45</sup> However, almost all Pt-based electrocatalysts involve these two reaction paths and suffers from the poisoning of  $\text{CO}$ , leading to a quick loss of their activity. How to mitigate the  $\text{CO}$  poisoning effect is still a hot research topic and draws considerable attention in the electrochemistry field. The conventional strategy is modifying Pt with



oxyphilic metals or metal oxides/hydroxides, which can provide abundant OH species to facilitate the oxidative removal of adsorbed CO by a bifunctional effect.<sup>13</sup> PtRu alloy is a good example of the bifunctional effect.<sup>46</sup> Ru assists in the dissociative adsorption of water molecules to form OH species, which promotes the oxidation of CO at the neighboring Pt sites, thereby releasing the active sites for further methanol oxidation. Although there has been encouraging progress in the modification of Pt electrocatalysts for methanol electrooxidation, it is still far away from practical application. Electrocatalysts with low cost, good chemical stability, and CO-tolerance capability are still required to achieve the commercial success of DMFCs.

### 1.3.2 Selective hydrogenation of alkynes

Light olefins (ethylene and propylene) are key building blocks to produce plastics (i.e., polyethylene and polypropylene) and important raw materials for other chemicals (such as ethylbenzene, ethylene oxide, and ethylene dichloride).<sup>47</sup> Light olefins are mainly produced by steam cracking of a broad range of hydrocarbons (such as naphtha, gas oil, and condensates). The products produced in this process are highly dependent on the composition of the feed, the hydrocarbon to steam ratio, the cracking temperature, and the furnace residence time.<sup>48</sup> Therefore, such-made olefins inevitably contain impurities of alkynes and dienes.<sup>49</sup> For example, the ethylene stream usually contains 0.5-3 % of acetylene, while propyne and propadiene account for 2-8 % of the propene stream. These highly unsaturated compounds are poisonous to the Ziegler-Natta catalysts for the downstream polymerization and thus must be removed to a level lower than 5 ppm. To this end, selective hydrogenation of unsaturated hydrocarbons has proven its efficiency in the petrochemical and fine chemical industry.

The selective hydrogenation of alkynes follows the Horiuti-Polanyi mechanism, in which the dissociative adsorption of H<sub>2</sub> takes place on the surface, and then the formed hydrides add to the unsaturated bond of adsorbed alkyne sequentially.<sup>50</sup> Apart from the desired hydrogenation of alkynes to alkenes, three side reactions, including the over-hydrogenation to alkanes, oligomerization to higher hydrocarbons, and cracking to coke, occur simultaneously (**Figure 1-5**).<sup>51</sup> These byproducts produced by side reactions not only challenge the reaction installments but also deteriorates the activity and selectivity

of catalysts. Therefore, there is an urgent demand in the industry for developing catalysts that can efficiently suppress these side reactions in the selective hydrogenation of alkynes.

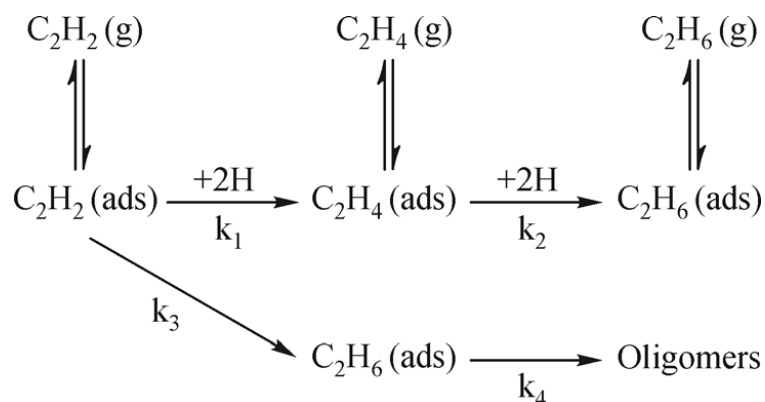


**Figure 1-5. Reaction network for acetylene hydrogenation. Adapted with permission from reference [50]. Copyright 2015 Spring Nature.**

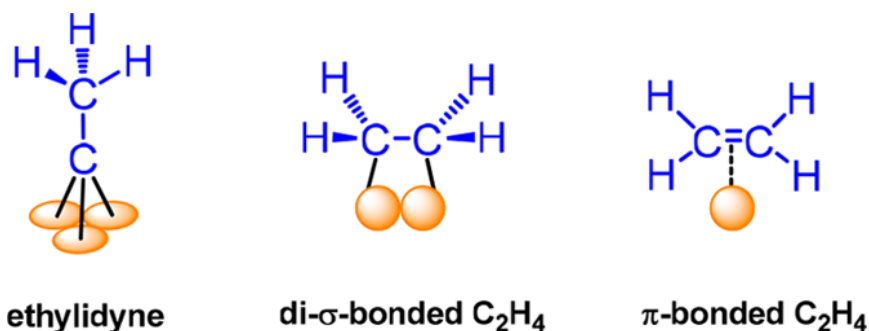


**Figure 1-6. Adsorption patterns of ethylene on Pd catalysts with different geometric structures. Adapted with permission from reference [49]. Copyright 2019 American Chemical Society.**

Pd is the most used catalyst to selectively hydrogenate alkynes to alkenes due to its efficiency in activating hydrogen molecules.<sup>52</sup> However, the selectivity toward alkenes upon unmodified Pd is quite low because of severe side reactions and oligomerization. Over the past few decades, extensive work has been focused on the modification of Pd catalysts for selective hydrogenation of alkynes. The traditional way is partially passivating the Pd surface with additives (such as CO or Pb/CaCO<sub>3</sub>), however, the gain in the selectivity is on the sacrifice of the activity.<sup>53</sup> Considering the close relationship

between the selectivity and the adsorption behavior of the unsaturated reactants/intermediates, alloying with a second metal is another efficient way to enhance the selectivity of Pd catalysts.<sup>54</sup> On the one hand, the charge redistribution induced by the different electronegativity can tune the adsorption strength of adsorbates thermodynamically. For example, the industrially employed Ag-Pd/Al<sub>2</sub>O<sub>3</sub> catalyst, in which electrons transfer from less electronegative Ag to Pd atoms, efficiently mitigates the over-hydrogenation of alkynes. On the other hand, the insertion of the second metal can change the adsorption types of intermediates, thereby influencing selectivity. Take the adsorption of ethylene on Pd catalysts as an example, ethylene has three adsorption modes: ethylidyne mode on 3-fold Pd sites, di- $\sigma$ -mode on bridged Pd dimers, and  $\pi$ -bonded mode on isolated Pd single atoms (**Figure 1-6**), and adsorption strength decreases in the order of ethylidyne > di- $\sigma$  >  $\pi$ -bonded. The weak adsorption means ethylene is more easily desorbing from the surface than undergoing further hydrogenation, which has driven the emergence of the “site isolation” strategy, i.e., breaking down the continuous Pd sites.<sup>49</sup> Under the guidance of this concept, a series of Pd-based intermetallic catalysts (such as PdZn,<sup>55,56</sup> PdSn,<sup>57</sup> PdGa,<sup>58</sup> PdIn,<sup>59</sup> etc.) and single-atom catalysts (single Pd atom anchored on carbon materials or metal oxides)<sup>60,61</sup> have been successfully synthesized and show enhanced selectivity toward targeted products. Although considerable progress has been achieved in improving the catalytic performance, it is still difficult to quantify the relationship between the performance and the geometric or electronic properties considering many entangled factors.

## 1.4 Thesis objectives

Targeting the issues that noble metal catalysts face in specific reactions, such as the methanol electrooxidation and the selective hydrogenation of propyne, the author has carried out a series of works about the design and surface modification of noble metal catalysts. Combining theoretical simulations and advanced characterization techniques, the author has been trying to capture the intrinsic nature of the local environment of the catalyst surface and quantify a reliable relationship between their catalytic performance and geometric as well as electronic structures.

## 1.5 Thesis outline

The outline of the thesis is as follows. Chapter 1 provides the introduction of noble metal-based nanocatalysts, the strategies to modify their surface properties, and their applications in DMFCs and selective hydrogenation reactions. Chapter 2 introduces the synchrotrons, beamlines, and spectroscopic techniques used in this thesis. Chapter 3 introduces the surface modification of Pt catalysts with an electrochemical reconstruction strategy, with a focus on the impact of bismuth oxyhydroxides on the CO-tolerance capability of Pt in methanol electrooxidation. Chapter 4 further discusses the real role of Bi in the suppression of the notorious CO-poisoning phenomenon of Pt in methanol electrooxidation. Chapter 5 investigates the spectroscopic characteristics of PdBi surface alloy and their application in selective hydrogenation of propyne. Chapter 6 summarizes the thesis and provides an outlook for the design and modification of noble metal-based catalysts.

## 1.6 References

- (1) Zhang, Y.; Gao, F.; You, H.; Li, Z.; Zou, B.; Du, Y. Recent advances in one-dimensional noble-metal-based catalysts with multiple structures for efficient fuel-cell electrocatalysis. *Coordination Chemistry Reviews* **2022**, *450*, 214244.
- (2) Rodrigues, T. S.; da Silva, A. G.; Camargo, P. H. Nanocatalysis by noble metal nanoparticles: Controlled synthesis for the optimization and understanding of activities. *Journal of Materials Chemistry A* **2019**, *7* (11), 5857.
- (3) Zang, W.; Li, G.; Wang, L.; Zhang, X. Catalytic hydrogenation by noble-metal nanocrystals with well-defined facets: A review. *Catalysis Science & Technology* **2015**, *5* (5), 2532.
- (4) Zhou, M.; Li, C.; Fang, J. Noble-metal based random alloy and intermetallic nanocrystals: Syntheses and applications. *Chemical Reviews* **2020**, *121* (2), 736.
- (5) Zhou, M.; Li, C.; Fang, J. Noble-metal based random alloy and intermetallic nanocrystals: Syntheses and applications. *Chemical Reviews* **2021**, *121* (2), 736.
- (6) Somwanshi, S. B.; Somvanshi, S. B.; Kharat, P. B. *Journal of Physics: Conference Series*, 2020; p 012046.
- (7) Pareek, V.; Bhargava, A.; Gupta, R.; Jain, N.; Panwar, J. Synthesis and applications of noble metal nanoparticles: A review. *Advanced Science, Engineering and Medicine* **2017**, *9* (7), 527.

- (8) Shi, Y.; Lyu, Z.; Zhao, M.; Chen, R.; Nguyen, Q. N.; Xia, Y. Noble-metal nanocrystals with controlled shapes for catalytic and electrocatalytic applications. *Chemical Reviews* **2021**, *121* (2), 649.
- (9) Loza, K.; Heggen, M.; Epple, M. Synthesis, structure, properties, and applications of bimetallic nanoparticles of noble metals. *Advanced Functional Materials* **2020**, *30* (21), 1909260.
- (10) Mustieles Marin, I.; Asensio, J. M.; Chaudret, B. Bimetallic nanoparticles associating noble metals and first-row transition metals in catalysis. *ACS Nano* **2021**, *15* (3), 3550.
- (11) Zhang, W.; Xiao, Y. Mechanism of electrocatalytically active precious metal (Ni, Pd, Pt, and Ru) complexes in the graphene basal plane for orr applications in novel fuel cells. *Energy & Fuels* **2020**, *34* (2), 2425.
- (12) Roth, C.; Papworth, A. J.; Hussain, I.; Nichols, R. J.; Schiffrin, D. J. A Pt/Ru nanoparticulate system to study the bifunctional mechanism of electrocatalysis. *Journal of Electroanalytical Chemistry* **2005**, *581* (1), 79.
- (13) Huang, W.; Wang, H.; Zhou, J.; Wang, J.; Duchesne, P. N.; Muir, D.; Zhang, P.; Han, N.; Zhao, F.; Zeng, M.; Zhong, J.; Jin, C.; Li, Y.; Lee, S. T.; Dai, H. Highly active and durable methanol oxidation electrocatalyst based on the synergy of platinum-nickel hydroxide-graphene. *Nature Communications* **2015**, *6*, 10035.
- (14) He, Q.; Xie, H.; Rehman, Z. U.; Wang, C.; Wan, P.; Jiang, H.; Chu, W.; Song, L. Highly defective Fe-based oxyhydroxides from electrochemical reconstruction for efficient oxygen evolution catalysis. *ACS Energy Letters* **2018**, *3* (4), 861.
- (15) Zhang, D.; Lu, J.; Pei, C.; Ni, S. Electrochemical activation, sintering, and reconstruction in energy-storage technologies: Origin, development, and prospects. *Advanced Energy Materials* **2022**, *12* (19), 2103689.
- (16) Sivanantham, A.; Ganesan, P.; Vinu, A.; Shanmugam, S. Surface activation and reconstruction of non-oxide-based catalysts through in situ electrochemical tuning for oxygen evolution reactions in alkaline media. *ACS Catalysis* **2019**, *10* (1), 463.
- (17) Gao, M.-R.; Zheng, Y.-R.; Jiang, J.; Yu, S.-H. Pyrite-type nanomaterials for advanced electrocatalysis. *Accounts of Chemical Research* **2017**, *50* (9), 2194.
- (18) You, B.; Sun, Y. Innovative strategies for electrocatalytic water splitting. *Accounts of Chemical Research* **2018**, *51* (7), 1571.
- (19) Kuznetsov, D. A.; Han, B.; Yu, Y.; Rao, R. R.; Hwang, J.; Román-Leshkov, Y.; Shao-Horn, Y. Tuning redox transitions via inductive effect in metal oxides and complexes, and implications in oxygen electrocatalysis. *Joule* **2018**, *2* (2), 225.

- (20) Hu, C.; Ma, Q.; Hung, S.-F.; Chen, Z.-N.; Ou, D.; Ren, B.; Chen, H. M.; Fu, G.; Zheng, N. In situ electrochemical production of ultrathin nickel nanosheets for hydrogen evolution electrocatalysis. *Chem* **2017**, *3* (1), 122.
- (21) Jiang, H.; He, Q.; Zhang, Y.; Song, L. Structural self-reconstruction of catalysts in electrocatalysis. *Accounts of Chemical Research* **2018**, *51* (11), 2968.
- (22) Liao, H.; Wei, C.; Wang, J.; Fisher, A.; Sritharan, T.; Feng, Z.; Xu, Z. J. A multisite strategy for enhancing the hydrogen evolution reaction on a nano-Pd surface in alkaline media. *Advanced Energy Materials* **2017**, *7* (21), 1701129.
- (23) In *Smithells metals reference book (eighth edition)*; Gale, W. F.; Totemeier, T. C., Eds.; Butterworth-Heinemann: Oxford, 2004.
- (24) Strasser, P.; Koh, S.; Anniyev, T.; Greeley, J.; More, K.; Yu, C.; Liu, Z.; Kaya, S.; Nordlund, D.; Ogasawara, H.; Toney, M. F.; Nilsson, A. Lattice-strain control of the activity in dealloyed core-shell fuel cell catalysts. *Nature Chemistry* **2010**, *2* (6), 454.
- (25) Matthews, J.; Academic Press, London, 1975.
- (26) Tan, C.; Chen, J.; Wu, X.-J.; Zhang, H. Epitaxial growth of hybrid nanostructures. *Nature Reviews Materials* **2018**, *3* (2).
- (27) Prieto, J. E.; Markov, I. Thermodynamic driving force of formation of coherent three-dimensional islands in stranski-krastanov growth. *Physical Review B* **2002**, *66* (7).
- (28) Kwon, S. G.; Krylova, G.; Phillips, P. J.; Klie, R. F.; Chattopadhyay, S.; Shibata, T.; Bunel, E. E.; Liu, Y.; Prakapenka, V. B.; Lee, B.; Shevchenko, E. V. Heterogeneous nucleation and shape transformation of multicomponent metallic nanostructures. *Nature Materials* **2015**, *14* (2), 215.
- (29) Li, X.; Liu, Y.; Bi, W.; Bi, J.; Guo, R.; Li, R.; Wang, C.; Zhan, Q.; Wang, W.; Yang, S.; Shi, F.; Wu, J.; Jin, M. Lattice-mismatch-induced growth of ultrathin Pt shells with high-index facets for boosting oxygen reduction catalysis. *Journal of Materials Chemistry A* **2020**, *8* (32), 16477.
- (30) Habas, S. E.; Lee, H.; Radmilovic, V.; Somorjai, G. A.; Yang, P. Shaping binary metal nanocrystals through epitaxial seeded growth. *Nature Materials* **2007**, *6* (9), 692.
- (31) Sneed, B. T.; Kuo, C. H.; Brodsky, C. N.; Tsung, C. K. Iodide-mediated control of rhodium epitaxial growth on well-defined noble metal nanocrystals: Synthesis, characterization, and structure-dependent catalytic properties. *Journal of the American Chemical Society* **2012**, *134* (44), 18417.

- (32) Wang, G.; Liu, Y.; Gao, C.; Guo, L.; Chi, M.; Ijro, K.; Maeda, M.; Yin, Y. Island growth in the seed-mediated overgrowth of monometallic colloidal nanostructures. *Chem* **2017**, *3* (4), 678.
- (33) Zhong, Q.; Feng, J.; Jiang, B.; Fan, Y.; Zhang, Q.; Chen, J.; Yin, Y. Strain-modulated seeded growth of highly branched black Au superparticles for efficient photothermal conversion. *Journal of the American Chemical Society* **2021**, *143* (48), 20513.
- (34) Chen, J.; Jiang, F.; Yin, Y. Manipulation of interfacial diffusion for controlling nanoscale transformation. *Accounts of Chemical Research* **2021**, *54* (5), 1168.
- (35) Steimle, B. C.; Fenton, J. L.; Schaak, R. E. Rational construction of a scalable heterostructured nanorod megalibrary. *Science* **2020**, *367* (6476), 418.
- (36) Nakajima, H. The discovery and acceptance of the Kirkendall effect: The result of a short research career. *Journal of the Minerals Metals and Materials Society* **1997**, *49* (6), 15.
- (37) Gao, C.; Hu, Y.; Wang, M.; Chi, M.; Yin, Y. Fully alloyed Ag/Au nanospheres: Combining the plasmonic property of Ag with the stability of Au. *Journal of the American Chemical Society* **2014**, *136* (20), 7474.
- (38) Kubaschewski, O. The diffusion rates of some metals in copper, silver, and gold. *Transactions of the Faraday Society* **1950**, *46*, 713.
- (39) Xia, X.; Wang, Y.; Ruditskiy, A.; Xia, Y. 25th anniversary article: Galvanic replacement: A simple and versatile route to hollow nanostructures with tunable and well-controlled properties. *Advanced Materials* **2013**, *25* (44), 6313.
- (40) Tianou, H.; Wang, W.; Yang, X.; Cao, Z.; Kuang, Q.; Wang, Z.; Shan, Z.; Jin, M.; Yin, Y. Inflating hollow nanocrystals through a repeated Kirkendall cavitation process. *Nature Communications* **2017**, *8* (1), 1261.
- (41) Kordesch, K. V.; Simader, G. R. Environmental impact of fuel cell technology. *Chemical Reviews* **1995**, *95* (1), 191.
- (42) Wang, C.-Y. Fundamental models for fuel cell engineering. *Chemical Reviews* **2004**, *104* (10), 4727.
- (43) Alias, M.; Kamarudin, S.; Zainoodin, A.; Masdar, M. Active direct methanol fuel cell: An overview. *International Journal of Hydrogen Energy* **2020**, *45* (38), 19620.
- (44) Kakati, N.; Maiti, J.; Lee, S. H.; Jee, S. H.; Viswanathan, B.; Yoon, Y. S. Anode catalysts for direct methanol fuel cells in acidic media: Do we have any alternative for Pt or Pt-Ru? *Chemical Reviews* **2014**, *114* (24), 12397.

- (45) Chen, Y. X.; Miki, A.; Ye, S.; Sakai, H.; Osawa, M. Formate, an active intermediate for direct oxidation of methanol on Pt electrode. *Journal of the American Chemical Society* **2003**, *125* (13), 3680.
- (46) Li, L.; Xing, Y. Pt-Ru nanoparticles supported on carbon nanotubes as methanol fuel cell catalysts. *The Journal of Physical Chemistry C* **2007**, *111* (6), 2803.
- (47) Trotus, I. T.; Zimmermann, T.; Schuth, F. Catalytic reactions of acetylene: A feedstock for the chemical industry revisited. *Chemical Reviews* **2014**, *114* (3), 1761.
- (48) Posch, W. In *Applied plastics engineering handbook*; Kutz, M., Ed.; William Andrew Publishing: Oxford, 2011, DOI:<https://doi.org/10.1016/B978-1-4377-3514-7.10003-0>.
- (49) Zhang, L.; Zhou, M.; Wang, A.; Zhang, T. Selective hydrogenation over supported metal catalysts: From nanoparticles to single atoms. *Chemical Reviews* **2020**, *120* (2), 683.
- (50) Horiuti, I.; Polanyi, M. Exchange reactions of hydrogen on metallic catalysts. *Transactions of the Faraday Society* **1934**, *30*, 1164.
- (51) McCue, A. J.; Anderson, J. A. Recent advances in selective acetylene hydrogenation using palladium containing catalysts. *Frontiers of Chemical Science and Engineering* **2015**, *9* (2), 142.
- (52) Teschner, D.; Vass, E.; Hävecker, M.; Zafeirotos, S.; Schnörch, P.; Sauer, H.; Knop-Gericke, A.; Schlögl, R.; Chamam, M.; Wootsch, A. Alkyne hydrogenation over Pd catalysts: A new paradigm. *Journal of Catalysis* **2006**, *242* (1), 26.
- (53) Takht Ravanchi, M.; Sahebdehfar, S.; Komeili, S. Acetylene selective hydrogenation: A technical review on catalytic aspects. *Reviews in Chemical Engineering* **2018**, *34* (2), 215.
- (54) Zhao, X.; Chang, Y.; Chen, W.-J.; Wu, Q.; Pan, X.; Chen, K.; Weng, B. Recent progress in Pd-based nanocatalysts for selective hydrogenation. *ACS Omega* **2021**, *7* (1), 17.
- (55) Glyzdova, D. V.; Vedyagin, A. A.; Tsapina, A. M.; Kaichev, V. V.; Trigub, A. L.; Trenikhin, M. V.; Shlyapin, D. A.; Tsyrlunikov, P. G.; Lavrenov, A. V. A study on structural features of bimetallic Pd-M/C (m: Zn, Ga, Ag) catalysts for liquid-phase selective hydrogenation of acetylene. *Applied Catalysis A: General* **2018**, *563*, 18.
- (56) Dasgupta, A.; He, H.; Gong, R.; Shang, S. L.; Zimmerer, E. K.; Meyer, R. J.; Liu, Z. K.; Janik, M. J.; Rioux, R. M. Atomic control of active-site ensembles in ordered alloys to enhance hydrogenation selectivity. *Nature Chemistry* **2022**, DOI:10.1038/s41557-021-00855-3.



- (57) Li, R.; Yue, Y.; Chen, Z.; Chen, X.; Wang, S.; Jiang, Z.; Wang, B.; Xu, Q.; Han, D.; Zhao, J. Selective hydrogenation of acetylene over Pd-Sn catalyst: Identification of Pd<sub>2</sub>Sn intermetallic alloy and crystal plane-dependent performance. *Applied Catalysis B: Environmental* **2020**, *279*, 119348.
- (58) Prinz, J.; Pignedoli, C. A.; Stöckl, Q. S.; Armbrüster, M.; Brune, H.; Gröning, O.; Widmer, R.; Passerone, D. Adsorption of small hydrocarbons on the three-fold PdGa surfaces: The road to selective hydrogenation. *Journal of the American Chemical Society* **2014**, *136* (33), 11792.
- (59) Cao, Y.; Sui, Z.; Zhu, Y.; Zhou, X.; Chen, D. Selective hydrogenation of acetylene over Pd-In/Al<sub>2</sub>O<sub>3</sub> catalyst: Promotional effect of indium and composition-dependent performance. *ACS Catalysis* **2017**, *7* (11), 7835.
- (60) Zhou, S.; Shang, L.; Zhao, Y.; Shi, R.; Waterhouse, G. I.; Huang, Y. C.; Zheng, L.; Zhang, T. Pd single - atom catalysts on nitrogen-doped graphene for the highly selective photothermal hydrogenation of acetylene to ethylene. *Advanced Materials* **2019**, *31* (18), 1900509.
- (61) Guo, Y.; Qi, H.; Su, Y.; Jiang, Q.; Cui, Y. T.; Li, L.; Qiao, B. High performance of single-atom catalyst Pd<sub>1</sub>/MgO for semi-hydrogenation of acetylene to ethylene in excess ethylene. *ChemNanoMat* **2021**, *7* (5), 526.

## Chapter 2

### 2 Synchrotron Instruments

#### 2.1 Synchrotron overview

Since the first X-ray was discovered by German physicist Wilhelm Röntgen in 1895, X-ray has thrived in many disciplines including physics, chemistry, materials science, biology, medical science, and so on. X-ray features in high energy (100 eV – 100 keV) and short wavelengths (0.01 – 10 nm). The wavelength is parallel to the atomic size, making measurements possible at the atomic scale. What is more, almost all elements have absorption edges (abrupt change of light absorption) and light emission in the X-ray energy range. These features can serve as elemental fingerprints in material characterizations. As a bright and collimated X-ray source, synchrotron has been developed to provide characterization techniques for scientific research. The synchrotron can accelerate electrons to nearly the speed of light and produces highly polarized light in a continuous energy range from infrared light (IR) to X-rays when the electrons are accelerated centrifugally by their trajectory being bent by bending magnets. Compared with lab X-rays, synchrotron X-rays feature wide tunability of the energy (from IR to X-rays), high brightness (the higher flux of photons of a given wavelength on the tiny spot with a small divergence), a high extent of polarization (Linear, circular, or elliptical polarization), time structure (light pulses with dark intervals at the scale of a hundred nanoseconds arising from the radio frequency cavities), and partial coherence (laser-like beam). With these features, synchrotron X-rays pave the way for the development of characterization techniques associated with X-ray absorption, X-ray emission, X-ray scattering, and so on.

**Figure 2-1** schematically shows a typical synchrotron. Electrons originally generated by a heated cathode, named electron gun, are accelerated in the linear accelerator (LINAC) with a high vacuum environment. These electrons get speed up to 99.9998 % of the speed of light with an energy of hundreds of MeV before leaving the LINAC. They are then injected into the booster ring and get further acceleration to 99.9999985 % of the speed of light with energy to the orders of GeV. These electrons finally get into the storage ring,

where they are kept cycling for hours even days. Bending magnets used to direct the electron beam are usually located at the turning sections, where the synchrotron radiations are generated by the highly relativistic electrons. When synchrotron comes to the third generation, insertions, such as wigglers and undulators, are introduced into the straight sections to provide more brighter and coherent X-rays. The generation of synchrotron leads to the energy loss of electrons, which are replenished by the radiofrequency (RF) cavities inserted in the storage ring. Meanwhile, the oscillating electromagnetic field of RF cavities synchronizes the electron bundles at the relativistic domain, which makes it possible to get a time structure. Each beamline has its own designed functionalities and supports a wide range of advanced characterization techniques at the endstations.

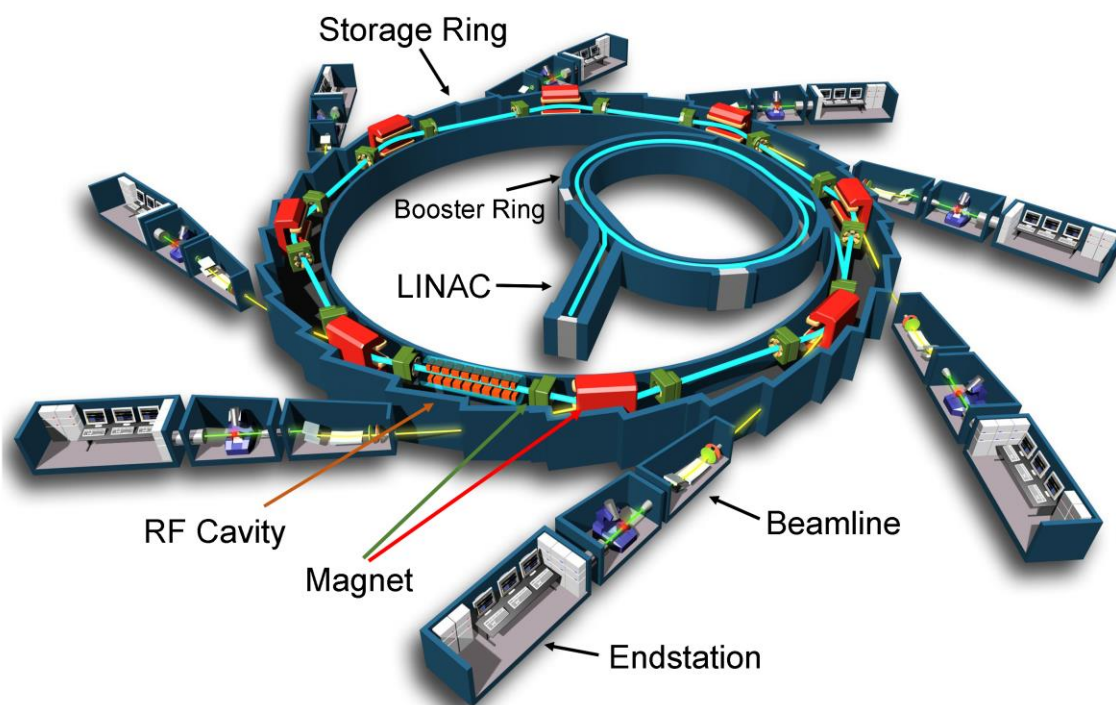


**Figure 2-1. Schematic of a synchrotron. The synchrotron ring is reprinted from EPSIM 3D/JF Santarelli, Synchrotron Soleil. Copyright @ EPSIM 3D/JF Santarelli, Synchrotron Soleil.**

## 2.2 Synchrotron Facilities

### 2.2.1 Canadian Light Source (CLS)

Canadian Light Source (CLS) located in Saskatoon, Saskatchewan, Canada, is a third-generation synchrotron, equipped with a 2.9 GeV storage ring with a circumference of 170.88 m and a maximum current of 220 mA. The horizontal and vertical emittances are 18 and 0.09 nm·rad, respectively. Since the formal opening of the CLS in 2005, the number of operational beamlines has been increased to 15 through Phase-I to Phase-IV construction and upgrade, covering a wide range of applications.<sup>1</sup>

### 2.2.2 Advanced Photon Source (APS)

Advanced Photon Source (APS) located at Argonne National Laboratory, Chicago, Illinois, USA, is a third-generation synchrotron, equipped with a 7.0-GeV storage ring and a 450-MeV linear accelerator as the injector. The ring has a circumference of 1,104 m, with an operating ring current of 100 mA and an effective emittance of 3.1 nm·rad. Currently, the APS consists of 34 sectors with a total of more than 50 beamlines covering nearly every scientific discipline, from materials science to biology, chemistry, environmental, geological, and planetary science, and fundamental physics.

### 2.2.3 Taiwan Light Source (TLS) and Taiwan Photon Source (TPS)

Taiwan Light Source (TLS) and Taiwan Photon Source (TPS) locate in the Hsinchu Science Park, Taiwan, China, operated by the National Synchrotron Radiation Research Center (NSRRC). TLS was a third-generation synchrotron, equipped with a 1.5-GeV storage ring with a maximum current of 360 mA. The circumference of TLS is 120 m, and the horizontal and vertical emittances are 22 and 88 nm·rad, respectively. Over 50 experimental stations on 24 beamlines are operating in the TLS. TPS with a circumference of 518.4 m, is equipped with a low-emittance synchrotron storage ring and a booster ring in the same tunnel producing a beam of 3 GeV. The horizontal and vertical emittances are 1.6 and 16 nm·rad, respectively. It has a capacity of about 40 beamlines; five of the initial beamlines are now open to users, and nine phase-II beamlines are in commissioning or under construction.

## 2.3 Beamlines

The beamlines related to this thesis are briefly described in the following.

### 2.3.1 Beamline Sector 20-BM at APS

The sector 20-BM beamline at APS uses the beam source generated from the bending magnet. The Si (111) monochromator with an energy resolution of  $1.4 \times 10^{-4}$ , from 2.7 to 32.7 KeV,<sup>2</sup> is used. The available X-ray techniques include X-ray absorption fine structure (XAFS), micro-fluorescence, micro-XAFS, micro-diffraction, time-resolved X-ray excited optical luminescence (TRXEOL), and diffraction anomalous fine structure, covering the disciplines of material science, environmental science, and chemistry. In this thesis, some of the hard X-ray XAFS were collected at the 20-BM beamline.

### 2.3.2 Soft X-ray microcharacterization beamline (SXRMB) at CLS

SXRMB at CLS is a medium energy x-ray beamline with a range of 1.7 to 10 keV. The InSb (111) monochromator has an energy resolution of  $3.3 \times 10^{-4}$  over the range from 1.7 to 3.7 keV. The Si (111) monochromator has an energy resolution of  $1.0 \times 10^{-4}$  over the range of 2 to 10 keV. The InSb (111) provides the higher flux while the Si (111) has the higher energy resolution.<sup>3</sup> Five endstations are available at the SXRMB:

(1) Solid state endstation. Bulk analysis of solid samples, such as pellets and powders can be performed using this endstation. Samples are placed under a vacuum of  $10^{-7}$  torr, and the endstation is optimized for the lower energy edges, such as Si, P, and S.

(2) Microprobe endstation. This endstation provides a  $10 \times 10 \mu\text{m}$  beam spot for use in mapping experiments.<sup>4</sup> Micro-XAS can also be performed on specific spots using the microprobe.

(3) Ambient table. This multiple-use endstation is designed for bulk analysis of many different samples. The endstation can be configured for liquid and solid in-situ experiments as well.

(4) High energy XPS.<sup>5</sup> By setting the beamline to varying energies, x-ray photoelectron spectroscopy (XPS) will be performed at different depths on the same sample, providing information on the surface and bulk properties of the material. In this thesis, Pd L<sub>3</sub>-edges were collected with a surface-sensitive TEY mode at the SXRMB beamline.

(5) Glovebox integrated high energy resolution X-ray emission spectrometer; custom built by easyXAFS company. This end-station allows for the detection of tender X-ray fluorescence from 1.7 – 8 keV.<sup>6</sup>

### 2.3.3 Beamline sector 24A1 at TLS

This beamline has two endstations, i.e., surface/interface science endstation and ambient pressure X-ray photoelectron spectroscopy (APXPS) endstation. The surface/interface science endstation is dedicated to ultra-high vacuum (UHV)-based surface chemistry experiments with measurement capability including temperature-programmed desorption (TPD), imaging-type XPS possessing a 1D resolution of 35  $\mu\text{m}$ , and near-edge X-ray absorption fine structure (NEXAFS) spectroscopy. All the surface analysis instruments are in the 14'' analysis sphere. The X-ray spot sizes at the sample position of the endstation were measured with a Ce-doped YAG fluorescent single crystal and varied between 1.3 to 2.8 mm (FWHM) vertically but remained rather constant at 1.5 mm (FWHM) horizontally. The APXPS endstation is designed primarily for performing XPS measurements of solid surfaces interacting with gasses at elevated pressure up to 10 mbar.<sup>7</sup> In contrast to the conventional X-ray photoelectron spectroscopy that is performed in a high-vacuum environment to eliminate electron-gaseous molecule scattering events, APXPS is carried out in a mbar pressure range, enabling the acquisition of photoelectron signals from a gas, solid surface, and liquid surface as well. The realization of this unconventional technique hinges on the successful development of a sophisticated electrostatic lens of the analyzer in conjunction with an elaborate differential pumping system. The technique enables an in-situ and in-operando investigation of heterogeneous reactions and allows researchers to extract the crucial information heretofore unavailable in many important research areas including catalysis, energy storage, and environmental and atmospheric sciences. In this thesis, an investigation of the CO adsorption behavior on Pt-based catalysts was performed at the APXPS beamline.

### 2.3.4 Beamline sector 44A at TPS

Quick-scanning X-ray absorption spectroscopy beamline using a bending magnet at Taiwan Photon Source (TPS) was newly constructed for the studies of physics, chemistry, biology, environment, and arts. This beamline covers the energy range from 4.5 to 34 keV with a focused spot size,  $70 \times 200 \mu\text{m}^2$  or  $10 \times 10 \mu\text{m}^2$ . Four techniques are available at 44A, including X-ray absorption spectroscopy, time-resolved X-ray absorption spectroscopy, X-ray absorption fine structures spectroscopy, and micro-X-ray fluorescence microscopy. In this thesis, some of the hard X-ray XAFS were collected at the 44A beamline.

## 2.4 Synchrotron X-ray techniques

### 2.4.1 X-ray absorption spectroscopy (XAS)

When light interacts with matter, the incident photons can be either absorbed, scattered, or transmitted. The relationship between the intensities of the transmitted ( $I_t$ ) and the incident X-ray ( $I_0$ ) follows the Beer-Lambert Law (Eq. 2.1), where  $t$  is the thickness of the sample and  $\mu$  is the absorption coefficient. The absorption coefficient can be expressed as Eq. 2.2, where  $\sigma$  is the X-ray absorption cross-section,  $\rho$  is the sample density,  $Z$  is the atomic number,  $A$  is the atomic mass, and  $E$  is the X-ray energy. The adsorption coefficient is dependent on the atomic number and X-ray energy, indicating its element-specific nature. Generally, the X-ray absorption increases abruptly at the edge (excitation from the core level to an unoccupied bound/quasi-bound state or the continuum) and decreases gradually afterward until meeting another absorption edge (from the same or another element), following the trend of the cross section  $\sigma$ . For the FY and TEY modes,  $\mu$  is proportional to the ratio between the yield and  $I_0$  (Eq. 2.3). This equation holds when affecting factors such as self-absorption are small.

$$\frac{I_t}{I_0} = e^{-\mu t} \quad (2.1)$$

$$\mu = \sigma \cdot \rho \approx \frac{\rho Z^4}{AE^3} \quad (2.2)$$

$$\mu \approx \frac{I_{e,f}}{I_0} \quad (2.3)$$

X-ray absorption spectroscopy (XAS) or X-ray absorption fine structure (XAFS) is a technique to look into the chemical state and local structure of materials, fundamentally based on the specific absorption of X-ray at the edge. The hard X-ray absorption spectrum contains two regions, the X-ray near edge structure (XANES, -20 to +50 eV relative to the absorption edge) and extended X-ray absorption fine structure (EXAFS, +50 eV relative to the absorption edge). However, for the soft X-ray absorption spectrum, normally only XANES is analyzed due to the closeness of edges (from the same element or different elements). Although XANES and EXAFS are collected simultaneously, the origin of each is fundamentally different. When an incident X-ray shines on the sample, core electrons are excited to the unoccupied state or quasi-state (the absorption edge mentioned above) while extra energy transforms them into photoelectrons. These photoelectrons propagate as De Broglie waves with wavelengths described by Eq. 2.4,

$$\lambda = \frac{h}{p} = \frac{h}{\sqrt{2m(E - E_0)}} \quad (2.4)$$

where  $h$  is the Planck constant,  $p$ ,  $m$ , and  $E - E_0$  are the momentum, mass, and kinetic energy of the electron, respectively. Photoelectrons with low kinetic energy tend to be scattered multiple times and contribute to the XANES features while photoelectrons with high kinetic energy contribute to the EXAFS by single scattering (**Figure 2-2**).



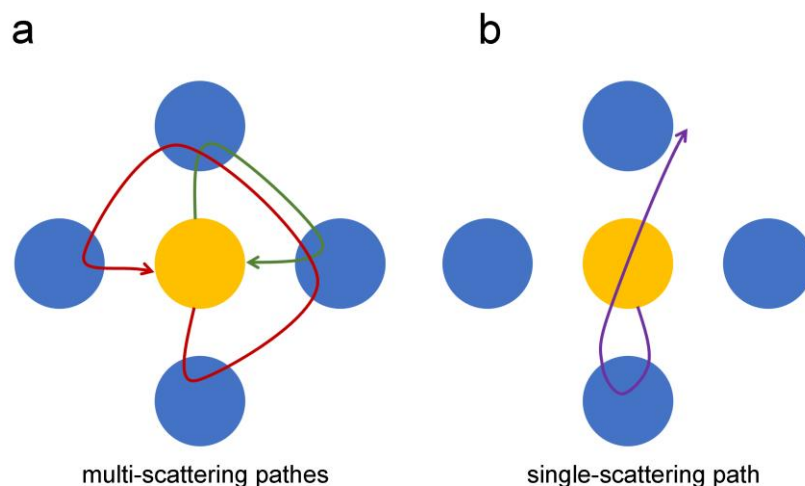


**Figure 2-2. The schematic illustrations to a) multi-scattering paths and b) single-scattering path.**

In the XANES region, transitions of core electrons to unoccupied bound/quasi-bound or the continuum follow the dipole selection rule ( $\Delta l = \pm 1$ ,  $\Delta j = \pm 1, 0$ ). As a result, the absorption edge position ( $E_0$ ) is sensitive to the oxidation state, e.g., the higher oxidation state is usually accompanied by the edge appearing at the higher energy. Pre-edge features are sensitive to the local symmetry due to the crystal field splitting and orbital hybridization, which generate unoccupied dipole-prohibited states at an energy lower than the absorption edge. Besides, the whiteline peak (the major peak following the absorption edge) area is sensitive to the number of dipole-allowed unoccupied states. The electron transition rate  $P_{i \rightarrow f}$  from the initial state  $|\psi_i\rangle$  (with energy  $E_i$ ) to the final state  $|\psi_f\rangle$  (with energy  $E_f$ ) is described by Fermi's golden rule in Eq. 2.5, where  $\hat{H}'$  is the interaction Hamiltonian operator between the electromagnetic field and the electron, and  $\rho$  is the density of states. Because of the high sensitivity of chemical environments, XANES is extensively used in the analysis of oxidation state, chemical components, occupation of molecular orbitals, local symmetry, and so on.

$$P_{i \rightarrow f} = \frac{2\pi}{\hbar} |\langle \psi_f | \hat{H}' | \psi_i \rangle|^2 \rho \quad (2.5)$$

$$k = \frac{2\pi}{\lambda} = \frac{\sqrt{2m(E - E_0)}}{\hbar} \quad (2.6)$$

EXAFS measures the modulation of the absorption coefficient as a function of photon energy beyond the XANES region. It is commonly expressed in  $k$  space by transforming the electron kinetic energy to wavenumber, as described by Eq. 2.6. The EXAFS features originate from the interference between the outgoing electron wave and the backscattered electron wave by surrounding atoms. Eq. 2.7 describes the well-developed model for the EXAFS,<sup>8,9</sup>

$$\chi(k) = \sum_j \left[ \frac{N_j S_0^2 f(k, \theta) e^{-2R_j/\lambda_e(k)} e^{-2k^2 \sigma_j^2}}{k R_j^2} \right] \sin[2kR_j + \delta(k)] = A(k)\Phi(k) \quad (2.7)$$

where  $N_j$  is the coordination number (CN) of atom type  $j$ ;  $S_0^2$  is the amplitude reduction term induced by the many-body effects;  $f(k, \theta)$  is the atomic scattering amplitude;  $e^{2R_j/\lambda_e(k)}$  is the amplitude damping term due to the electron escape depth  $\lambda_e$ ;  $e^{-2k^2 \sigma_j^2}$  is the Debye-Waller factor, that is, the amplitude damping term due to thermal motion;  $R_j$  is the interatomic distance between the absorber atom and the scatterer atom;  $\delta(k) = 2\delta_a(k) + \delta_b(k)$  is the phase shift function attributed to the absorber  $\delta_a(k)$  and the back-scatterer  $\delta_b(k)$ . EXAFS spectra can be fitted to obtain the coordination number (CN) and interatomic distances for the elements of interest, in which  $N_i$ ,  $S_0$ ,  $\sigma_j^2$ , and  $R_j$  are the parameters commonly fitted. EXAFS can be Fourier transformed into R Space, from which it is visually plausible to identify the crystal structure of crystalline materials. Specifically, in the R space, the peak intensity is proportional to the CN of the corresponding scatter, while the peak position is related to the interatomic distance ( $\sim 0.5$  Å smaller than the real bond distance because of the phase shift  $\delta(k)$ ).

#### 2.4.1.1 Detection modes

XAS beamlines are normally equipped with multiple detecting modes (detectors) to meet different experiment requirements. **Figure 2-3** shows the optical path of synchrotron X-rays at the endstation while multiple detecting modes can be applied simultaneously.

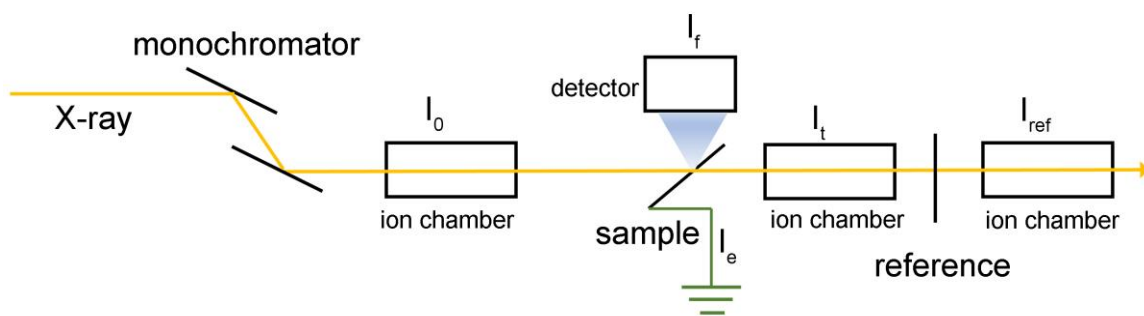


**Figure 2-3. Optical path of synchrotron X-rays at the endstation showing the three detecting modes.**

#### 2.4.1.1.1 Fluorescence yield (FY)

FY mode detects the X-ray fluorescence ( $I_f$ ) signal when the incident X-ray ( $I_0$ ) bombards the sample. The fluorescence detector is normally aligned 45 degrees to the sample and 90 degrees to the incident beam. FY mode is usually considered bulk sensitive due to the deep penetrating depth, but it also can exclusively probe the surface by adjusting the incident beam with a glancing angle. For a very dilute sample, FY mode is the best choice to obtain enough signal. However, thick samples (elementally dense) suffer from the self-absorption effect induced by the reabsorption of the sample. This effect is more severe for low  $Z$  elements using soft X-ray.

#### 2.4.1.1.2 Transmission

Transmission mode collects the light signal ( $I_t$ ) after the incident X-ray ( $I_0$ ) has been partially absorbed by the sample. The light intensity is measured by the ionization of the inert gas in the ion chamber. Since the X-ray passes through the whole sample, the transmission mode is bulk sensitive. This mode is a good option for samples with a proper thickness (one absorption length,  $\sim 36\%$  absorption of the incident light), which can bypass the self-absorption occurring in the FY mode and provide a reliable signal.

### 2.4.1.1.3 Total electron yield (TEY)

TEY mode measures the total electron yield including photoelectrons, auger electrons, and secondary electrons ejected from the sample by monitoring the current compensation ( $I_c$ ). Because electrons carry charge and mass, of which the traveling trajectories are severely affected by electromagnetic fields, the TEY mode is quite surface sensitive. The probing depth depends on the electron inelastic mean free path (IMFP),<sup>10</sup> in other words, the kinetic energy of electrons and elemental density of the sample. Therefore, this mode is the best option to probe the surface properties. The TEY mode was used in this thesis to study the properties of PdBi surface alloy on the Pd core in chapter 5.

### 2.4.2 Synchrotron X-ray photoelectron spectroscopy (XPS)

X-ray photoelectron spectroscopy (XPS) is a photon in, electron out technique, specifically, core and valence electrons are ejected if the photon energy is greater than the binding energy of the electrons. This technique is fundamentally based on the photoelectric effect theorized by Albert Einstein in 1905, as described in Eq. 2.8.

$$KE = h\nu - BE - \phi \quad (2.8)$$

where  $KE$  is the kinetic energy of photoelectrons,  $h\nu$  is the incident photon energy,  $BE$  is the binding energy of an electron ejected by irradiation, and  $\phi$  is the work function that is the minimum energy to remove an electron from the Fermi level to vacuum. XPS probes the energy state of bound electrons of matter, including electrons with discrete energy (atomic orbitals), shallowing bond electrons (molecular orbitals), and closely spaced energy states (energy bands in solids). This technique is element and chemical-specific since it monitors the change of the threshold of core levels, which are element specific and chemically sensitive. Generally, a single particle approximation is used to interpret XPS spectra, in which the energy of the photoelectron is a good approximation independent of the movement of the other electrons, yielding a single peak or spin-orbit doubles. But in some cases, the energy of the photoelectron dose depends on the presence of other electrons which get excited simultaneously yielding satellite peaks (shake-up, shake-off, and shake-down) or even the complete disappearance of the single-particle peak, which is called the many-body effect. Apart from the electronic structures, XPS

also can provide information on elemental compositions after calibration with their corresponding sensitive factors.

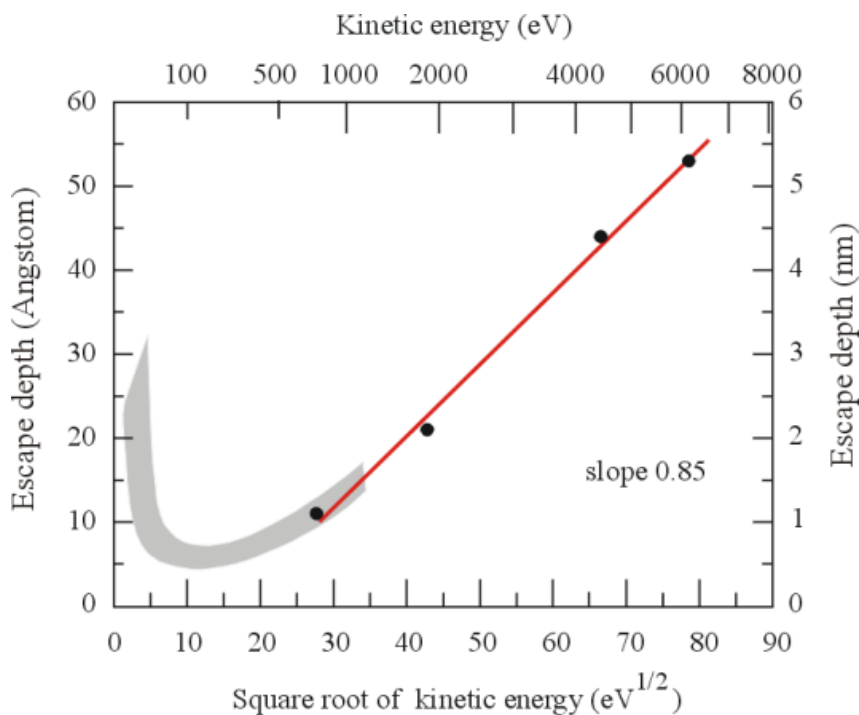


**Figure 2-4. Schematic illustration of the universal escape depth curve of electrons versus square root of kinetic energy. Measurements at ID32, ESRF (European Synchrotron Radiation Facility) by J. Zegenhagen.**

Generally, Al  $K_{\alpha}$  (~1486 eV) or Mg  $K_{\alpha}$  (~1253 eV) serves as the laboratory X-ray source for XPS. Experimentally, XPS measures the kinetic energy of the photoelectrons ejected from all levels (binding energy) accessible at given photon energy. The probing depth is determined by the escape depth of electrons, also called inelastic mean free path (IMFP), which shows a universal relationship with the square root of kinetic energy, as shown in **Figure 2-4**. Laboratory X-ray photoelectron spectroscopy is quite surface sensitive (~1 to 2 nm) considering the energy range of X-ray sources. Compared to laboratory X-rays with fixed energy, synchrotron endows X-rays with tunability in terms of energy, in other words, one can look into different depths of a sample by tuning the energy of incident synchrotron X-ray. The high flux of synchrotron X-rays also brings much better signals. Technically, it is available to adjust the incident angle of X-rays to perform depth

analysis. With advances in the development of equipment, gases even can be dosed into the chamber to perform XPS measurements of solid surfaces interacting with gasses at near ambient pressure. In this thesis, near ambient pressure X-ray photoelectron spectroscopy was performed to study the adsorption behavior of CO molecules on PtBi catalysts in Chapter 3.

## 2.5 References

- (1) Cutler, J.; Chapman, D.; Dallin, L.; Lamb, R. The brightest light in Canada: The Canadian Light Source. *Quantum Beam Science* **2017**, *1* (1), 4.
- (2) Heald, S.; Brewster, D.; Stern, E.; Kim, K.; Brown, F.; Jiang, D.; Crozier, E.; Gordon, R. XAFS and micro-XAFS at the PNC-CAT beamlines. *Journal of synchrotron radiation* **1999**, *6* (3), 347.
- (3) Hu, Y.; Coulthard, I.; Chevrier, D.; Wright, G.; Igarashi, R.; Sitnikov, A.; Yates, B.; Hallin, E.; Sham, T.; Reininger, R. AIP conference proceedings, 2010; p 343.
- (4) Xiao, Q.; Hu, Y.; Sham, T. Microprobe endstation at SXRMB of Canadian Light Source: Introduction and applications. *Microscopy and Microanalysis* **2018**, *24* (S2), 466.
- (5) Xiao, Q.; Cui, X.; Shi, Y.; Hu, Y.; Sham, T.-K.; Piao, H.; McMahon, J. The hard X-ray photoemission spectroscopy facility at CLS: Performance and first results. *Canadian Journal of Chemistry* **2015**, *93* (1), 113.
- (6) Shakouri, M.; Holden, W. M.; Hu, Y.; Xiao, Q.; Igarashi, R.; Schreiner, B.; Bree, M.; Li, M.; Li, W.; Sun, X. Glovebox-integrated XES and XAS station for in situ studies in tender x-ray region. *Electronic Structure* **2020**, *2* (4), 047001.
- (7) Wang, C.-H.; Liu, B.-H.; Yang, Y.-W. Ambient pressure X-ray photoelectron spectroscopy (APXPS): Present status and future development at NSRRC. *Synchrotron Radiation News* **2022**, DOI:10.1080/08940886.2022.2082182, 1.
- (8) Rehr, J. J.; Albers, R. C. Theoretical approaches to X-ray absorption fine structure. *Reviews of modern physics* **2000**, *72* (3), 621.
- (9) Stern, E.; Sayers, D.; Lytle, F. Extended X-ray-absorption fine-structure technique. III. Determination of physical parameters. *Physical Review B* **1975**, *11* (12), 4836.
- (10) Powell, C. J.; Jablonski, A.; Salvat, F. NIST databases with electron elastic - scattering cross sections, inelastic mean free paths, and effective attenuation lengths. *Surface and Interface Analysis: An International Journal devoted to the*

*development and application of techniques for the analysis of surfaces, interfaces and thin films* **2005**, 37 (11), 1068.

## Chapter 3

### 3 Bismuth Oxyhydroxide-Pt Inverse Interface for Enhanced Methanol Electrooxidation Performance

#### 3.1 Introduction

Direct methanol fuel cells (DMFCs) have emerged as one of the most promising power sources for portable devices and vehicles because of their unique advantages including high energy density, low operation temperature, and environmental benignancy.<sup>1-4</sup> The wide application of DMFCs has been seriously hindered by the low efficiency of the anode reaction, namely the methanol oxidation reaction, because of its sluggish kinetics. Although Pt has been widely used as an electrocatalyst for methanol oxidation reaction (MOR), it has suffered from several severe problems including its scarcity, high cost, and poor operation durability.<sup>5-8</sup> The low efficiency can be mainly ascribed to the susceptible nature of Pt to poisonous MOR intermediates, especially CO. How to boost the intrinsic activity of Pt and alleviate the adsorption of poisonous CO species on Pt are thereby crucial for developing highly efficient and durable Pt-based MOR electrocatalysts.<sup>5,9-12</sup>

To enhance the antipoisoning ability of Pt-based catalysts, one strategy is via alloying Pt with other metals, such as Ru,<sup>13,14</sup> Cu,<sup>15,16</sup> Ni,<sup>17-21</sup> and Co,<sup>22</sup> to modify the electronic structure of Pt, thus weakening CO adsorption. In addition to the alloy system, some metal oxides<sup>23,24</sup> and hydroxides/oxyhydroxides<sup>25</sup> have been used to support Pt as they can facilitate the generation of abundant OH species for oxidative removal of adsorbed CO. Notably, the interface between Pt and the support plays a crucial role in improving the catalytic performance since it provides the channel for charge redistribution and vicinity for intermediate spillover. Therefore, engineering the interface structure is beneficial to the rational design of highly efficient catalysts. In recent years, inverse heterogeneous nanostructures, in which oxides or other compounds were decorated on the noble metal surface, have opened an avenue for the construction of interface structures.<sup>26-29</sup> Heterogeneous catalysts with an inverse interface structure, particularly oxide/metal interface structure, have shown extraordinary catalytic performance in water-gas shift,<sup>30,31</sup> water splitting<sup>32,33</sup> and CO oxidation,<sup>34,35</sup> mainly attributed to enhanced



dissociation of water or oxygen at interfacial sites. However, the inverse interface has been seldom studied in MOR, although it provides a well-suitable structural model for investigating the promotion effect that metal oxides exert on the noble metal surface.

Besides, constructing the inverse interface structure also faces challenges to its prevailing in electrocatalysis. Traditional bottom-up and top-down synthesis strategies are difficult to directly tune the subtle interface structure considering multiple variable synthesis parameters. Recently, electrochemical treatment-induced structural evolution of electrocatalysts has played a great role in optimizing catalyst structures to improve their efficiency in an electrocatalytic system.<sup>36-38</sup> For example, Strasser and co-workers realized experimental control over the extent of dealloying (thickness of Pt-rich shell) in Pt-Cu nanoparticles through cyclic voltammetry scans, which could tune the lattice strain of the Pt-rich shell and weaken chemisorption of oxygenated species in oxygen reduction reaction (ORR).<sup>39</sup> Liao et al. tuned the areal ratio of the water dissociation component to the noble metal surface on a nano-Pd surface through an electrochemical cycling strategy, thereby effectively balancing the water dissociation step and the hydrogen formation step in the hydrogen evolution reaction (HER).<sup>32</sup> Given the structural variability of electrocatalysts at a reductive or oxidative potential, it would be a promising strategy to construct the inverse interface, underlying the mechanism study of inverse catalysts in MOR.

Over the past few years, bismuth as a cheap and efficient promoter has been widely incorporated in Pt-based electrocatalysts.<sup>40-43</sup> Bismuth oxide/hydroxide, particularly in the alcohol oxidation reaction, has been inextricably linked to generating OH species for oxidative removal of adsorbed CO, whereas deep insight into the synergy between Pt and Bi remains vague.<sup>44,45</sup> Herein, with the help of density functional theory (DFT) calculations, we reveal that the inverse interface can increase the positive charge on its neighboring Pt atoms, resulting in weakened CO adsorption and strengthened OH adsorption. Under the theoretical guideline, we have successfully synthesized PtBi catalysts with this kind of inverse interface structure through electrochemical reconstruction. A comprehensive depiction of the inverse interface structure in terms of geometric and electronic features is provided by combining X-ray absorption

spectroscopy (XAS), ambient pressure X-ray photoelectron spectroscopy (APXPS), and electrochemical characterizations. The optimal Pt<sub>2</sub>Bi sample manifests a high mass activity of 4611 mA mg<sup>-1</sup><sub>Pt</sub>, which is 5.96 times higher than that of commercial Pt/C. Moreover, the Pt<sub>2</sub>Bi sample can maintain the mass activity of 1520 mA mg<sup>-1</sup><sub>Pt</sub> after a chronoamperometric test for 10000s, which is much higher than that of Pt/C (278 mA mg<sup>-1</sup><sub>Pt</sub>). This work highlights a comprehensive understanding of the inverse interface structure and its electronic effect on Pt sites, shedding light on the rational design of highly efficient electrocatalysts.

## 3.2 Experimental section

### 3.2.1 Chemicals

Chloroplatinic acid hexahydrate (H<sub>2</sub>PtCl<sub>6</sub>·6H<sub>2</sub>O), bismuth neodecanoate (C<sub>30</sub>H<sub>57</sub>BiO<sub>6</sub>), and polyvinyl pyrrolidone (PVP) were purchased from Sigma-Aldrich. Nafion alcohol solution (5 wt.%), commercial Pt/C catalyst (20 wt.%), and diethylene glycol (DEG) were purchased from Alfa Aesar. Methanol, acetone, ethanol, and potassium hydroxide (KOH) were bought from Sinopharm Chemical Reagent Co., Ltd. Carbon black (Vulcan XC-72) was purchased from Cabot Corporation. All reagents were used as received without further purification.

### 3.2.2 Synthesis of Pt<sub>2</sub>Bi nanoparticles

Pt<sub>2</sub>Bi nanoparticles were synthesized by a polyol reduction method using a standard Schlenk line. In a typical synthesis, 30 mg H<sub>2</sub>PtCl<sub>6</sub>·6H<sub>2</sub>O and 21 mg C<sub>30</sub>H<sub>57</sub>BiO<sub>6</sub> were dissolved in 3 mL DEG to prepare a precursor solution. 0.11 g PVP and 17 mL DEG were added into a 50 mL three-neck flask and then degassed for 15 minutes at 60 °C using a vacuum pump. Following, it was heated to 200 °C in a nitrogen atmosphere, and then the as-prepared precursor solution was quickly injected into the flask with vigorous stirring. The mixture was held at 200 °C for 30 minutes and then cooled to room temperature. Final products were collected by centrifugation (10000 rpm) and washed with acetone and ethanol (acetone: ethanol = 1:1) several times. Collected products were dried in a vacuum oven at 40 °C overnight. PtBi and Pt<sub>4</sub>Bi were synthesized with a

similar procedure except for changing the feeding ratio of Pt and Bi precursors to 1:1 and 4:1, respectively. The activation process was specified in the following section.

### 3.2.3 Characterizations

Transmission electron microscopy (TEM) was performed on a FEI TECNAI G2 operated at 200 kV. High-angle angular dark field (HAADF) images and elemental mapping were collected using a TECNAI G2 F20 electron microscope equipped with energy dispersive spectroscopy (EDS). The X-ray diffraction (XRD) patterns were recorded on an Empyrean diffractometer with Cu  $K\alpha$  radiation operated at 40 kV and 30 mA. X-ray photoelectron spectroscopy (XPS) measurements were conducted on a Kratos AXIS Untraded ultrahigh vacuum (UHV) surface analysis system and Al  $K\alpha$  was used as a light source. The elemental compositions were determined by inductively coupled plasma-atomic emission spectroscopy (ICP-AES, 710-ES, Varia). X-ray absorption near edge structure (XANES) and extended X-ray absorption fine structure (EXAFS) spectra were collected at 20BM beamline of the Advanced Photon Source (APS) operated by Argonne National Laboratory, U. S. and 44A beamline of Taiwan Photon Source (TPS) at the National Synchrotron Radiation Research Center (NSRRC), Taiwan, China. Standard Pt and Pb foils were used to do the energy calibration of XANES spectra at Pt  $L_3$ -edge and Bi  $L_2$ -edge, respectively. Ambient-pressure X-ray photoelectron spectroscopy (APXPS) was performed at 24A beamline of Taiwan Light Source (TLS) at the National Synchrotron Radiation Research Center (NSRRC), Taiwan, China. AP-XPS spectra were collected under three successive atmospheric conditions, changing from ultra-high vacuum (UHV-1,  $3 \times 10^{-8}$  bar) to near ambient pressure (AP-CO,  $5 \times 10^{-4}$  bar, CO atmosphere) and then back to ultra-high vacuum (UHV-2,  $3 \times 10^{-8}$  bar), with incipient light energy of 560 eV.

### 3.2.4 Electrochemical tests

CHI660 electrochemistry workstation was used to perform all the electrochemical tests under ambient conditions. A saturated calomel electrode (SCE) was used as the reference electrode, and Pt gauze was used as the counter electrode. Glass carbon electrode with a diameter of 3 mm was used as the working electrode. To prepare the ink solution, 1 mg

catalyst and 0.3 mg commercial carbon black (Vulkan X-72) were dispersed in a mixed solution ( $\text{H}_2\text{O}$ : ethanol: Nafion = 1:1:0.1) and ultrasonicated for 40 minutes to form a homogeneous mixture. A thin catalyst layer was cast on the working electrode surface with a constant Pt loading ( $28.3 \mu\text{g}\cdot\text{cm}^{-2}$ ) and dried at room temperature. PtBi catalysts were activated using chronoamperometry at  $-0.23 \text{ V}$  in  $1 \text{ M KOH}/1 \text{ M CH}_3\text{OH}$  solution. The activation time depended on the composition (PtBi, 2 h; Pt<sub>2</sub>Bi, 1 h; Pt<sub>4</sub>Bi, 0.5 h, and Pt/C, 1 h). Cyclic voltammetry (CV) curves were collected at a scan rate of  $50 \text{ mV}\cdot\text{s}^{-1}$  in  $1 \text{ M KOH}/1 \text{ M CH}_3\text{OH}$  solution. The peak current density normalized by the loading mass of Pt was used to estimate the catalytic activities of catalysts. The long-term stability test was conducted under chronoamperometry mode at  $-0.23 \text{ V}$  in  $1 \text{ M KOH}/1 \text{ M CH}_3\text{OH}$  solution. The regeneration of Pt<sub>2</sub>Bi catalyst after each cycle (10000 s per cycle) was realized by conducting several CV scans in  $1 \text{ M KOH}$  solution. For comparison, commercial Pt/C (20 wt. % of Pt nanoparticles supported on Vulkan X-72 carbon black, JM) was used as a reference with the same Pt loading.

### 3.2.5 CO-stripping experiments

The CO-stripping experiments were conducted in  $1 \text{ M KOH}$  solution. The potential was held at  $-0.96 \text{ V}$ . Meanwhile, CO gas was bubbled into the electrolyte for 30 minutes to create monolayer adsorption of CO on the catalyst surface, and then  $\text{N}_2$  was bubbled into the electrolyte to purge the CO dissolved into the electrolyte. Following, cyclic voltammograms were collected by applying the potential from  $-0.96$  to  $0.2 \text{ V}$  with a scan rate of  $50 \text{ mV s}^{-1}$ . The first cycle noted as “1<sup>st</sup> scan” was ascribed to the oxidative removal of surface-adsorbed CO. The second cycle noted as “2<sup>nd</sup> scan” was a typical CV curve of the catalyst in  $1 \text{ M KOH}$  solution.

### 3.2.6 DFT simulations

The quantum mechanics (QM) calculations were carried out using the VASP software, version 5.4.4. The Perdew, Burke, and Ernzerhof (PBE) flavor of density functional theory (DFT) with the post-stage DFT-D3 method was used to correct for London dispersion (van der Waals attraction) with Becke-Johnson damping. The projector augmented wave (PAW) method was used to account for core-valence interactions. The

kinetic energy cutoff for plane wave expansions was set to 400 eV, and reciprocal space was sampled by the  $\Gamma$ -centered Monkhorst-Pack scheme using a  $3 \times 3 \times 1$  K-point grid for all systems with a  $4 \times 4$  unit cell. The vacuum layer is at least  $15 \text{ \AA}$  above the surface. The convergence criteria are  $1 \times 10^{-5}$  eV energy differences for solving the electronic wave function. All geometries (atomic coordinates) were converged to within  $3 \times 10^{-2}$  eV/ $\text{\AA}$  for maximal components of forces. In this work, all free energies at 298.15 K were calculated as

$$G = E_{elec} + E_{ZPE} - T \times S_m^v \quad (3.1)$$

$E_{elec}$  is the electronic energy of the Pt/Pt<sub>2</sub>Bi\_A metal slab with adsorbed OH/CO molecule. The vibrational frequencies were evaluated for only surface adsorbates and were calculated. According to the calculated frequency results, zero-point energy (EZPE) and adsorption entropy  $S_m^v$  were obtained.

$$S_m^v = \sum_{\tilde{\nu}}^{\tilde{\nu}_i} R \left\{ \frac{\beta h c \tilde{\nu}}{e^{\beta h c \tilde{\nu}} - 1} - \ln(1 - e^{-\beta h c \tilde{\nu}}) \right\} \quad (3.2)$$

where  $R$  is gas constant,  $\beta$  is  $1/T * kb$  ( $kb$  is Boltzmann constant),  $h$  is Plank constant,  $c$  is light speed, and  $\nu$  is wave number.

### 3.2.7 Fourier transform (FT) and Wavelet transform (WT) of EXAFS

ATHENA software was used to do the energy calibration and background subtraction.<sup>46</sup> In the Fourier transform of EXAFS, the  $k$  space was set in a range from  $3.5$  to  $14.9 \text{ \AA}^{-1}$  with a  $k^3$  weighting being used. As a parallel mathematic transform to the Fourier transform, the wavelet transform involves the term of energy. It is a complementary tool to identify the contribution of scattering paths. Wavelet transform of EXAFS was performed using the Morlet wavelet, in which the program parameters  $\kappa$  and  $\sigma$  were set to 6 and 1, respectively. The  $k$  and  $R$  ranges were set to be  $0 - 14.9 \text{ \AA}^{-1}$  and  $0 - 6 \text{ \AA}$ , respectively. A  $k^3$  weighting was used.

### 3.3 Results and discussion

#### 3.3.1 DFT simulations

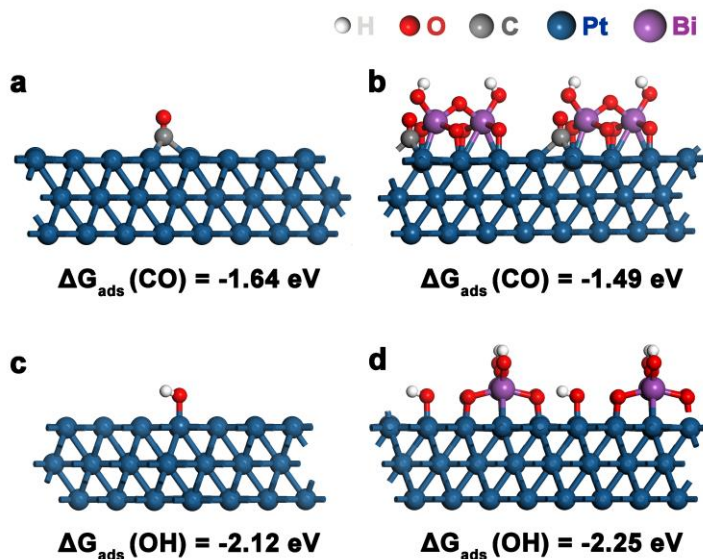


**Figure 3-1.** DFT simulations of the binding free energy of CO and OH species on surfaces of pristine Pt (111) (a and c) and Pt (111) with  $\text{BiO}_x(\text{OH})_y$  (b and d).

**Table 3-1** Adsorption properties of CO and OH species on Pt sites of  $\text{Pt}_2\text{Bi}_A$  based on DFT calculation.

	CO		OH		
Surface	Pt (111)	Pt- $\text{BiO}_x(\text{OH})_y$	Surface	Pt (111)	Pt- $\text{BiO}_x(\text{OH})_y$
C-O bond length (Å)	1.20	1.19	O-H bond length (Å)	0.98	1.00
C-Pt bond length (Å)	2.11	2.11	O-Pt bond length (Å)	1.98	1.95
Binding free energy $\Delta G(\text{CO})$ (eV)	-1.64	-1.50	Binding free energy $\Delta G(\text{OH})$ (eV)	-2.12	-2.25

To investigate the impact of the inverse interface on the catalyst surface, DFT calculations were performed based on two structural models, the Pt (111) surface and the Pt (111) surface with  $\text{BiO}_x(\text{OH})_y$ . For Pt decorated with  $\text{BiO}_x(\text{OH})_y$ , Pt (111) with three atomic layers in the bulk and two isolated  $\text{BiO}_x(\text{OH})_y$  on its surface was employed.

During the geometry optimizations, two layers of atoms in the bottom were fixed at their bulk positions, whereas the rest of the atoms were allowed to relax. Both O and Bi strongly bind on the interface as indicated by the short Pt-O and Pt-Bi distance. The binding free energies of CO and OH species were calculated (**Figure 3-1** and **Table 3-1**). The binding free energies of CO ( $\Delta G_{\text{ads}}(\text{CO})$ ) and OH ( $\Delta G_{\text{ads}}(\text{OH})$ ) on the Pt (111) surface are -1.64 eV and -2.12 eV, respectively. In contrast,  $\Delta G_{\text{ads}}(\text{CO})$  increases to -1.49 eV, and  $\Delta G_{\text{ads}}(\text{OH})$  decreases to -2.25 eV at neighboring Pt atoms along with  $\text{BiO}_x(\text{OH})_y$ , indicating the CO adsorption is weakened while OH adsorption is strengthened.

### 3.3.2 Morphology and composition studies

Inspired by DFT calculations, PtBi nanochains with a  $\text{BiO}_x(\text{OH})_y$ -Pt interface were delicately prepared through electrochemical reconstruction. In a typical synthesis, PtBi nanoparticles with controllable Pt/Bi ratios were synthesized through a polyol reduction method, in which chloroplatinic acid hexahydrate, bismuth neodecanoate, polyvinylpyrrolidone, and diethylene glycol were used as the metal precursors, surfactant and solvent, respectively. The as-prepared products were then subjected to a chronoamperometric treatment for different times at -0.23 V versus a saturated calomel electrode (SCE) to achieve the structural evolution in which treatment time was dependent on the Pt/Bi ratios. To confirm the formation of the proposed inverse interface structure,  $\text{Pt}_2\text{Bi}$  was taken as an example. The subscript indicates the feeding molar ratio of Pt/Bi precursors. Samples before and after electrochemical treatment are noted as  $\text{Pt}_2\text{Bi\_I}$  and  $\text{Pt}_2\text{Bi\_A}$ , respectively.

The structural evolution was first monitored by TEM.  $\text{Pt}_2\text{Bi\_I}$  consists of chain-like structures with an average diameter of 4.0 nm and plate-like structures with an average diameter of 20 nm (**Figure 3-2a**). The lattice spacing of  $\text{Pt}_2\text{Bi\_I}$  is measured to be about 0.225 nm (inset of **Figure 3-2a**), which can be indexed to the (111) facet of face-centered-cubic (fcc) Pt. After electrochemical treatment,  $\text{Pt}_2\text{Bi\_A}$  maintains its chain-like structures while the nanoplates disappear (**Figure 3-2b**). **Figure 3-2c** shows the elemental distribution of  $\text{Pt}_2\text{Bi\_I}$ , in which Pt and Bi elements disperse among all the particle regions and the average Pt/Bi atomic ratio is around 83.8:16.2 (**Figure 3-2e, bottom**). Chains and plates possess different compositions, and the Pt/Bi ratio is

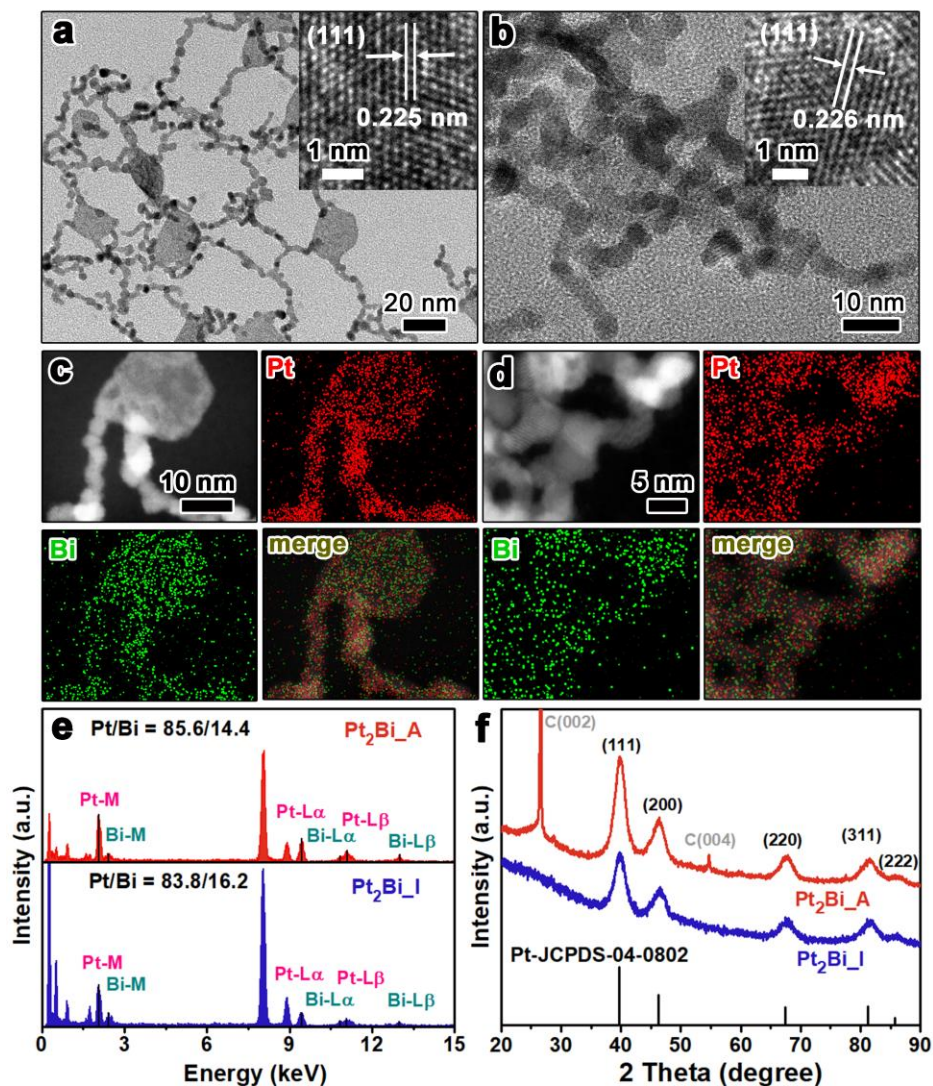


**Figure 3-2. TEM images and HRTEM images of (a) Pt<sub>2</sub>Bi\_I and (b) Pt<sub>2</sub>Bi\_A. HAADF-STEM images and elemental mapping of (c) Pt<sub>2</sub>Bi\_I and (d) Pt<sub>2</sub>Bi\_A. e) EDS spectra and f) XRD patterns of Pt<sub>2</sub>Bi\_I and Pt<sub>2</sub>Bi\_A, respectively.**

89.3:10.7 in chains while it is 56.8:43.2 in plates. **Figure 3-2d** shows a uniform elemental distribution after electrochemical treatment with a Pt/Bi ratio of 85.6:14.4 (**Figure 3-2e, top**). A slight increase in Pt/Bi ratio is ascribed to leaching out mainly from the plates during electrochemical treatment, which also gives a possible explanation for the disappearance of plates. The crystal phase of Pt<sub>2</sub>Bi\_I and Pt<sub>2</sub>Bi\_A was characterized by X-ray diffraction (XRD), in which diffraction peaks at  $2\theta = 39.7^\circ$ ,  $46.3^\circ$ ,  $67.3^\circ$ ,  $81.5^\circ$ , and



85.9° are indexed as facets of fcc Pt (**Figure 3-2f**). Two additional peaks at  $2\theta = 26.5^\circ$  and  $54.8^\circ$  for Pt<sub>2</sub>Bi\_A are assigned to carbon paper which is used as conductive support for collecting XRD samples.

### 3.3.3 Electronic structure study

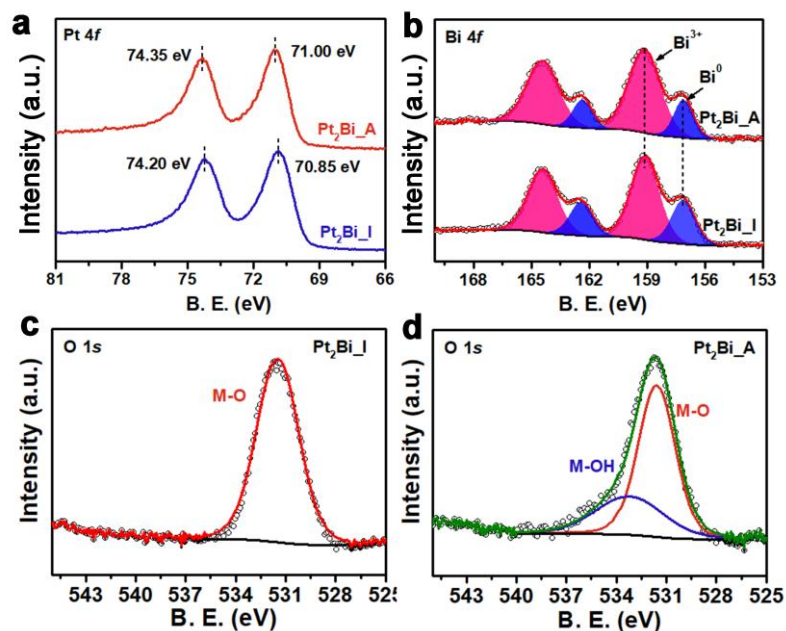


**Figure 3-3.** XPS spectra of Pt<sub>2</sub>Bi\_I and Pt<sub>2</sub>Bi\_A at a) Pt 4f and b) Bi 4f core levels. XPS spectra of c) Pt<sub>2</sub>Bi\_I and d) Pt<sub>2</sub>Bi\_A at O 1s core levels.

To get a deeper understanding of the surface chemistry of Pt<sub>2</sub>Bi, X-ray photoelectron spectroscopy (XPS) was used to track changes in the electronic structure of Pt<sub>2</sub>Bi\_I and Pt<sub>2</sub>Bi\_A. For Pt<sub>2</sub>Bi\_I, two peaks at 70.85 and 74.20 eV are assigned to 4f<sub>7/2</sub> and 4f<sub>5/2</sub> core levels of metallic Pt, respectively (**Figure 3-3a**). Pt 4f orbitals of Pt<sub>2</sub>Bi\_A shift to a higher binding energy by 0.15 eV compared to that of Pt<sub>2</sub>Bi\_I, suggesting higher oxidation state of Pt after electrochemical treatment. **Figure 3-3b** shows two sets of peaks of Bi 4f core levels, in which peaks at 157.14 and 162.46 eV are assigned to 4f<sub>7/2</sub> and 4f<sub>5/2</sub> core levels of metallic Bi while peaks at 159.12 and 164.42 eV are corresponding to 4f<sub>7/2</sub> and 4f<sub>5/2</sub> core levels of Bi<sup>3+</sup> species. Although no obvious peak shift is observed at the Bi 4f core levels, there is a noticeable decrease in metallic Bi after electrochemical treatment, which is confirmed by the decreasing integrated area ratio of

$\text{Bi}^0/\text{Bi}^{3+}$  from 0.43 to 0.28. The changes in the oxidation state of Pt and Bi should be driven by anodic electrochemical oxidation. Moreover, the O 1s spectrum of  $\text{Pt}_2\text{Bi}_A$  shows an extra peak at higher binding energy compared to that of  $\text{Pt}_2\text{Bi}_I$  (**Figure 3-3c and 3d**), which can be assigned to metal-OH (M-OH), suggesting that  $\text{Bi}^{3+}$  is mainly in the form of  $\text{BiO}_x(\text{OH})_y$ .<sup>47</sup>

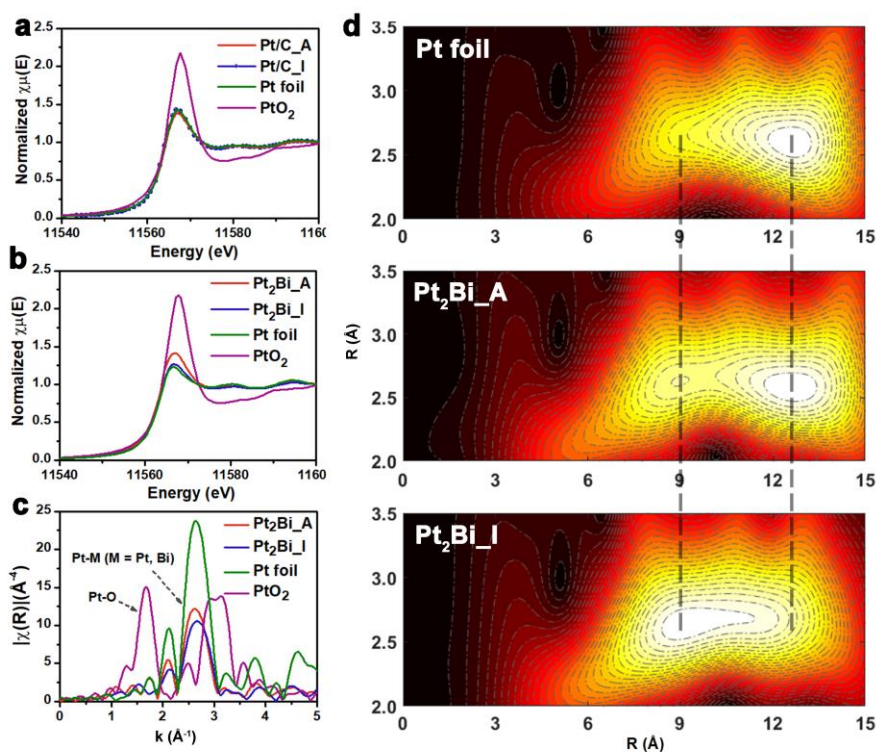


**Figure 3-4.** XANES spectra of a) Pt/C and b)  $\text{Pt}_2\text{Bi}$  before and after electrochemical treatment at Pt  $L_{3}$ -edge. Pt foil and  $\text{PtO}_2$  are used as references. Fourier transform c) and wavelet transform d) of Pt  $L_{3}$ -edge EXAFS of  $\text{Pt}_2\text{Bi}_I$  and  $\text{Pt}_2\text{Bi}_A$  with a  $k^3$  weighting. Pt foil and  $\text{PtO}_2$  are used as references.

X-ray absorption spectroscopy (XAS) was further conducted to obtain the local electronic structure and coordination environment. X-ray absorption near edge structure (XANES) and extended X-ray absorption fine structure (EXAFS) spectra were collected at Pt  $L_{3}$ -edge and Bi  $L_{2}$ -edge. Commercial 20 wt.% Pt/C catalyst was used for comparison.

**Figure 3-4a** shows that the XANES spectra of commercial Pt/C before and after the same electrochemical treatment at Pt  $L_{3}$ -edge both overlap with that of Pt foil, indicating that

Pt/C possesses the same local structure as Pt foil. The overlapping XANES spectra provide direct evidence for the absence of structural changes in Pt/C before and after electrochemical treatment. However, in the case of Pt<sub>2</sub>Bi catalyst, the whiteness intensity of Pt<sub>2</sub>Bi\_I catalyst is slightly higher than that of Pt foil while a noticeable enhancement is observed after electrochemical treatment (**Figure 3-4b**). The enhanced whiteness intensity indicates more unoccupied valence states at Pt sites (fewer electrons in the Pt 5d orbitals), keeping in line with XPS results and DFT calculation.

### 3.3.4 Local structure study

Fourier transform (phase-uncorrected) of EXAFS was carried out to study the coordination environment of Pt<sub>2</sub>Bi catalysts before and after electrochemical treatment (**Figure 3-4c**). The peak position in *R* space is related to the atomic distance between surrounding atoms and the absorber while the peak intensity is proportional to the coordination number of the corresponding surrounding atoms around the absorbing atom. Pt-metal (Pt-M) scattering paths contribute to the features around 2.6 Å. For Pt<sub>2</sub>Bi catalysts, Pt-M consists of two single scattering paths, Pt-Pt at a shorter radial distance and Pt-Bi at a slightly longer radial distance, which almost overlap with each other. The electrochemical treatment results in the Pt-M peak shifting to a shorter radial distance, which is presumably because of the increase of coordinated Pt and decrease of coordinated Bi around central Pt atoms as a result of structural evolution. Generally, fitting EXAFS in *R* space or *k* space is used to identify the local structure of the central atoms. Often an atom shell, i.e., of all the neighboring atoms at a specific distance, consists of only one type of atom. If such a shell comprises atoms of different elements, however, their waves cannot be separated by the Fourier transform approach. For example, due to the very close radial distance of Pt and Bi, Pt-Pt and Pt-Bi signals cannot be well separated by the Fourier transform of EXAFS of Pt<sub>2</sub>Bi before and after electrochemical treatment. Wavelet transform (WT) resolves the centers of the backscattering wave functions in energy (or *k*) space, therefore offering a straightforward way to discriminate different atoms within one atomic shell.<sup>48</sup> The WT contour plots show two intensity maxima at  $R = 2.58 \text{ \AA}$ ,  $k = 12.6 \text{ \AA}^{-1}$  and  $R = 2.63 \text{ \AA}$ ,  $k = 9 \text{ \AA}^{-1}$ , assigned to the Pt-Pt scattering path and Pt-Bi scattering path, respectively (**Figure 3-4d**).

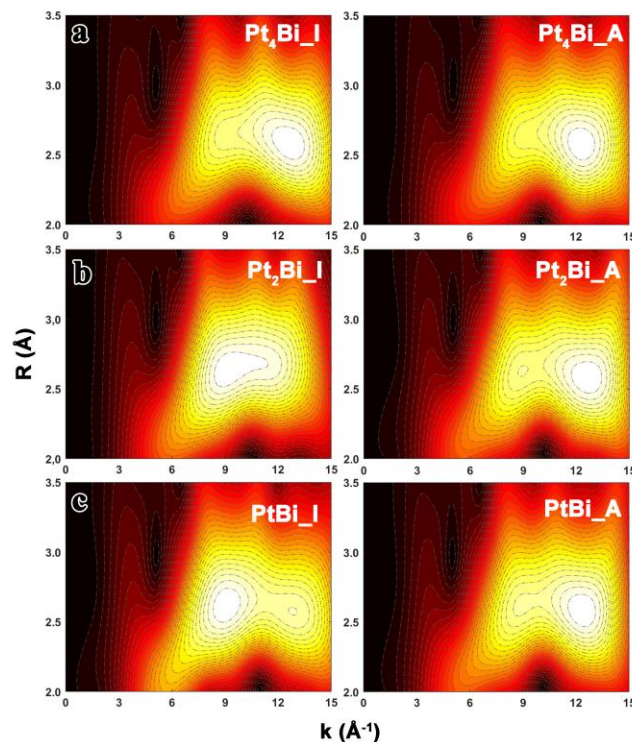


**Figure 3-5. WT contour plots of a) Pt<sub>4</sub>Bi, b) Pt<sub>2</sub>Bi, and c) PtBi before and after activation.**

The intensity maximum at the Bi dominating zone becomes weaker and Pt dominating zone shows an obvious enhancement, demonstrating that the coordination environment varies from the coexistence of Pt-Pt and Pt-Bi bonds to a Pt-Pt bond dominating situation after electrochemical treatment. The same trend is also observed in Pt<sub>4</sub>Bi and PtBi samples (**Figure 3-5**). The XANES spectra of Pt<sub>2</sub>Bi\_I and Pt<sub>2</sub>Bi\_A at Bi L<sub>2</sub>-edge show similar features to the Bi<sub>2</sub>O<sub>3</sub> spectrum but with a broadened whiteline peak (**Figure 3-6a**). The linear combination fitting toward spectra was conducted using Bi foil and Bi<sub>2</sub>O<sub>3</sub> as references (**Figure 3-6b and 3-6c**). The amount of Bi<sup>0</sup> species decreases significantly after electrochemical treatment which is consistent with XPS results.

Moreover, the absence of peaks from hydrogen underpotential deposition in the range of -0.9 V to -0.6 V (**Figure 3-6d**) further suggests the coverage of Bi<sup>3+</sup> species on the Pt surface. With the help of XPS, XANES, and EXAFS analysis, we now get a comprehensive understanding of the structural evolution of PtBi catalysts. After the

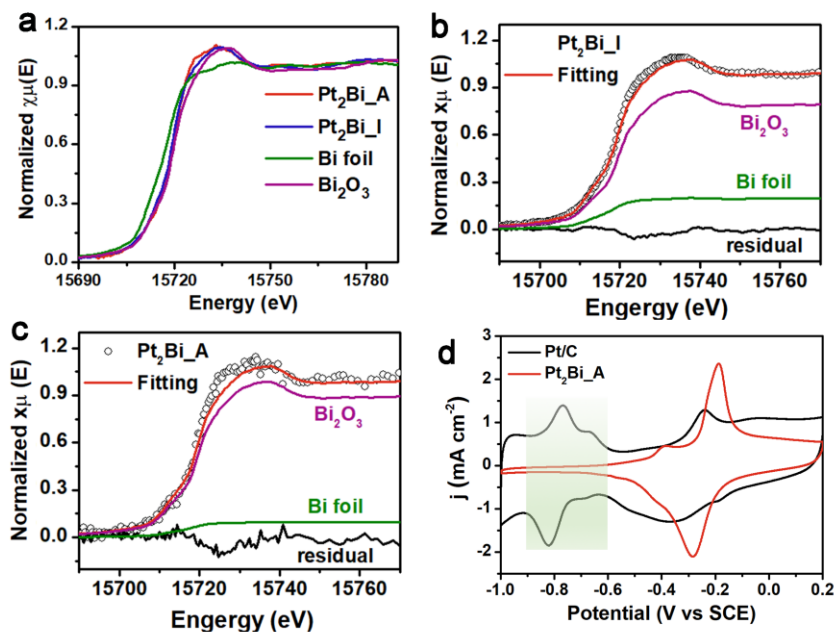


**Figure 3-6. a) XANES spectra of Pt<sub>2</sub>Bi\_I and Pt<sub>2</sub>Bi\_A at Bi L<sub>2</sub>-edge. Bi foil and Bi powder were used as references. b) and c) are linear combination fitting of XANES spectra of Pt<sub>2</sub>Bi\_I and Pt<sub>2</sub>Bi\_A, respectively. d) CV curves of Pt/C and Pt<sub>2</sub>Bi\_A in 1 M KOH with a scan rate of 50 mV s<sup>-1</sup>.**

electrochemical reconstruction, Bi species partially leach out from Pt<sub>2</sub>Bi\_I, generating a unique BiO<sub>x</sub>(OH)<sub>y</sub>-Pt inverse interface, resulting in Pt with an electron-deficient state.

### 3.3.5 CO resistance tests

To substantiate its enhanced antipoisoning ability toward CO adsorbate, ambient pressure X-ray photoelectron spectroscopy (AP-XPS) was conducted. Commercial Pt/C and Pt<sub>2</sub>Bi\_A were subjected to three successive atmospheric conditions, changing from ultrahigh vacuum (UHV-1,  $3 \times 10^{-8}$  bar) to near ambient pressure (AP-CO,  $5 \times 10^{-4}$  bar, CO atmosphere) and then back to ultra-high vacuum (UHV-2,  $3 \times 10^{-8}$  bar). In the case of Pt/C (**Figure 3-7a**), two peaks located at 71.30 and 74.65 eV are ascribed to Pt 4f<sub>7/2</sub> and 4f<sub>5/2</sub> core levels, respectively, with a clean surface (olive line). Subsequently switching to the CO atmosphere induces an obvious peak shift of 0.16 eV toward higher binding energy (red line), and the peak shift keeps constant even after pumping back to the initial ultra-high vacuum (blue line). The peak shift is triggered by adsorbed CO on Pt sites by

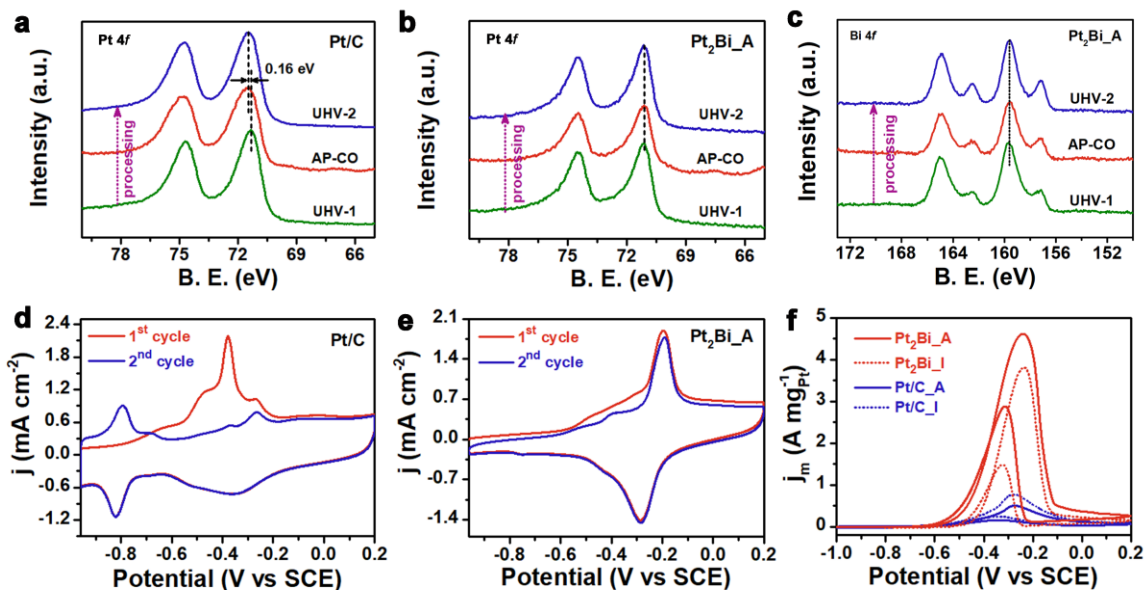


**Figure 3-7.** AP-XPS spectra of a) Pt/C and b) Pt<sub>2</sub>Bi\_A at Pt 4f and c) Bi 4f core levels under three successive atmospheric conditions. 1) Ultra-high vacuum (UHV-1, olive line); 2) CO atmosphere (AP-CO, red line); 3) ultra-high vacuum (UHV-2, blue line). The incipient X-ray energy is 560 eV. CO-stripping experiments of d) Pt/C and e) Pt<sub>2</sub>Bi\_A in 1 M KOH. Scanning rate is 50 mV s<sup>-1</sup>. f) CV curves of Pt/C and Pt<sub>2</sub>Bi\_A in 1 M KOH/1 M CH<sub>3</sub>OH before and after electrochemical treatment. Scanning rate is 50 mV s<sup>-1</sup>.

forming a chemical bond,<sup>49</sup> revealing its intrinsic nature of being poisoned. However, no peak shift is observed at Pt 4f (**Figure 3-7b**) and Bi 4f core levels (**Figure 3-7c**) in the case of Pt<sub>2</sub>Bi\_A, indicating an impressive CO tolerance capacity compared to Pt/C. Additionally, the CO-stripping experiments provide solid evidence for weakened CO adsorption in the electrolyte (**Figures 3-7d and 3-7e**). For Pt/C, two oxidation peaks are observed in the forward scan over a range of -0.5 V to -0.3 V, ascribed to CO oxidative removal on Pt.<sup>25</sup> Impressively, CV curves for Pt<sub>2</sub>Bi\_A in the first scan and the second scan almost overlap, indicating that CO molecules are barely adsorbed on Pt<sub>2</sub>Bi\_A. The enhanced CO tolerance is expected to derive from the electron-deficient state of Pt, which efficiently weakens CO adsorption. In addition, the removal of CO adsorbates can also be



facilitated by rich OH species from another Pt site or  $\text{BiO}_x(\text{OH})_y$  based on the bifunctional mechanism.<sup>6,25</sup>

To experimentally confirm the enhancement of the  $\text{BiO}_x(\text{OH})_y$ -Pt inverse interface structure on the catalytic performance of PtBi catalysts, the MOR activities of  $\text{Pt}_2\text{Bi}$  and commercial 20 wt.% Pt/C catalysts were evaluated in a typical three-electrode system using an electrolyte containing 1 M KOH and 1 M  $\text{CH}_3\text{OH}$ . CV curves of  $\text{Pt}_2\text{Bi}$  and Pt/C before and after electrochemical treatment are shown in **Figure 3-7f**. Peaks that appear at a high voltage in a forward scan are ascribed to methanol oxidation, while the peaks at a low voltage in a backward scan are assigned to the oxidation of intermediates.<sup>25</sup> Peak current density normalized by loading mass of Pt in the forward scan is used to estimate activities of catalysts. For  $\text{Pt}_2\text{Bi}$  catalyst, the mass activity increases from 3806 to 4611  $\text{mA mg}^{-1}_{\text{Pt}}$  after electrochemical treatment. However, in the case of commercial Pt/C, the mass activity decreases from 774 to 504  $\text{mA mg}^{-1}_{\text{Pt}}$ .

### 3.3.6 Electrochemical tests

To verify the activity enhancement induced by electrochemical treatment, PtBi nanoparticles with different compositions were synthesized by simply adjusting the feeding molar ratios of Pt and Bi precursors (**Figure 3-8a-c**). The feeding ratio has a great influence on the morphology of the nanoparticles. High Pt content prefers the growth of chain-like structures while a high Bi content prefers the formation of plate-like structures. It should be noticed that the fcc-Pt phase is dominating in all samples based on XRD patterns (**Figure 3-8d**). The activation phenomenon is universal for all PtBi catalysts, and the activation time is dependent on the Pt/Bi ratios, in which a longer treatment time is required for the higher Bi content. As shown in **Figure 3-8e**, specific mass activities of  $\text{Pt}_4\text{Bi}$ ,  $\text{Pt}_2\text{Bi}$  and PtBi are 2000, 4611, and 2480  $\text{mA mg}^{-1}_{\text{Pt}}$ , which are 1.17, 1.21, and 1.18 times their initial states (1713, 3806, and 2110  $\text{mA mg}^{-1}_{\text{Pt}}$ ). In the case of commercial Pt/C, the activity decays after a similar treatment (1 hour). The electrochemical treatment is critical for enhancing the catalytic activity of PtBi catalysts.  $\text{Pt}_2\text{Bi}$  manifests the highest activity among all samples, which is 2.31, 1.86, and 5.96 times higher than that of  $\text{Pt}_4\text{Bi}$ , PtBi, and pristine commercial Pt/C, respectively. In addition, the catalytic durability and recyclability of  $\text{Pt}_2\text{Bi}_A$  and Pt/C were evaluated in

a solution containing 1 M KOH and 1 M CH<sub>3</sub>OH by using chronoamperometric measurement at -0.23 V (**Figure 3-8f**). Pt<sub>2</sub>Bi\_A shows excellent durability as evidenced by the fact that a mass activity of 1520 mA mg<sup>-1</sup><sub>Pt</sub> can be maintained even after a continuous test for 10000s which is much higher than that of Pt/C (278 mA mg<sup>-1</sup><sub>Pt</sub>). The high activity and great durability of Pt<sub>2</sub>Bi\_A make it among one of the best MOR electrocatalysts reported so far (**Table 3-2**). Therefore, the existence of the BiO<sub>x</sub>(OH)<sub>y</sub>-Pt inverse interface can dramatically improve the catalytic performance toward MOR.

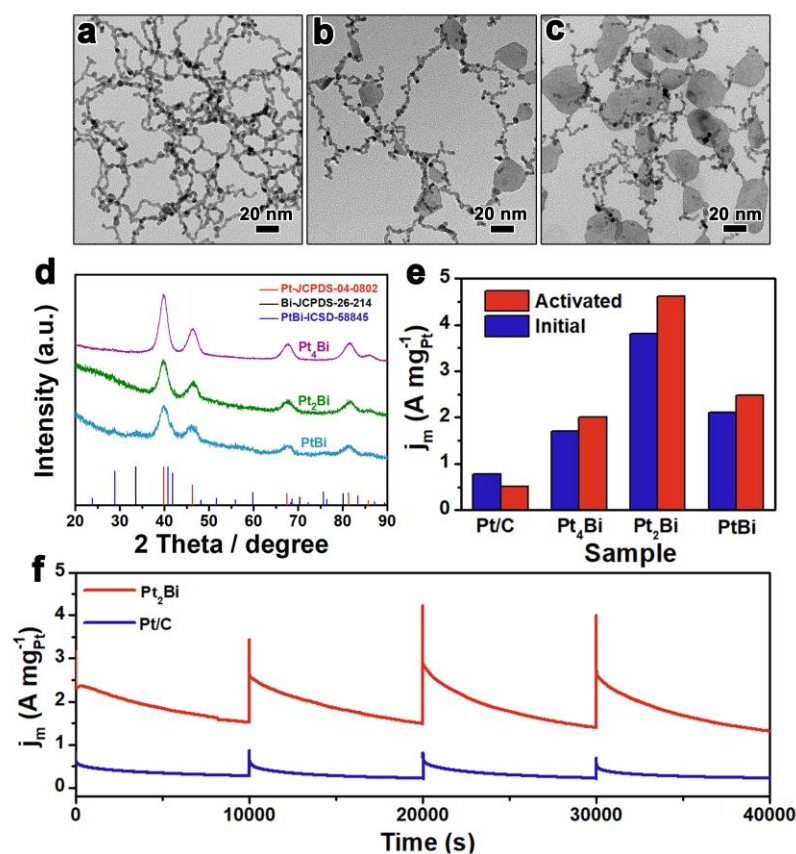


**Figure 3-8.** TEM images of PtBi nanoparticles with different compositions. a) Pt<sub>4</sub>Bi, b) Pt<sub>2</sub>Bi, and c) PtBi. d) XRD patterns of PtBi nanoparticles with different compositions. e) Mass activity of Pt/C, Pt<sub>4</sub>Bi, Pt<sub>2</sub>Bi, and PtBi towards MOR. f) Chronoamperogram of Pt<sub>2</sub>Bi and Pt/C in 1 M KOH/1 M CH<sub>3</sub>OH at -0.23 V vs. SCE.



**Table 3-2. A summary of the activities of MOR electrocatalysts in alkaline electrolytes reported in previous literature.**

Electrocatalyst	Electrolyte	Mass activity	Durability	Reference
<b>Pt<sub>2</sub>Bi nanochains</b>	<b>1 M KOH + 1 M CH<sub>3</sub>OH</b>	<b>4611 mA mg<sup>-1</sup>Pt</b>	<b>1520 mA mg<sup>-1</sup>Pt after 10000 s</b>	<b>This work</b>
Au <sub>3</sub> Ag nanoframes	0.5 M KOH + 2 M CH <sub>3</sub> OH	950 mA mg <sup>-1</sup> Au	502.1 mA mg <sup>-1</sup> Au after 7200 s	<i>Nat. Commun.</i> 2019, 10, 3782
Mesoporous Rh nanoparticles	1 M KOH + 1 M CH <sub>3</sub> OH	288 mA mg <sup>-1</sup> Rh	N/A	<i>Nat. Commun.</i> 2017, 8, 15581
Pt/Ni(OH) <sub>2</sub> /rGO	1 M KOH + 1 M CH <sub>3</sub> OH	1070 mA mg <sup>-1</sup> Pt	460 mA mg <sup>-1</sup> Pt after 3600 s	<i>Nat. Commun.</i> 2015, 6 10035
PtCu Nanoframes	0.5 M KOH + 1 M CH <sub>3</sub> OH	2260 mA mg <sup>-1</sup> Pt	N/A	<i>Adv. Mater.</i> 2016, 28, 8712
PdCu nanocages	1 M KOH + 1 M CH <sub>3</sub> OH	1090 mA mg <sup>-1</sup> Pd	~ 100 mA mg <sup>-1</sup> Pd after 2000 s	<i>J. Mater. Chem. A</i> 2018, 6, 3906
Pd-CeO <sub>2</sub> /NMCS	1 M KOH + 1 M CH <sub>3</sub> OH	1500 mA mg <sup>-1</sup> Pd	109.4 mA mg <sup>-1</sup> Pd after 3600 s	<i>ACS Catal.</i> 2019, 9, 6362
PtBi nanoplate	1 M NaOH + 1M CH <sub>3</sub> OH	4,820 mA mg <sup>-1</sup> Pt	~1500 mA mg <sup>-1</sup> Pt after 10000 s	<i>Nano Res.</i> 2019, 12, 429
Pt <sub>1</sub> Ni <sub>1</sub> /C	1 M KOH + 1 M CH <sub>3</sub> OH	~1750 mA mg <sup>-1</sup> Pt	N/A	<i>Nano Res.</i> 2018, 11, 2058
Rh nanowires	1 M KOH + 1 M CH <sub>3</sub> OH	722 mA mg <sup>-1</sup> Rh	25 mA mg <sup>-1</sup> Rh after 6000 s	<i>Nano Res.</i> 2019, 12, 211
Pd <sub>59</sub> Cu <sub>33</sub> Ru <sub>8</sub> Nanosuperstructures	1 M KOH + 1 M CH <sub>3</sub> OH	1660.8 mA mg <sup>-1</sup> Pd	1046 mA mg <sup>-1</sup> Pd after 250 cycles	<i>ACS Appl. Mater. Interfaces</i> 2019, 11, 42123
PdCo nanowires	1 M KOH + 1 M CH <sub>3</sub> OH	1205 mA mg <sup>-1</sup> Pd	24.5 mA mg <sup>-1</sup> Pd after 2000 s	<i>ACS Appl. Mater. Interfaces</i> 2018, 10, 29965
AgAu@Pt nanoframes	0.2 M KOH + 1 M CH <sub>3</sub> OH	483.1 mA mg <sup>-1</sup> Pt	~160 mA mg <sup>-1</sup> Pt after 1500 s	<i>Nanoscale</i> 2018, 10, 2231

### 3.4 Conclusions

In conclusion, we have demonstrated the formation of the BiO<sub>x</sub>(OH)<sub>y</sub>-Pt inverse interface through electrochemical reconstruction. Guided by DFT calculations, and combining XAS, AP-XPS, and electrochemical characterizations, we revealed that the incorporation of BiO<sub>x</sub>(OH)<sub>y</sub> could tailor the electronic structure and local coordination environment of Pt, resulting in weakened CO and strengthened OH at Pt sites. Moreover, it is worth

noting that  $\text{BiO}_x(\text{OH})_y$  also can provide rich OH species for oxidative removal of adsorbed CO. The synergy between the electronic effect and bifunctional effect strengthens the resistance to poisonous CO species. In virtue of the  $\text{BiO}_x(\text{OH})_y$ -Pt inverse interface, the optimal  $\text{Pt}_2\text{Bi}$  sample manifests a mass activity of  $4611 \text{ mA mg}^{-1}_{\text{Pt}}$ , which is 5.96 times higher than that of commercial Pt/C and shows excellent durability as retained  $1520 \text{ mA} \cdot \text{mg}^{-1}_{\text{Pt}}$  after a chronoamperometric test for 10,000 seconds. This work emphasizes the rational engineering of the interfaces in the composite electrocatalysts and provides deeper insight into the structure-property relationship, offering great opportunities for the fabrication of high-performance electrocatalysts for green energy technologies.

### 3.5 Reference

- (1) Aricò, A. S.; Srinivasan, S.; Antonucci, V. DMFCs: From fundamental aspects to technology development. *Fuel Cells* **2001**, *1* (2), 133.
- (2) Zhao, X.; Yin, M.; Ma, L.; Liang, L.; Liu, C.; Liao, J.; Lu, T.; Xing, W. Recent advances in catalysts for direct methanol fuel cells. *Energy & Environmental Science* **2011**, *4* (8), 2736.
- (3) Kakati, N.; Maiti, J.; Lee, S. H.; Jee, S. H.; Viswanathan, B.; Yoon, Y. S. Anode catalysts for direct methanol fuel cells in acidic media: Do we have any alternative for Pt or Pt–Ru? *Chemical Reviews* **2014**, *114* (24), 12397.
- (4) Feng, Y.; Liu, H.; Yang, J. A selective electrocatalyst-based direct methanol fuel cell operated at high concentrations of methanol. *Science Advances* **2017**, *3* (6), e1700580.
- (5) Liu, H.; Liu, K.; Zhong, P.; Qi, J.; Bian, J.; Fan, Q.; Ren, K.; Zheng, H.; Han, L.; Yin, Y.; Gao, C. Ultrathin Pt–Ag alloy nanotubes with regular nanopores for enhanced electrocatalytic activity. *Chemistry of Materials* **2018**, *30* (21), 7744.
- (6) Tong, Y.; Yan, X.; Liang, J.; Dou, S. X. Metal-based electrocatalysts for methanol electro-oxidation: Progress, opportunities, and challenges. *Small* **2019**, *17* (9), 1904126.
- (7) Zhang, T.; Sun, Y.; Li, X.; Li, X.; Liu, D.; Liu, G.; Li, C.; Fan, H. J.; Li, Y. PtPdAg hollow nanodendrites: Template-free synthesis and high electrocatalytic activity for methanol oxidation reaction. *Small Methods* **2020**, *4* (1), 1900709.
- (8) Liu, Z.; Qi, J.; Liu, M.; Zhang, S.; Fan, Q.; Liu, H.; Liu, K.; Zheng, H.; Yin, Y.; Gao, C. Aqueous synthesis of ultrathin platinum/non-noble metal alloy nanowires

for enhanced hydrogen evolution activity. *Angewandte Chemie International Edition* **2018**, *57* (36), 11678.

- (9) Yang, Y.; Luo, M.; Zhang, W.; Sun, Y.; Chen, X.; Guo, S. Metal surface and interface energy electrocatalysis: Fundamentals, performance engineering, and opportunities. *Chem* **2018**, *4* (9), 2054.
- (10) Xia, Z.; Zhang, X.; Sun, H.; Wang, S.; Sun, G. Recent advances in multi-scale design and construction of materials for direct methanol fuel cells. *Nano Energy* **2019**, *65*, 104048.
- (11) Feng, Q.; Zhao, S.; He, D.; Tian, S.; Gu, L.; Wen, X.; Chen, C.; Peng, Q.; Wang, D.; Li, Y. Strain engineering to enhance the electrooxidation performance of atomic-layer Pt on intermetallic Pt<sub>3</sub>Ga. *Journal of the American Chemical Society* **2018**, *140* (8), 2773.
- (12) Wu, X.; Jiang, Y.; Yan, Y.; Li, X.; Luo, S.; Huang, J.; Li, J.; Shen, R.; Yang, D.; Zhang, H. Tuning surface structure of Pd<sub>3</sub>Pb/Pt<sub>n</sub>Pb nanocrystals for boosting the methanol oxidation reaction. *Advanced Science* **2019**, *6* (24), 1902249.
- (13) Ma, S.-Y.; Li, H.-H.; Hu, B.-C.; Cheng, X.; Fu, Q.-Q.; Yu, S.-H. Synthesis of low Pt-based quaternary PtPdRuTe nanotubes with optimized incorporation of Pd for enhanced electrocatalytic activity. *Journal of the American Chemical Society* **2017**, *139* (16), 5890.
- (14) Huang, L.; Zhang, X.; Wang, Q.; Han, Y.; Fang, Y.; Dong, S. Shape-control of Pt–Ru nanocrystals: Tuning surface structure for enhanced electrocatalytic methanol oxidation. *Journal of the American Chemical Society* **2018**, *140* (3), 1142.
- (15) Zhang, Z.; Luo, Z.; Chen, B.; Wei, C.; Zhao, J.; Chen, J.; Zhang, X.; Lai, Z.; Fan, Z.; Tan, C.; Zhao, M.; Lu, Q.; Li, B.; Zong, Y.; Yan, C.; Wang, G.; Xu, Z. J.; Zhang, H. One-pot synthesis of highly anisotropic five-fold-twinned PtCu nanoframes used as a bifunctional electrocatalyst for oxygen reduction and methanol oxidation. *Advanced Materials* **2016**, *28* (39), 8712.
- (16) Li, H.-H.; Fu, Q.-Q.; Xu, L.; Ma, S.-Y.; Zheng, Y.-R.; Liu, X.-J.; Yu, S.-H. Highly crystalline PtCu nanotubes with three dimensional molecular accessible and restructured surface for efficient catalysis. *Energy & Environmental Science* **2017**, *10* (8), 1751.
- (17) Huang, J.; Liu, Y.; Xu, M.; Wan, C.; Liu, H.; Li, M.; Huang, Z.; Duan, X.; Pan, X.; Huang, Y. PtCuNi tetrahedra catalysts with tailored surfaces for efficient alcohol oxidation. *Nano Letters* **2019**, *19* (8), 5431.
- (18) Zhang, W.; Yang, Y.; Huang, B.; Lv, F.; Wang, K.; Li, N.; Luo, M.; Chao, Y.; Li, Y.; Sun, Y.; Xu, Z.; Qin, Y.; Yang, W.; Zhou, J.; Du, Y.; Su, D.; Guo, S. Ultrathin

PtNiM (M = Rh, Os, and Ir) nanowires as efficient fuel oxidation electrocatalytic materials. *Advanced Materials* **2019**, *31* (15), 1805833.

- (19) Li, M.; Duanmu, K.; Wan, C.; Cheng, T.; Zhang, L.; Dai, S.; Chen, W.; Zhao, Z.; Li, P.; Fei, H.; Zhu, Y.; Yu, R.; Luo, J.; Zang, K.; Lin, Z.; Ding, M.; Huang, J.; Sun, H.; Guo, J.; Pan, X.; Goddard, W. A.; Sautet, P.; Huang, Y.; Duan, X. Single-atom tailoring of platinum nanocatalysts for high-performance multifunctional electrocatalysis. *Nature Catalysis* **2019**, *2* (6), 495.
- (20) Lu, S.; Li, H.; Sun, J.; Zhuang, Z. Promoting the methanol oxidation catalytic activity by introducing surface nickel on platinum nanoparticles. *Nano Research* **2018**, *11* (4), 2058.
- (21) Yang, P.; Yuan, X.; Hu, H.; Liu, Y.; Zheng, H.; Yang, D.; Chen, L.; Cao, M.; Xu, Y.; Min, Y.; Li, Y.; Zhang, Q. Solvothermal synthesis of alloyed PtNi colloidal nanocrystal clusters (CNSs) with enhanced catalytic activity for methanol oxidation. *Advanced Functional Materials* **2018**, *28* (1), 1704774.
- (22) Xia, B. Y.; Wu, H. B.; Li, N.; Yan, Y.; Lou, X. W.; Wang, X. One-pot synthesis of Pt–Co alloy nanowire assemblies with tunable composition and enhanced electrocatalytic properties. *Angewandte Chemie International Edition* **2015**, *54* (12), 3797.
- (23) Tao, L.; Shi, Y.; Huang, Y.-C.; Chen, R.; Zhang, Y.; Huo, J.; Zou, Y.; Yu, G.; Luo, J.; Dong, C.-L.; Wang, S. Interface engineering of Pt and CeO<sub>2</sub> nanorods with unique interaction for methanol oxidation. *Nano Energy* **2018**, *53*, 604.
- (24) Dung van, D.; Adilbish, G.; Le, T. D.; Nguyen, T. T. D.; Lee, I.-H.; Yu, Y.-T. Au@CeO<sub>2</sub> nanoparticles supported Pt/C electrocatalyst to improve the removal of CO in methanol oxidation reaction. *Journal of Catalysis* **2019**, *377*, 589.
- (25) Huang, W.; Wang, H.; Zhou, J.; Wang, J.; Duchesne, P. N.; Muir, D.; Zhang, P.; Han, N.; Zhao, F.; Zeng, M.; Zhong, J.; Jin, C.; Li, Y.; Lee, S.-T.; Dai, H. Highly active and durable methanol oxidation electrocatalyst based on the synergy of platinum-nickel hydroxide-graphene. *Nature Communications* **2015**, *6* (1), 10035.
- (26) Cao, L.; Liu, W.; Luo, Q.; Yin, R.; Wang, B.; Weissenrieder, J.; Soldemo, M.; Yan, H.; Lin, Y.; Sun, Z.; Ma, C.; Zhang, W.; Chen, S.; Wang, H.; Guan, Q.; Yao, T.; Wei, S.; Yang, J.; Lu, J. Atomically dispersed iron hydroxide anchored on Pt for preferential oxidation of CO in H<sub>2</sub>. *Nature* **2019**, *565* (7741), 631.
- (27) Chen, Z.; Liu, Y.; Liu, C.; Zhang, J.; Chen, Y.; Hu, W.; Deng, Y. Engineering the metal/oxide interface of Pd nanowire@CuO<sub>x</sub> electrocatalysts for efficient alcohol oxidation reaction. *Small* **2020**, *16* (4), 1904964.
- (28) Feng, Y.; Yang, C.; Fang, W.; Huang, B.; Shao, Q.; Huang, X. Anti-poisoned oxygen reduction by the interface modulated Pd@NiO core@shell. *Nano Energy* **2019**, *58*, 234.

- (29) Liu, Z.; Huang, E.; Orozco, I.; Liao, W.; Palomino, R. M.; Rui, N.; Duchoň, T.; Nemšák, S.; Grinter, D. C.; Mahapatra, M.; Liu, P.; Rodriguez, J. A.; Senanayake, S. D. Water-promoted interfacial pathways in methane oxidation to methanol on a CeO<sub>2</sub>-Cu<sub>2</sub>O catalyst. *Science* **2020**, *368* (6490), 513.
- (30) Rodriguez, J. A.; Ma, S.; Liu, P.; Hrbek, J.; Evans, J.; Pérez, M. Activity of CeO<sub>x</sub> and TiO<sub>x</sub> nanoparticles grown on Au(111) in the water-gas shift reaction. *Science* **2007**, *318* (5857), 1757.
- (31) Yan, H.; Yang, C.; Shao, W.-P.; Cai, L.-H.; Wang, W.-W.; Jin, Z.; Jia, C.-J. Construction of stabilized bulk-nano interfaces for highly promoted inverse CeO<sub>2</sub>/Cu catalyst. *Nature Communications* **2019**, *10* (1), 3470.
- (32) Liao, H.; Wei, C.; Wang, J.; Fisher, A.; Sritharan, T.; Feng, Z.; Xu, Z. J. A multisite strategy for enhancing the hydrogen evolution reaction on a nano-Pd surface in alkaline media. *Advanced Energy Materials* **2017**, *7* (21), 1701129.
- (33) Zhao, Z.; Liu, H.; Gao, W.; Xue, W.; Liu, Z.; Huang, J.; Pan, X.; Huang, Y. Surface-engineered PtNi-O nanostructure with record-high performance for electrocatalytic hydrogen evolution reaction. *Journal of the American Chemical Society* **2018**, *140* (29), 9046.
- (34) Sun, Y.-N.; Giordano, L.; Goniakowski, J.; Lewandowski, M.; Qin, Z.-H.; Noguera, C.; Shaikhutdinov, S.; Pacchioni, G.; Freund, H.-J. The interplay between structure and CO oxidation catalysis on metal-supported ultrathin oxide films. *Angewandte Chemie-International Edition* **2010**, *49* (26), 4418.
- (35) Yang, F.; Graciani, J.; Evans, J.; Liu, P.; Hrbek, J.; Sanz, J. F.; Rodriguez, J. A. Co oxidation on inverse CeO<sub>x</sub>/Cu(111) catalysts: High catalytic activity and ceria-promoted dissociation of O<sub>2</sub>. *Journal of the American Chemical Society* **2011**, *133* (10), 3444.
- (36) Jiang, H.; He, Q.; Zhang, Y.; Song, L. Structural self-reconstruction of catalysts in electrocatalysis. *Accounts of Chemical Research* **2018**, *51* (11), 2968.
- (37) Jin, S. Are metal chalcogenides, nitrides, and phosphides oxygen evolution catalysts or bifunctional catalysts? *ACS Energy Letters* **2017**, *2* (8), 1937.
- (38) Zheng, X.; Zhang, B.; De Luna, P.; Liang, Y.; Comin, R.; Voznyy, O.; Han, L.; García de Arquer, F. P.; Liu, M.; Dinh, C. T.; Regier, T.; Dynes, J. J.; He, S.; Xin, H. L.; Peng, H.; Prendergast, D.; Du, X.; Sargent, E. H. Theory-driven design of high-valence metal sites for water oxidation confirmed using in situ soft x-ray absorption. *Nature Chemistry* **2018**, *10* (2), 149.
- (39) Strasser, P.; Koh, S.; Anniyev, T.; Greeley, J.; More, K.; Yu, C.; Liu, Z.; Kaya, S.; Nordlund, D.; Ogasawara, H.; Toney, M. F.; Nilsson, A. Lattice-strain control of the activity in dealloyed core-shell fuel cell catalysts. *Nature Chemistry* **2010**, *2* (6), 454.

- (40) Zhang, B.-W.; Lai, W.-H.; Sheng, T.; Qu, X.-M.; Wang, Y.-X.; Ren, L.; Zhang, L.; Du, Y.; Jiang, Y.-X.; Sun, S.-G.; Dou, S.-X. Ordered platinum-bismuth intermetallic clusters with Pt-skin for a highly efficient electrochemical ethanol oxidation reaction. *Journal of Materials Chemistry A* **2019**, *7* (10), 5214.
- (41) Qin, Y.; Luo, M.; Sun, Y.; Li, C.; Huang, B.; Yang, Y.; Li, Y.; Wang, L.; Guo, S. Intermetallic hcp-PtBi/fcc-Pt core/shell nanoplates enable efficient bifunctional oxygen reduction and methanol oxidation electrocatalysis. *ACS Catalysis* **2018**, *8* (6), 5581.
- (42) Feng, Y.; Shao, Q.; Lv, F.; Bu, L.; Guo, J.; Guo, S.; Huang, X. Intermetallic PtBi nanoplates boost oxygen reduction catalysis with superior tolerance over chemical fuels. *Advanced Science* **2020**, *7* (1), 1800178.
- (43) Yuan, X.; Jiang, X.; Cao, M.; Chen, L.; Nie, K.; Zhang, Y.; Xu, Y.; Sun, X.; Li, Y.; Zhang, Q. Intermetallic PtBi core/ultrathin Pt shell nanoplates for efficient and stable methanol and ethanol electro-oxidation. *Nano Research* **2019**, *12* (2), 429.
- (44) Yuan, X.; Zhang, Y.; Cao, M.; Zhou, T.; Jiang, X.; Chen, J.; Lyu, F.; Xu, Y.; Luo, J.; Zhang, Q.; Yin, Y. Bi(OH)<sub>3</sub>/PdBi composite nanochains as highly active and durable electrocatalysts for ethanol oxidation. *Nano Letters* **2019**, *19* (7), 4752.
- (45) Yang, M. Catalytic activities of PtBi nanoparticles toward methanol electrooxidation in acid and alkaline media. *Journal of Power Sources* **2013**, *229*, 42.
- (46) Ravel, B.; Newville, M. ATHENA, ARTEMIS, HEPHAESTUS: Data analysis for X-ray absorption spectroscopy using IFEFFIT. *Journal of synchrotron radiation* **2005**, *12* (Pt 4), 537.
- (47) Zu, M. Y.; Zhang, L.; Wang, C.; Zheng, L. R.; Yang, H. G. Copper-modulated bismuth nanocrystals alter the formate formation pathway to achieve highly selective CO<sub>2</sub> electroreduction. *Journal of Materials Chemistry A* **2018**, *6* (35), 16804.
- (48) Muñoz, M.; Argoul, P.; Farges, F. Continuous Cauchy wavelet transform analyses of EXAFS spectra: A qualitative approach. *American Mineralogist* **2003**, *88* (4), 694.
- (49) Tao, F.; Dag, S.; Wang, L.-W.; Liu, Z.; Butcher, D. R.; Bluhm, H.; Salmeron, M.; Somorjai, G. A. Break-up of stepped platinum catalyst surfaces by high CO coverage. *Science* **2010**, *327* (5967), 850.

## Chapter 4

### 4 The Role of Bismuth in Suppressing the CO-poisoning in Alkaline Methanol Electrooxidation: Switching the Reaction from CO to Formate Pathway

#### 4.1 Introduction

Direct methanol fuel cells (DMFCs) have long been considered as promising power sources for portable devices and vehicles thanks to their low operation temperature, high energy conversion efficiency, eco-friendly nature, and sustainable sources.<sup>1-4</sup> Pt-based catalysts are commonly used in anodic methanol oxidation but severely suffer from the poisoning effect of surface-adsorbed intermediates, such as CO.<sup>5-7</sup> It is generally accepted that methanol can be oxidized to CO<sub>2</sub> via a dual-path mechanism, i.e., via the indirect pathway (CO<sub>ads</sub> as the intermediate) or the direct pathway (formate as the intermediate).<sup>8,9</sup> Given the CO-poisoning effect, it will be a promising way to improve the catalyst efficiency by suppressing the indirect pathway while enhancing the direct.

Conventional wisdom to address the CO-poisoning issue is combining Pt with oxophilic metals or metal oxides/hydroxides, which can enrich the OH adsorbates (OH<sub>ads</sub>) on the catalyst surface and reduce the overpotential of CO<sub>ads</sub> electrooxidation.<sup>10-12</sup> However, almost no Pt-based catalysts can entirely circumvent the formation of CO<sub>ads</sub> no matter in the acidic or alkaline electrolytes, in other words, these catalysts are more or less suffering from the poisoning of CO<sub>ads</sub>. Compared with other additives, Bi species can surprisingly prohibit the CO<sub>ads</sub> adsorption at Pt active sites and substantially improve the catalytic activity and durability in the alkaline electrolyte.<sup>13-16</sup> It is found that the CO molecule barely adsorbs on the Bi-modified Pt catalysts in the CO-stripping experiments,<sup>17,18</sup> and in situ infrared absorption spectroscopy also does not probe the signal from CO<sub>ads</sub> in the methanol oxidation.<sup>19</sup> Bi-modified Pt catalysts seem to inhibit the indirect pathway in the alkaline electrolyte, but there is still no consensus on that. Interestingly, when switched to the acidic electrolyte, a large amount of CO molecules adsorb on the Bi-modified Pt catalysts in the CO-stripping experiments, comparable to the case of pure Pt catalysts.<sup>17</sup> This discrepancy indicates the complexity of how Bi

works, which cannot be simply explained in terms of the electronic effect or bifunctional effect.<sup>20-22</sup> Therefore, elucidating the real role of Bi in improving the methanol oxidation of Pt, especially in the alkaline electrolyte, is of significance to its practical applications.

In this work, we contrive a PtBi model catalyst consisting of a PtBi surface alloy and a Pt-rich core to systematically study the functionality of Bi as a promoter in the methanol oxidation reaction. It is found that the PtBi catalyst can efficiently circumvent the indirect pathway and concurrently enhance the direct pathway of methanol oxidation in the alkaline electrolyte. The Bi species play great roles in this process: 1) The charge redistribution between Bi and Pt atoms weakens the adsorption of CO<sub>ads</sub> thermodynamically; 2) Bi enriches the OH<sub>ads</sub> species on the catalyst surface, and the competitive adsorption of OH<sub>ads</sub> and CO<sub>ads</sub> at Pt sites reduces the CO<sub>ads</sub> kinetically; 3) The presence of abundant OH<sub>ads</sub> meets the prerequisite of the formation of formate. We have successfully extended this concept to modify the commercial Pt/C catalyst and realized its facile and large-scale production by a microwave-assisted strategy. This work aims to unveil the role of Bi in mitigating the CO-poisoning on Pt catalysts, underlying the design of CO-tolerance electrocatalysts for fuel cells.

## 4.2 Experimental section

### 4.2.1 Chemicals

Chloroplatinic acid hexahydrate (H<sub>2</sub>PtCl<sub>6</sub>·6H<sub>2</sub>O), bismuth neodecanoate (Bi(NE)<sub>3</sub>), tetramethylammonium bromide (TMAB), and polyvinyl pyrrolidone (PVP, MW = 29000 g/mol) were purchased from Sigma-Aldrich. Nafion alcohol solution (5 wt. %) and commercial Pt/C (20 % Pt by mass) were purchased from Alfa Aesar. Ethelene glycol (EG) was purchased from TCI. Methanol, acetone, ethanol, and potassium hydroxide (KOH) were bought from Sinopharm Chemical. Reagent Co., Ltd. Carbon black (Vulcan XC-72) was purchased from Cabot Corporation. All reagents were used as received without further purification.



#### 4.2.2 Synthesis of Pt NPs

Pt NPs were synthesized according to a previously reported method.<sup>23</sup> In a typical synthesis, 1.5 mmol TMAB, and 2 mmol PVP were dissolved into 17 mL 20 mL EG, and then the mixture was heated to 180 °C under the protection of a N<sub>2</sub> atmosphere. 0.1 mmol H<sub>2</sub>PtCl<sub>6</sub>·6H<sub>2</sub>O, pre-dissolved in 3 mL EG, was quickly injected into the hot solution. The solution was kept at 180 °C for 20 minutes and then cooled down to room temperature. The final product was collected by centrifugation (10000 rpm) and washed with ethanol and acetone (ethanol: acetone = 1:1) several times. Finally, Pt NPs were obtained by drying in a vacuum oven at 40 °C overnight.

#### 4.2.3 Synthesis of Bi-modified Pt catalysts

The synthesis of Bi-modified Pt catalysts adopted a two-step method. First, Pt NPs, the substrate, were synthesized using the same procedure as introduced above. Second, after the Pt precursor was injected for 20 minutes, a proper amount of Bi precursor, pre-dissolved in 3 mL EG, was injected into the solution. The mixture was kept at 180 °C for another 20 minutes and then cooled down to room temperature. The final product was collected by centrifugation and washed with ethanol and acetone several times, and finally was dried in a vacuum oven at 40 °C overnight. The feeding amounts of Bi(NE)<sub>3</sub> for Pt<sub>95</sub>Bi<sub>5</sub>, Pt<sub>92</sub>Bi<sub>8</sub>, and Pt<sub>78</sub>Bi<sub>22</sub> were 0.011, 0.043, and 0.1 mmol, respectively.

#### 4.2.4 Synthesis of Bi-modified commercial Pt/C catalysts (PtBi/C)

The synthesis of PtBi/C adopted a microwave-assisted method. In a typical synthesis, 25 mg commercial Pt/C and 0.011 mmol Bi(NE)<sub>3</sub> were well mixed in a reactor tube with 20 mL EG. The tube was set into the microwave reactor. The temperature was set to 180 °C with a heating rate of 10 °C per minute. The mixture was kept at 180 °C for 15 minutes and then cooled down to room temperature. The final product was collected by centrifugation (10000 rpm) and washed with ethanol several times, and then dried in a vacuum oven at 40 °C overnight.

#### 4.2.5 Characterizations

Transmission electron microscopy (TEM) was performed on a FEI TECNAI G2 operated at 200 kV. High-angle angular dark field (HAADF) and elemental mapping images were collected using a TECNAI G2 F20 electron microscope equipped with energy dispersive spectroscopy (EDS). X-ray diffraction patterns were recorded on an Empyrean diffractometer with a Cu K $\alpha$  light source operated at 40 kV and 30 mA. X-ray photoelectron spectroscopy (XPS) was conducted on a Kratos AXIS Untraded ultrahigh vacuum surface analysis system and Al K $\alpha$  was used as the light source. Elemental compositions were determined by inductively coupled plasma-atomic emission spectroscopy (ICP-OES, 710-ES, Varia), EDS, and XPS analysis. X-ray absorption spectra Pt L<sub>3,2</sub>- and Bi L<sub>3</sub>-edges were collected at 20 BM beamline of Advanced Photon Source (APS) operated by Argonne National Laboratory, U.S. X-ray absorption spectra at Bi L<sub>2</sub>-edge were collected 44A beamline of Taiwan Photon Source (TPS) at the National Synchrotron Radiation Research Center (NSRRC), Taiwan, China.

#### 4.2.6 Data analysis of XAS spectra

Athena was used to do the energy calibration and normalization toward the XAS spectra. In the XANES fitting at Pt L<sub>3</sub>-edge, an arctangent background was subtracted from the normalized XANES spectra, and the integrated area under the whitenline was used to compare the number of d electron holes. In the EXAFS region of Pt L<sub>3</sub>-edge, the k space was obtained by subtracting an arctangent background from the EXAFS spectra, and it was further converted into the R space through Fourier transform, in which the k range was set from 2.6 to 14.5 Å<sup>-1</sup> and a k<sup>2</sup> weighting was used. Artemis was used to fit the EXAFS in R space.

#### 4.2.7 Catalytic performance tests

CHI660 electrochemistry workstation was used to perform all electrochemical tests under ambient conditions. Glass carbon electrode with a diameter of 3 mm was used as the working electrode. Saturated calomel electrode (SCE) and Pt gauze were used as the reference electrode and counter electrode, respectively. The potential used in data

analysis was converted to the potential referenced to a reversible hydrogen electrode (RHE) according to the following equation:

$$E(\text{vs. RHE}) = E(\text{vs. SCE}) + 0.242 + 0.059pH \quad (4.1)$$

In the preparation of ink solutions, 1 mg catalyst and 0.3 mg commercial carbon black (Vulcan X-72) were dispersed in a mixed solution (water: ethanol: Nafion = 1:1:0.1), and the mixture underwent ultrasonication for 40 minutes. The ink solution was cast on the working electrode with a constant loading amount of catalyst ( $28.3 \mu\text{g cm}^{-2}$ ) and dried at room temperature. Cyclic voltammograms of catalysts were collected in the 1 M KOH or 1 M KOH/CH<sub>3</sub>OH solution at a scan rate of  $50 \text{ mV s}^{-1}$ . The long-term durability test was conducted under chronoamperometry mode at 0.81 V vs. RHE in 1 M KOH/CH<sub>3</sub>OH solution. The current density was normalized to the mass of the catalyst rather than the mass of Pt to evaluate the catalytic performance.

#### 4.2.8 CO-stripping experiments

The working electrode was prepared according to the above description. The CO-stripping experiments were conducted in 1 M KOH solution. The potential was held at 0.1 V vs. RHE. Meanwhile, CO gas was bubbled into the electrolyte for 30 minutes to create monolayer adsorption of CO on the catalyst surface, and then N<sub>2</sub> was bubbled into the electrolyte to purge the CO dissolved into the electrolyte. Following, cyclic voltammograms were collected by applying the potential from 0.1 to 1.26 V with a scan rate of  $50 \text{ mV s}^{-1}$ . The first cycle noted as “CO<sub>ads</sub>” was ascribed to the oxidative removal of surface-adsorbed CO. The second cycle noted as “clean” was a typical CV curve of the catalyst in 1 M KOH solution.

#### 4.2.9 In situ electrochemical Fourier-transform infrared (FTIR) absorption spectroscopy

In situ FTIR spectra were collected by an Agilent Cary 660 FTIR spectrometer equipped with a liquid-cooling MCT detector, using the homemade spectroelectrochemical cell. Two working modes (attenuated total reflection (ATR) mode and external reflection mode (IRAS)) were respectively employed to probe the surface-adsorbed species and

dissolved species.<sup>24-26</sup> In detail, in situ ATR surface-enhanced infrared absorption spectroscopy (SEIRAS) was used to investigate the surface species especially the CO<sub>ads</sub> species adsorbed at the Pt NPs and Pt<sub>92</sub>Bi<sub>8</sub> catalysts surfaces when the cyclic voltammogram was scanning in the KOH/CH<sub>3</sub>OH solution with the scan rate of 5 mV/s. The time interval for each sample spectrum collection is 5 s, which means that each spectrum was coadded by at least 44 interferograms. The Pt NPs and Pt<sub>92</sub>Bi<sub>8</sub> catalysts were dipped on the ca. 60 nm thick Au nanofilm which was chemically deposited on the basal plane of a hemicylindrical Si prism in advance, which has been detailly described elsewhere.<sup>27,28</sup> On the other hand, the in-situ IRAS measurement was performed to analyze the discovered species such as CO<sub>2</sub>, carbonate, and formate in this work, being similar to the previous work.<sup>29,30</sup> The prepared catalyst ink was dropped on the glassy carbon electrode ( $d = 5$  mm), which was used as the working electrode. The working electrode was pressed onto the CaF<sub>2</sub> prism surface to form a ca. 10  $\mu$ m thin-layer contained electrolyte while collecting the in-situ spectra. The infrared spectrum was also collected every 5 seconds to ensure that each spectrum was formed by at least 44 interferograms. All spectra are expressed in absorbance units defined as  $\log(I/I_0)$ , where  $I$  and  $I_0$  represent the absorption intensities at the sample and reference conditions, respectively.

## 4.3 Results and discussion

### 4.3.1 Morphology and crystalline structure study

The construction of the PtBi model catalyst consisting of a PtBi surface alloy on a Pt-rich core adopted a two-step method. Typically, Pt nanoparticles (NPs), as the substrate, were synthesized according to a previously reported method,<sup>23</sup> and then Bi was introduced using a hot-injection method to guarantee the structural uniformity (see details in the Supporting Information). Chloroplatinic acid hexahydrate and bismuth neodecanoate, ethylene glycol, polyvinylpyrrolidone, and tetramethylammonium bromide (TMAB) were used as precursors, reductant, surfactant, and capping agent, respectively. As shown in **Figure 4-1a**, the Pt nanoparticles have an average diameter of 5.92 nm, exposing a high percentage of (100) facets due to the selective protection of Br<sup>-</sup>. To study the structural and electronic properties, Pt<sub>92</sub>Bi<sub>8</sub> was taken as an example, of which the

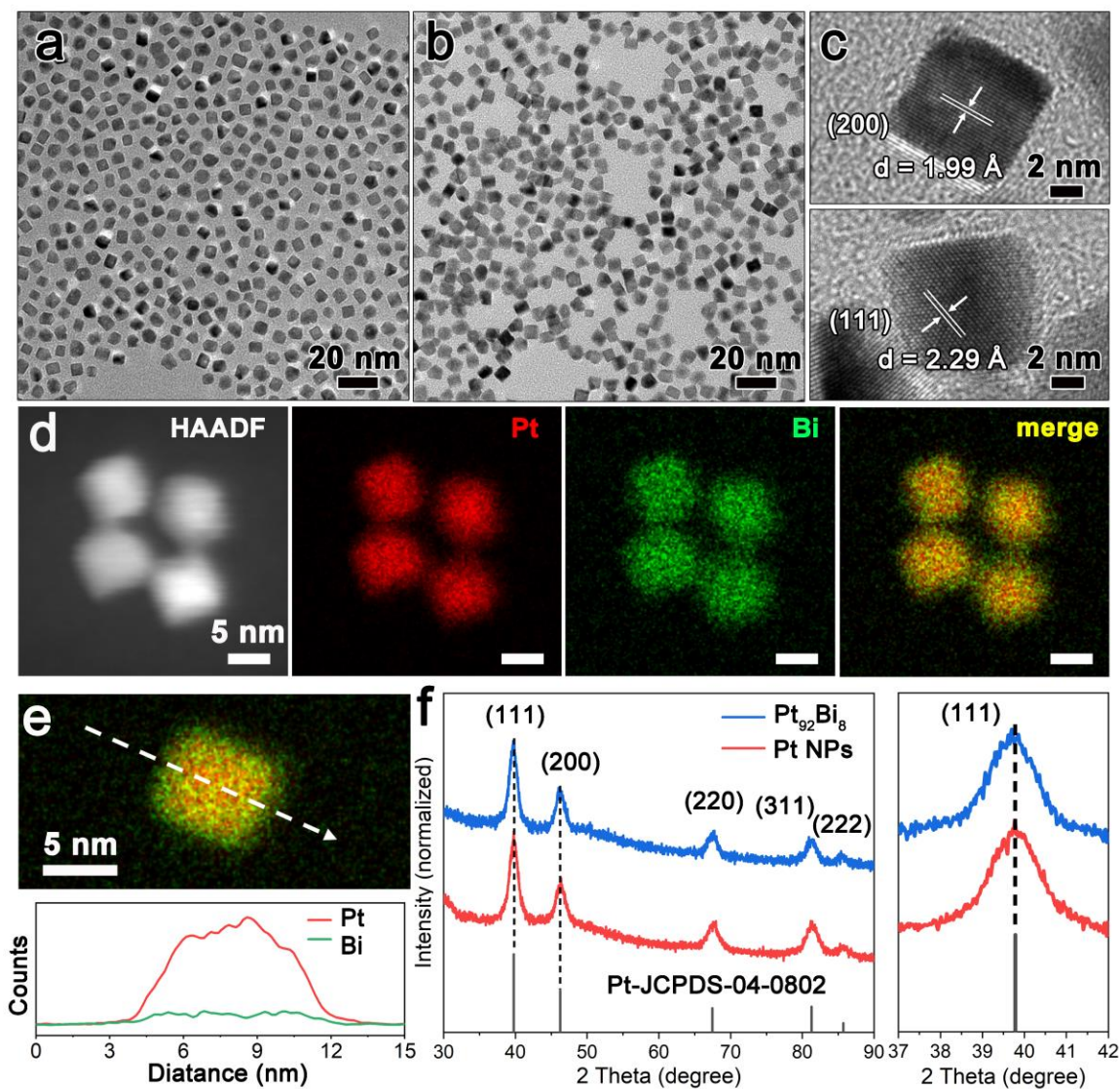


**Figure 4-1.** TEM images of a) Pt NPs and b) Pt<sub>92</sub>Bi<sub>8</sub>, respectively. c) HRTEM images of Pt<sub>92</sub>Bi<sub>8</sub>. d) Elemental mapping images of Pt<sub>92</sub>Bi<sub>8</sub>. e) Line scanning image (top) and profile (bottom) of Pt<sub>92</sub>Bi<sub>8</sub>. f) XRD patterns of Pt NPs and Pt<sub>92</sub>Bi<sub>8</sub> (left) and the zoom-in image of the (111) facet from 37° to 42° (right).

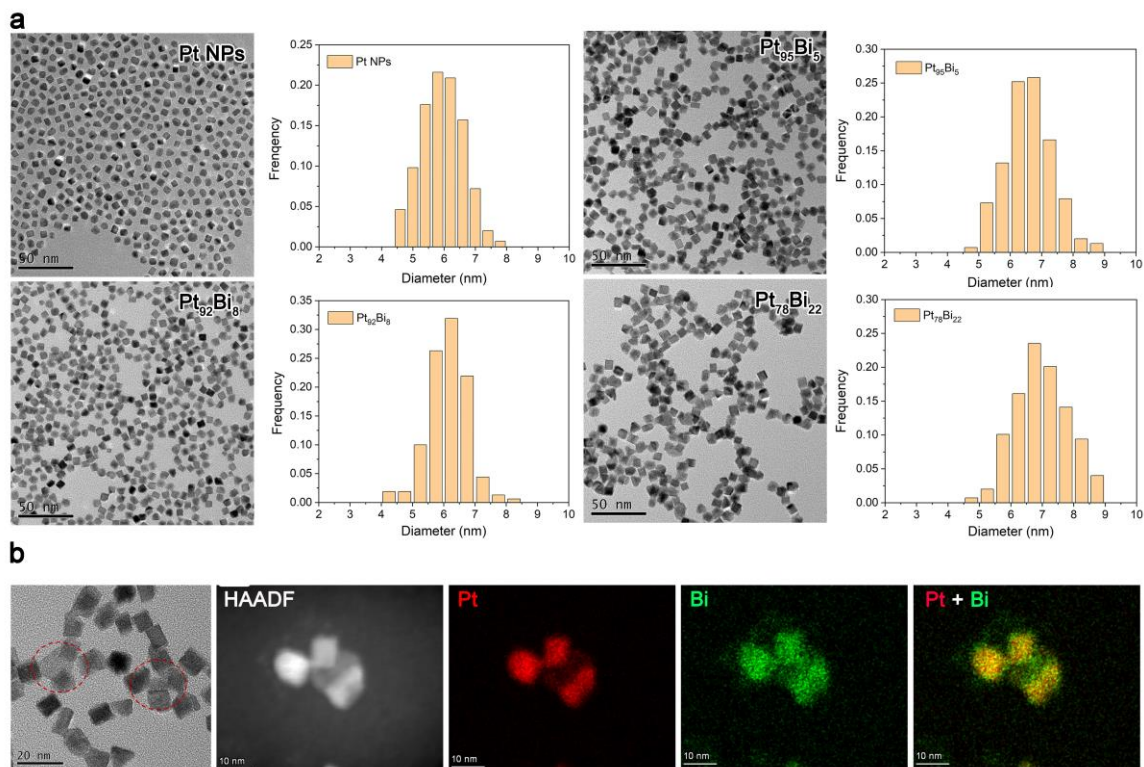


**Figure 4-2. a) TEM images and size-distribution statistics of Pt NPs, Pt<sub>92</sub>Bi<sub>8</sub>, Pt<sub>95</sub>Bi<sub>5</sub>, and Pt<sub>78</sub>Bi<sub>22</sub>. b) TEM and elemental mapping images of Pt<sub>78</sub>Bi<sub>22</sub>.**

subscript indicates the molar ratio of corresponding elements determined by inductively coupled plasma-optical emission spectroscopy (ICP-OES). The introduction of Bi does not induce noticeable changes in the particle size (average = 6.13 nm) due to the low content of Bi (**Figures 4-1b**). The high-resolution transmission electron microscopy (HRTEM) images show that the lattice spacings are 1.99 and 2.29 Å, close to that of the (200) and (111) facets of face-centered cubic (fcc) Pt (**Figure 4-1c**). The energy-dispersive X-ray spectroscopy (EDS) shows that Pt and Bi distribute homogeneously among the whole particle (at least in a few layers near the surface), suggesting the formation of a PtBi alloy structure (**Figure 4-1d**). The line scanning profile further confirms this homogeneity (**Figure 4-1e**). The XRD patterns indicate that Pt<sub>92</sub>Bi<sub>8</sub> keeps the fcc crystalline structure as Pt NPs, of which peaks around  $2\theta = 39.8^\circ$ ,  $46.3^\circ$ ,  $67.5^\circ$ ,  $81.3^\circ$ , and  $85.7^\circ$  are assigned to (111), (200), (220), (311), and (222) facets (**Figure 4-1f**, left), respectively. However, diffraction peaks slightly shift to the lower angle compared

to that of Pt NPs. Taking the (111) as an example, the peak shifts from  $39.78^\circ$  of Pt NPs to  $39.69^\circ$  of  $\text{Pt}_{92}\text{Bi}_8$  (**Figure 4-1f**, right), suggesting that Bi atoms diffuse into the Pt lattice and expand the lattice parameters as Bi possesses a relatively large atomic size. To precisely identify the structure and optimize the catalytic performance, PtBi catalysts with different molar ratios have been synthesized by tuning the feeding ratio of precursors. Little change is observed in the particle sizes of both  $\text{Pt}_{95}\text{Bi}_5$  and  $\text{Pt}_{78}\text{Bi}_{22}$  (**Figure 4-2a**), but freestanding Bi species appear when the Bi content reaches 22 % (**Figure 4-2b**), which is helpful to interpret the following spectra and voltammograms.

### 4.3.2 Electronic structure study

To probe the electronic properties of PtBi model catalysts, X-ray photoelectron spectroscopy (XPS) was performed at Pt and Bi 4f core levels. **Figure 4-3a** shows that the metallic Pt 4f<sub>7/2</sub> core level of  $\text{Pt}_{92}\text{Bi}_8$  (70.41 eV) slightly shifts to the lower binding energy compared to that of Pt NPs (70.46 eV). Meanwhile, the metallic Bi 4f<sub>7/2</sub> core level of  $\text{Pt}_{92}\text{Bi}_8$  locates at higher binding energy (156.33 eV) than that of Bi powder (156.49 eV, **Figure 4-3b**). The opposite shifting trend in the metallic Pt and Bi 4f core levels indicates the strong interaction between Pt and Bi atoms, and charge transfer from Bi to Pt takes place. Besides, Bi is prone to be oxidized upon exposure to air due to its oxophilicity, which explains the peaks of bismuth oxides in the Bi powder. Apart from bismuth oxides, signals from BiOBr are also probed in the case of  $\text{Pt}_{92}\text{Bi}_8$  because of the existence of bromide ions (from the TMAB). However, these surface-adsorbed species will not bother the catalytic performance since they can be easily removed upon cyclic voltammetry. As a powerful surface-sensitive characterization technique, XPS is also used to quantitatively analyze the surface composition (**Table 4-1**). The Bi content based on XPS analysis is much higher than that measured by ICP-OES and energy-dispersive X-ray spectroscopy (EDS), which means that Bi species are abundant in the near-surface layers and suggests the formation of a PtBi surface alloy. For example,  $\text{Pt}_{92}\text{Bi}_8$  has a Bi content of 25.2 % based on XPS, much higher than 8 % and 8.1 % from ICP-OES and EDS, respectively.



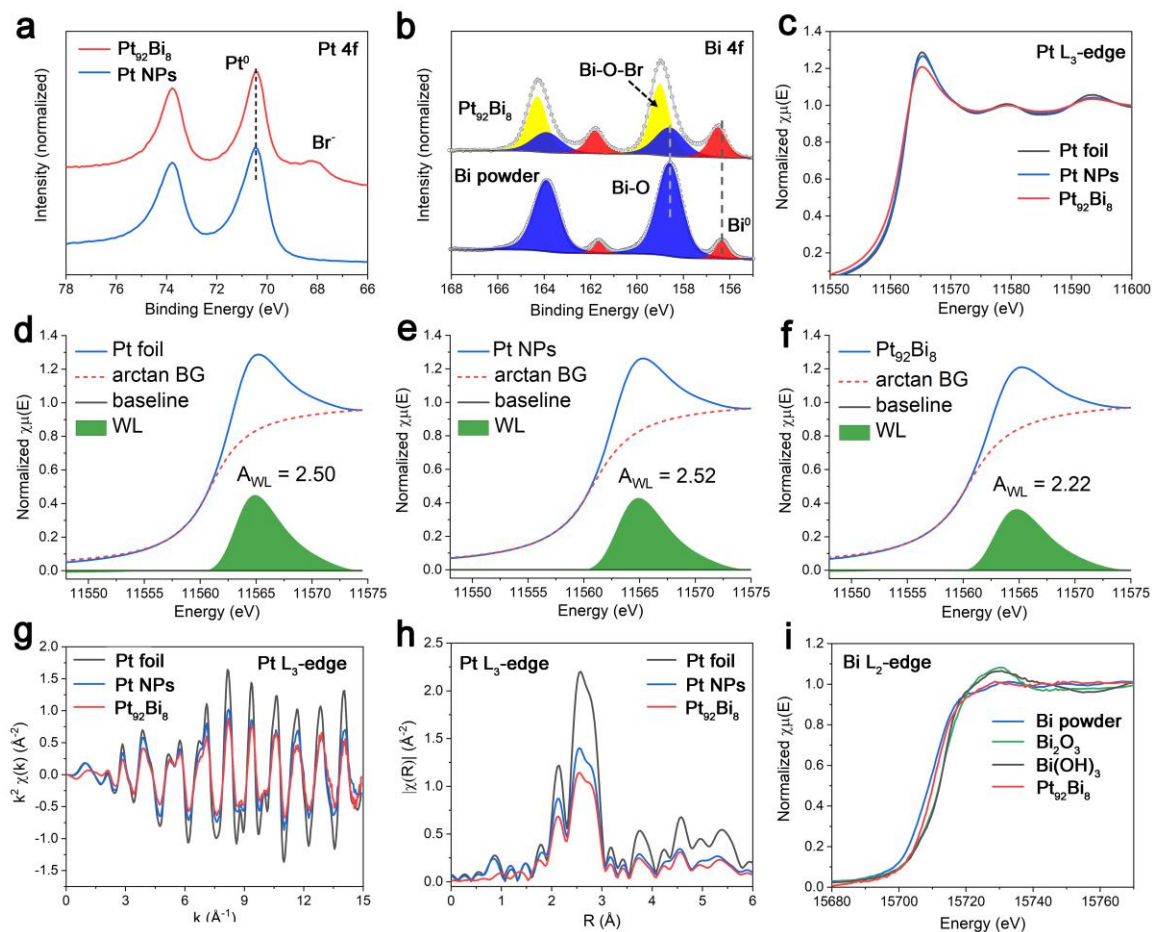


**Figure 4-3.** XPS spectra at a) Pt and b) Bi 4f core levels. c) XANES spectra at Pt L<sub>3</sub>-edge. The whiteline fitting of d) Pt foil, e) Pt NPs, and f) Pt<sub>92</sub>Bi<sub>8</sub> at Pt L<sub>3</sub>-edge. g) EXAFS spectra at Pt L<sub>3</sub>-edge in k space, a k<sup>2</sup> weighting is used .h) Fourier transformed EXAFS at Pt L<sub>3</sub>-edge in R space. A k<sup>2</sup> weighting is used. i) XANES spectra at Bi L<sub>2</sub>-edge.

**Table 4-1.** The molar ratio of Pt and Bi in precursors and in PtBi nanoparticles determined by various characterization techniques.

Samples	Feeding ratio by mole Pt: Bi	Measured ratio by mole		
		ICP	EDS	XPS
Pt NPs	100:0	-	-	-
Pt <sub>95</sub> Bi <sub>5</sub>	90:10	95.4:4.6	94.8:5.2	90.9:9.1
Pt <sub>92</sub> Bi <sub>8</sub>	70:30	92:8	91.9:8.1	74.8:25.2
Pt <sub>78</sub> Bi <sub>22</sub>	50:50	77.9:22.1	75.2:24.8	64.3:35.7



To obtain a deeper understanding of its electronic properties and local structure, X-ray absorption fine structure spectra, including X-ray absorption near-edge structure (XANES) and extended X-ray absorption fine structure (EXAFS), were collected at Pt L<sub>3,2</sub>- and Bi L<sub>3,2</sub>-edges. **Figure 4-3c** shows the XANES spectra recorded at Pt L<sub>3</sub>-edge in which the sharp peak at the edge jump is known as the whiteness (WL), and it arises from the transition from the Pt 2p<sub>3/2</sub> to the narrow unoccupied states just above the Fermi level with 5d<sub>5/2, 3/2</sub> characters. A reduction in Pt L<sub>3</sub>-edge WL intensity is observed for Pt<sub>92</sub>Bi<sub>8</sub> relative to Pt foil and Pt NPs. More accurately, the WL area (A<sub>WL</sub>), by integrating the area under the WL after extracting an arctangent background (arctan BG), shrinks upon alloying with Bi (**Figures 4-3d to 4-3f**), indicating a decrease of 5d Pt holes. In other words, Pt gains 5d electrons in the alloy. In the EXAFS region, the Pt<sub>92</sub>Bi<sub>8</sub> and Pt NPs show a smaller amplitude of oscillations compared to Pt foil (**Figure 4-3c**). This shrinkage in the amplitude indicates a smaller particle size due to more surface atoms with unsaturated coordination.

To better interpret the spectra, the k<sup>2</sup>-weighted  $\chi(k)$  (**Figure 4-3g**) was Fourier transformed into the R space, where the peak position is related to the bond distance (with a phase correction term) between the adsorber and surrounding atoms, and the magnitude is proportional to the coordination number of surrounding atoms (**Figure 4-3h**). The peak at 2.6 Å should be assigned to the Pt-Pt scattering path. However, no signal of Pt-Bi scattering path is observed because of the low Bi content as well as the small amplitude of Bi backscattering wave. The fitting results of EXAFS at Pt L<sub>3</sub>-edge are shown in **Table 4-2**. The coordination numbers (CNs) of Pt in Pt NPs and Pt<sub>92</sub>Bi<sub>8</sub> are 9.36 and 7.71, respectively, much smaller than fully coordinated Pt (CN = 12) due to their small particle sizes. However, the introduction of Bi can further decrease the Pt coordination number even though they share a similar particle size, which suggests that Bi replaces some of the Pt sites while does not give a signal. From the aspects of Bi, it is difficult to extract information from the Bi L<sub>3</sub>-edge because of its overlap with Pt L<sub>2</sub>- and Br K-edges. At Bi L<sub>2</sub>-edge, the Pt<sub>92</sub>Bi<sub>8</sub> spectrum shows similar features with Bi powder, with the threshold energy located between that of Bi powder and Bi(III) references (Bi<sub>2</sub>O<sub>3</sub> and Bi(OH)<sub>3</sub>) (**Figure 4-3i**). It indicates that Bi mainly exists in the metallic state, and charge transfer has taken place from less electronegative Bi atoms to Pt atoms, in good

accord with core level observations in XPS. Finally, all the information points to the formation of PtBi surface alloy on the Pt-rich core (**Figure 4-4**). The structural and electronic modification toward the surface Pt sites would have a profound influence on the catalytic performance.

**Table 4-2. Fitting result of EXAFS at Pt L<sub>3</sub>-edge.**

Scattering path	CN <sup>a)</sup>	R (Å) <sup>b)</sup>	$\sigma^2$ ( $10^{-3}$ Å <sup>2</sup> ) <sup>c)</sup>	$\Delta E_0$ (eV) <sup>d)</sup>
Pt foil				
Pt-Pt	12	$2.76 \pm 0.05$	$4.51 \pm 0.1$	$7.34 \pm 0.3$
Pt NPs				
Pt-Pt	$9.36 \pm 0.3$	$2.75 \pm 0.05$	$5.36 \pm 0.2$	$7.32 \pm 0.3$
Pt <sub>92</sub> Bi <sub>8</sub>				
Pt-Pt	$7.71 \pm 0.3$	$2.75 \pm 0.06$	$5.38 \pm 0.2$	$7.23 \pm 0.3$

<sup>a)</sup> CN, coordination number; <sup>b)</sup> R, interatomic distance; <sup>c)</sup>  $\sigma^2$ , Debye-Waller factor; <sup>d)</sup>  $\Delta E_0$ , energy deviation.

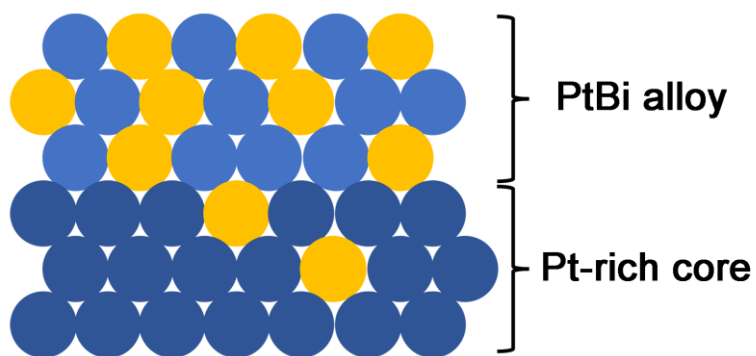


**Figure 4-4. The scheme of the PtBi structural model.**

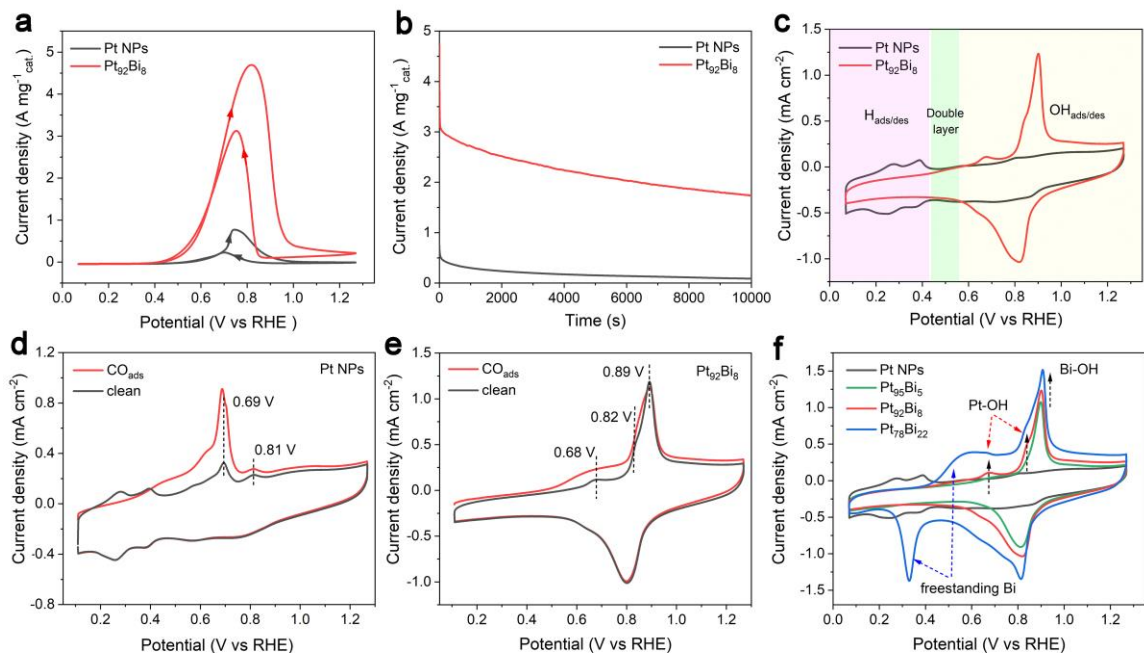


**Figure 4-5.** a) CV curves of Pt NPs and Pt<sub>2</sub>Bi<sub>8</sub> in 1 M KOH / 1 M CH<sub>3</sub>OH at a scan rate of 50 mV s<sup>-1</sup>. b) Long-term durability measurements of Pt NPs and Pt<sub>2</sub>Bi<sub>8</sub> in 1 M KOH / 1 M CH<sub>3</sub>OH at 0.81 V versus RHE. c) CV curves of Pt NPs and Pt<sub>2</sub>Bi<sub>8</sub> in 1 M KOH at a scan rate of 50 mV s<sup>-1</sup>. CO-stripping experiments performed on d) Pt NPs and e) Pt<sub>2</sub>Bi<sub>8</sub> in 1 M KOH at a scan rate of 50 mV s<sup>-1</sup>, respectively. f) CV curves of Pt NPs, Pt<sub>95</sub>Bi<sub>5</sub>, Pt<sub>2</sub>Bi<sub>8</sub>, and Pt<sub>78</sub>Bi<sub>22</sub> in 1 M KOH at a scan rate of 50 mV s<sup>-1</sup>.

1.

### 4.3.3 Electrochemical tests

The catalytic performance was evaluated in a typical three-electrode system in an alkaline solution containing 1 M KOH and 1 M CH<sub>3</sub>OH. **Figure 4-5a** shows that the cyclic voltammograms of Pt NPs and Pt<sub>2</sub>Bi<sub>8</sub> consist of scans toward high potential (the forward scan) and low potential (the backward scan). The peak current density in the forward scan is used to estimate the activity of catalysts. Here, the current density is normalized by the total mass of catalysts rather than the mass of Pt or the specific area, and it is more reasonable considering the cost of additives. Pt<sub>2</sub>Bi<sub>8</sub> shows an activity of 4694 mA mg<sup>-1</sup><sub>cat.</sub>, approximately 6 times that of Pt NPs (771 mA mg<sup>-1</sup><sub>cat.</sub>). The durability is another important criterion for evaluating the performance of catalysts, which is estimated by

chronoamperometry. After a 10000-second durability test, Pt<sub>92</sub>Bi<sub>8</sub> retains a current density of 1738 mA mg<sup>-1</sup><sub>cat.</sub>, 55.9 % of its initial value (3113 mA mg<sup>-1</sup><sub>cat.</sub>) after entering the steady state; however, Pt NPs remain at a current density of 88 mA mg<sup>-1</sup><sub>cat.</sub>, only 16.2 % of its initial value (541 mA mg<sup>-1</sup><sub>cat.</sub>) in the steady state (**Figure 4-5b**). It is clear that Bi plays a significant role in improving the catalytic activity and durability of Pt catalysts.

The question now is how Bi improves the catalytic performance to such a degree. Since the adsorption strength of CO<sub>ads</sub> and OH<sub>ads</sub> have been used as the activity descriptors to predict the methanol oxidation trend, it is reasonable to look into the impact of Bi on the adsorption of CO<sub>ads</sub> and OH<sub>ads</sub>.<sup>31</sup> **Figure 4-5c** shows the different adsorption states of Pt NPs and Pt<sub>92</sub>Bi<sub>8</sub> in 1 M KOH solution at a scan rate of 50 mV s<sup>-1</sup>. Two different regions can be clearly distinguished: hydrogen adsorption/desorption (H<sub>ads/des</sub>) at potentials lower than 0.45 V and the OH adsorption/desorption (OH<sub>ads/des</sub>) region, which occurs at potentials higher than 0.55 V.<sup>32</sup> In the H<sub>ads/des</sub> region, the adsorption of hydrogen is substantially suppressed in the case of Pt<sub>92</sub>Bi<sub>8</sub>, probably arising from the electronic modification on Pt sites or the blocking effect brought by Bi species. In the OH<sub>ads</sub> region, different from Pt NPs, three oxidation peaks appear, which should be attributed to the OH<sub>ads</sub> species adsorbed on the catalyst surface. There is controversy surrounding their assignments to specific sites, but it holds the key to revealing the role of Bi, and this will be discussed in detail in the following section.

CO<sub>ads</sub> is a notorious intermediate blamed for poisoning Pt active sites in methanol oxidation. To evaluate the anti-poisoning capacity, CO-stripping experiments were conducted on the Pt NPs and Pt<sub>92</sub>Bi<sub>8</sub>. On Pt NPs, the charge density associated with the oxidative removal of CO<sub>ads</sub> takes place over the range of 0.4 to approximately 0.9 V (**Figure 4-5d**). The strongly adsorbed CO<sub>ads</sub> can expel the adsorbed impurities from the Pt surface.<sup>33</sup> As a result, OH<sub>ads</sub> at specific Pt sites also contribute to the current density in the forward scan, especially around the potential of 0.69 and 0.81 V. In stark contrast to the massive adsorption of CO<sub>ads</sub> on the Pt NPs, CO<sub>ads</sub> on Pt<sub>92</sub>Bi<sub>8</sub> is dramatically decreased, which demonstrates the significant role of Bi in reducing the CO<sub>ads</sub> (**Figure 4-5e**). Meanwhile, two peaks at 0.68 and 0.84 V are also discerned in the case of Pt<sub>92</sub>Bi<sub>8</sub>,

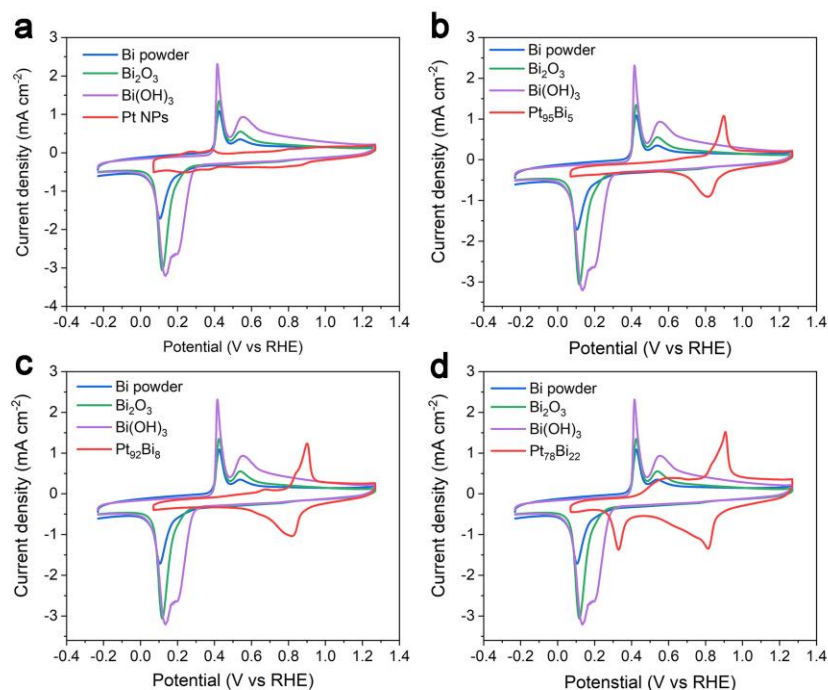


**Figure 4-6. The comparison of cyclic voltammograms of a) Pt NPs, b) Pt<sub>98</sub>Bi<sub>2</sub>, c) Pt<sub>92</sub>Bi<sub>8</sub>, and d) Pt<sub>78</sub>Bi<sub>22</sub> with that of references, including Bi powdering, Bi<sub>2</sub>O<sub>3</sub>, and Bi(OH)<sub>3</sub>. The electrolyte is 1 M KOH.**

and they turn out to be the OH<sub>ads</sub> at Pt sites. However, the assignment of the sharp peak at 0.89 V is controversial. Many studies assign this peak to the formation of Bi(OH)<sub>3</sub>,<sup>34</sup> while others attribute it to OH<sub>ads</sub> at the Pt sites induced by the neighboring Bi.<sup>35</sup>

To identify the nature of this peak, we recorded the cyclic voltammograms of PtBi samples with different Bi contents in 1 M KOH solution (**Figure 4-5f**). The peak intensities of peaks at 0.68 and 0.84 V both get enhanced with increasing Bi content, which means that Bi can strengthen the adsorption of OH<sub>ads</sub> on the Pt sites, given that these two peaks have been proven to be related to OH<sub>ads</sub> at the Pt sites. For the peak at 0.89 V, the growing current density with a higher Bi content indicates its identity as OH<sub>ads</sub> at Bi sites of the PtBi alloy. If it is the Pt sites, we would expect a weaker peak intensity because abundant Bi will dilute the Pt sites on the surface. When the Bi content reaches 22 %, new redox couples with similarities to Bi references (Bi powder, Bi<sub>2</sub>O<sub>3</sub>, and Bi(OH)<sub>3</sub>) appear at relatively lower potentials (**Figure 4-6**), and they should belong

to the freestanding Bi species, in the consistency with the TEM observation (**Figure 4-2b**). It further confirms that the peak at 0.89 V is associated with the alloying Bi rather than freestanding Bi species.

It is easy to understand the richness of  $\text{OH}_{\text{ads}}$  at Bi sites considering Bi's oxyphilic properties. However, to see why  $\text{Pt}_{92}\text{Bi}_8$  is more CO-resistant than Pt NPs, we must consider the thermodynamics and kinetics of the adsorption process. In the acidic electrolyte, CO does considerably adsorb on the PtBi nanoparticles even though with a lower onset oxidation potential (0.41 V versus SCE) than that of Pt/C (0.56 V versus SCE),<sup>17</sup> in other words, Bi can weaken the CO adsorption thermodynamically but not reduce it to a degree like in the alkaline electrolyte. What is more,  $\text{OH}_{\text{ads}}$  on the PtBi nanoparticles becomes much less than in the alkaline electrolyte.<sup>16,17,36</sup> Therefore, beyond helping the oxidative removal of  $\text{CO}_{\text{ads}}$  by a bifunctional effect, the OH species may compete with CO for adsorption at Pt sites in the alkaline solution. This competitive adsorption behavior even overwhelms the effect of thermodynamics on reducing  $\text{CO}_{\text{ads}}$ . In summary, Bi can enrich  $\text{OH}_{\text{ads}}$  on the catalyst surface while reducing  $\text{CO}_{\text{ads}}$  both thermodynamically and kinetically. Predictably, that will impact the reaction path of methanol oxidation in alkali.

#### 4.3.4 In situ FTIR results

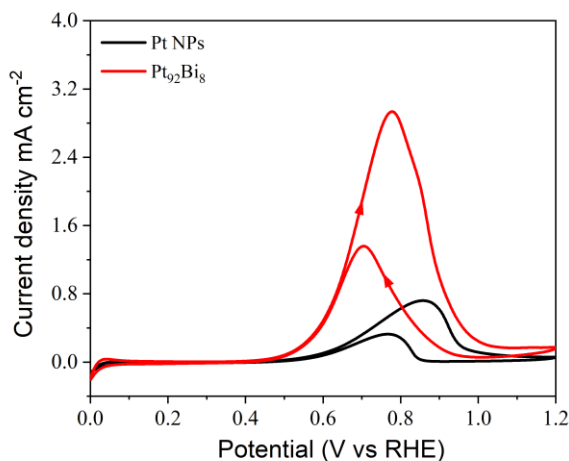


**Figure 4-7. CV curves of Pt NPs and Pt<sub>92</sub>Bi<sub>8</sub> in 0.1 M KOH/1 M CH<sub>3</sub>OH under the ATR-SEIRS mode.**

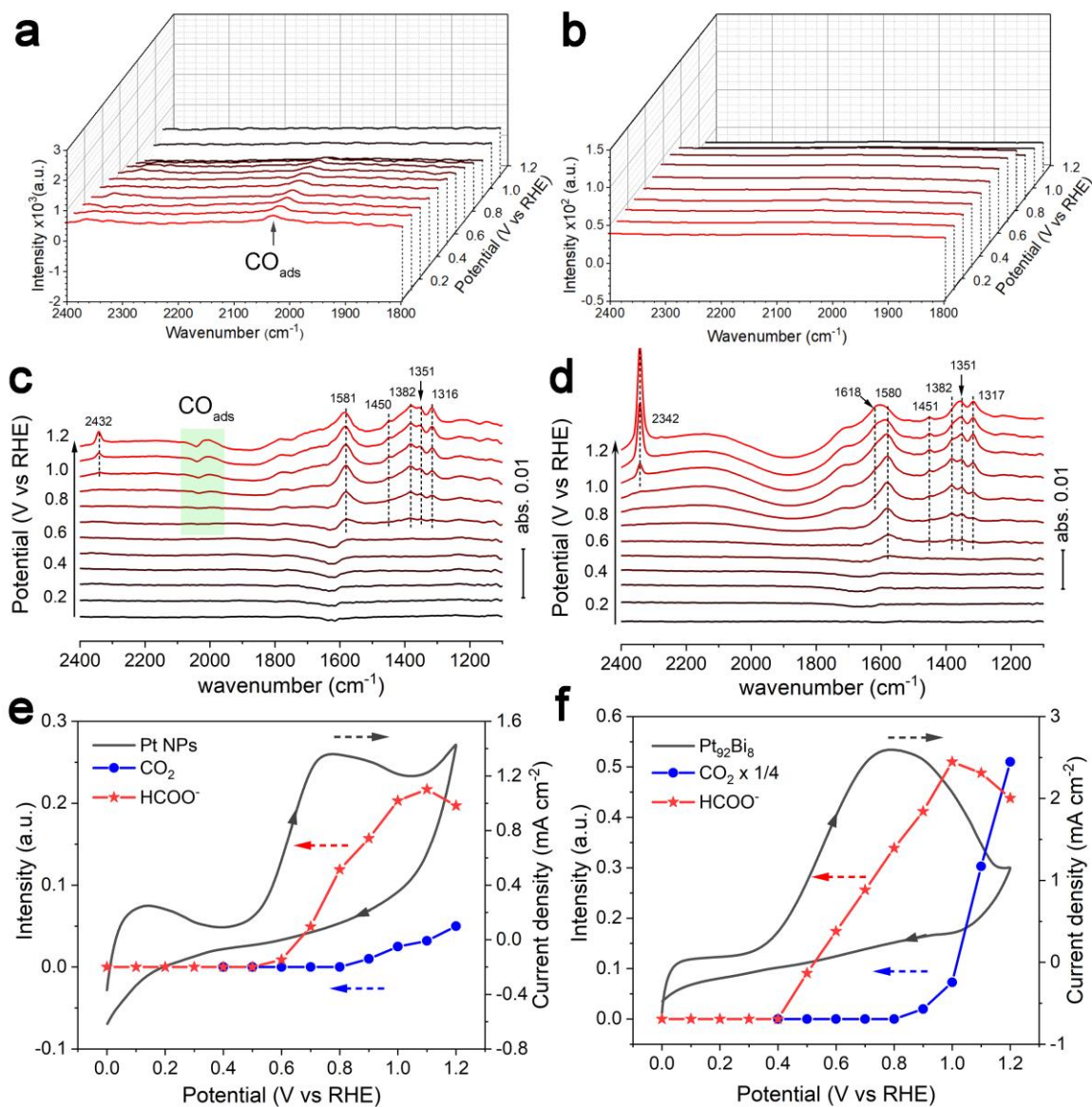


**Figure 4-8. In situ ATR-SEIRAS spectra taken on a) Pt NPs and b) Pt<sub>92</sub>Bi<sub>8</sub> in 0.1 M KOH/ 1 M CH<sub>3</sub>OH over the potential range from 0 to 1.2 V versus RHE. In situ IRAS spectra taken on c) Pt NPs and d) Pt<sub>92</sub>Bi<sub>8</sub> in 0.1 M KOH/ 1 M CH<sub>3</sub>OH over the potential range from 0 to 1.2 V vs. RHE. CV curves (black) and peak intensities at 1581 (blue) and 2432 cm<sup>-1</sup> (red) as a function of applied potential taken on e) Pt NPs and f) Pt<sub>92</sub>Bi<sub>8</sub>, respectively.**

To track the origin of the superb catalytic activity of Pt<sub>92</sub>Bi<sub>8</sub>, in situ attenuated total reflection surface-enhanced infrared absorption spectroscopy (ATR-SEIRAS) and infrared reflection absorption spectroscopy (IRAS) were performed in a 0.1 M KOH electrolyte containing 1 M CH<sub>3</sub>OH. Under the ATR-SEIRAS mode, which is sensitive to the adsorbates on the catalyst surface, cyclic voltammograms show that Pt<sub>92</sub>Bi<sub>8</sub> possesses a much higher current density than Pt NPs (**Figure 4-7**). **Figure 4-8a** shows the ATR-SEIRAS spectra of Pt NPs by applying the potential from 0 to 1.2 V, referenced to the spectra collected at 1.2 V. The IR absorption band at ca. 2034 cm<sup>-1</sup> is assigned to CO<sub>ads</sub> species,<sup>37</sup> confirming that methanol oxidation on Pt NPs does involve the formation of CO<sub>ads</sub>. CO<sub>ads</sub> formed at a low potential is consumed as applying the potential to a high value (**Figures 4-8a**). No adsorption band from CO<sub>ads</sub> is observed in the case of Pt<sub>92</sub>Bi<sub>8</sub> (**Figure 4-8b**), in line with previously reported results.<sup>18,19</sup> As weakly-adsorbed or produced species may dissolve into the solution, IRAS was used to probe the thin layer very close to the working electrode. Again, we see the CO<sub>ads</sub> on the Pt NPs (the unique bipolar peak at ca. 2034 cm<sup>-1</sup> in **Figure 4-8c**) but not on the Pt<sub>92</sub>Bi<sub>8</sub> (**Figure 4-8d**). Referring to the fact that CO barely adsorbs on PtBi catalysts in the alkaline electrolyte (proven by the CO-stripping experiments), the missing of CO<sub>ads</sub> signals in infrared absorption spectra demonstrate that the CO<sub>ads</sub> cannot be a preferable intermediate because a chemical reaction tends to form a stable intermediate other than an unstable one.

Regardless of the CO<sub>ads</sub>, Pt NPs and Pt<sub>92</sub>Bi<sub>8</sub> show similar IR absorption bands in the IRAS spectra (detail assignments listed in **Table 4-3**), of which bands at ca. 1580, 1382, and 1351 cm<sup>-1</sup> are assigned to  $\nu_{as}$  (OCO),  $\delta$  (C-H), and  $\nu_s$  (OCO) of formate (HCOO<sup>-</sup>), respectively.<sup>38,39</sup> The symmetric OCO stretching mode ( $\nu_s$  (OCO)) of bridge-adsorbed formate appears at ca. 1316 cm<sup>-1</sup>.<sup>8,40-42</sup> It indicates that formate is another important intermediate in addition to CO<sub>ads</sub> in the methanol oxidation reaction. The formation of formate is not derived from CO<sub>ads</sub> but requires the presence of active oxygen sources (OH<sub>ads</sub>), which explains why formate can only be observed at relatively high potential (> 0.5 V), the OH<sub>ads/des</sub> region.<sup>8</sup> The bands at 1450 and 2432 cm<sup>-1</sup> are attributed to CO<sub>3</sub><sup>2-</sup>/HCO<sub>3</sub><sup>-</sup> and CO<sub>2</sub>, respectively. The former appears earlier, indicating CO<sub>3</sub><sup>2-</sup>/HCO<sub>3</sub><sup>-</sup> is coming from the desorbed CO<sub>2</sub> into the alkaline solution. **Figures 4-8e and 4-8f** display the intensity of bands at 1581 (HCOO<sup>-</sup>) and 2432 cm<sup>-1</sup> (CO<sub>2</sub>) as a function of the applied



potential during a typical CV in 0.1 M KOH with 1 M CH<sub>3</sub>OH. Formate starts forming as early as 0.4 V on Pt<sub>92</sub>Bi<sub>8</sub> compared to 0.5 V on Pt NPs. Meanwhile, more CO<sub>2</sub> is observed in the case of Pt<sub>92</sub>Bi<sub>8</sub>, which means that methanol is more easily oxidized into formate and further to CO<sub>2</sub> on Pt<sub>92</sub>Bi<sub>8</sub>.

**Table 4-3. Band assignments from the ATR-SEIRAS and IRAS spectra displayed in Figure 4-8.**

Wavenumber / cm <sup>-1</sup>	Assignments
2342	$\nu_{\text{as}}$ (OCO) of CO <sub>2</sub> <sup>43</sup>
1618	$\delta$ (H-O-H) in H <sub>2</sub> O <sup>44</sup>
1580	$\nu_{\text{as}}$ (OCO) in HCOO <sup>-37,38</sup>
1451	$\nu_{\text{as}}$ (OCO) in CO <sub>3</sub> <sup>2-</sup> or HCO <sub>3</sub> <sup>-</sup>
1382	$\delta$ (C-H) in HCOO <sup>-38</sup>
1351	$\nu_{\text{s}}$ (OCO) in HCOO <sup>-38</sup>
1316	$\nu_{\text{s}}$ (OCO) in bridged HCOO <sup>-8</sup>

#### 4.3.5 Reaction pathways

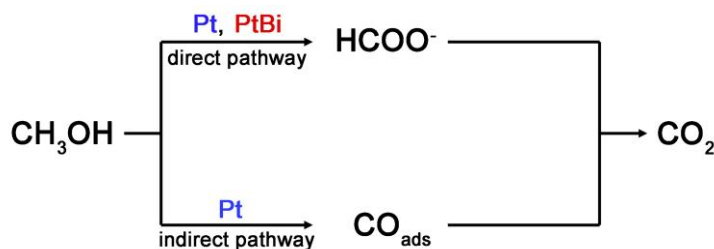


**Figure 4-9. Reaction pathways of methanol oxidation on Pt NPs and PtBi catalysts in the alkaline solution.**

A simplified scheme for the complete electrooxidation of methanol to CO<sub>2</sub> on Pt and PtBi catalysts is proposed (**Figure 4-9**). Methanol oxidation occurring on the Pt NPs involves both the direct and indirect pathways, and CO<sub>ads</sub> generated in the indirect pathway is the main reason for the catalyst deactivation. The advantage of Pt<sub>92</sub>Bi<sub>8</sub> lies in prohibiting the indirect pathway, thereby circumventing the CO-poisoning effect and improving the catalytic performance. Here, the contributions of Bi include, 1) charge transfer from Bi to Pt weakens the CO adsorption at Pt sites thermodynamically; 2) enriching OH<sub>ads</sub> at

Pt sites, which efficiently reduces  $\text{CO}_{\text{ads}}$  by the competitive adsorption of  $\text{OH}_{\text{ads}}$  and  $\text{CO}_{\text{ads}}$  from the aspect of kinetics.

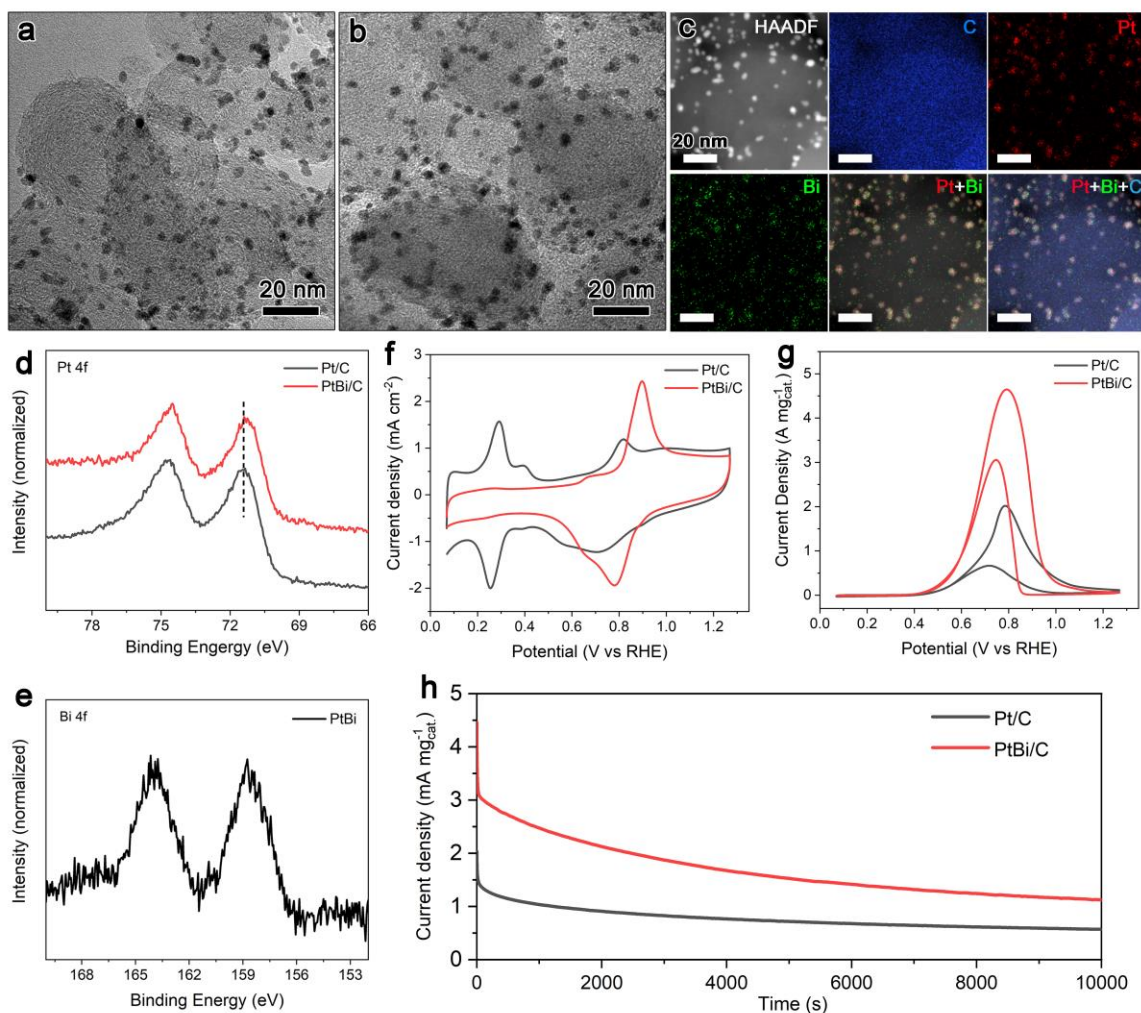


**Figure 4-10.** a) and b) are the TEM images of commercial Pt/C and PtBi/C, respectively. c) Elemental mapping images of PtBi/C. d) and e) are XPS spectra of Pt/C and PtBi/C at Pt and Bi 4f core levels, respectively. f) CV curves of commercial Pt/C and PtBi/C in 1 M KOH at a scan rate of  $50 \text{ mV s}^{-1}$ . g) CV curves of commercial Pt/C and PtBi/C in 1 M KOH/1 M  $\text{CH}_3\text{OH}$  at a scan rate of  $50 \text{ mV s}^{-1}$ . h) Long-term durability measurements of commercial Pt/C and PtBi/C in 1 M KOH /1 M  $\text{CH}_3\text{OH}$  at 0.81 V vs. RHE.

### 4.3.6 Extension of the concept

More importantly, this concept can be generalized to the modification of commercialized catalysts, such as Pt/C. To realize fast and large-scale production, we adopted a microwave-assisted approach with a controllable heating program. In a typical synthesis process, the commercial Pt/C catalyst and Bi precursor were dispersed into the ethylene glycol, and the mixture underwent microwave treatment at 180 °C for 15 min. Given that carbon is a good material for microwave absorption, this approach can create a local high temperature near the carbon support and facilitate the deposition of Bi on Pt particles rather than its self-aggregation in the solvent. **Figures 4-10a** and **4-10b** show the TEM images of commercial Pt/C before and after the modification with Bi. No noticeable change in the particle size is observed, and no aggregation of particles takes place. The elemental mapping images indicate that Bi mainly deposits on the Pt particles (**Figure 4-10c**). The charge redistribution observed at Pt 4f core levels further confirms the strong interaction between Pt and Bi atoms, even though surface Bi is oxidized due to the small particle size and the exposure to air (**Figures 4-10d and 4-10e**). The cyclic voltammogram of PtBi/C in 1 M KOH solution shows similar features with that of the model catalyst, Pt<sub>92</sub>Bi<sub>8</sub>, demonstrating the similarities in their structures (**Figure 4-10f**). As expected, the PtBi/C shows much better activity and durability than the commercial Pt/C catalyst (**Figures 4-10g and 4-10h**). Therefore, this approach possesses great potential for the practical modification of commercial catalysts, especially in the fuel cell field.

## 4.4 Conclusions

In this work, we design a PtBi model catalyst consisting of a PtBi alloy surface and a Pt-rich core. The model catalyst can efficiently suppress the poisoning effect of CO<sub>ads</sub> by directly suppressing the indirect pathway while concurrently enhancing the direct pathway. Combining spectroscopy and electrochemistry analysis, we find that Bi electronically modifies the Pt catalyst by charge redistribution, thus weakening the CO adsorption at Pt sites. More importantly, Bi can generate abundant OH<sub>ads</sub> on the catalyst surface and induce the competitive adsorption of OH<sub>ads</sub> and CO<sub>ads</sub> at Pt sites, which further destabilizes the adsorption of CO<sub>ads</sub>. All these factors contribute to switching the

intermediate from CO<sub>ads</sub> to formate. Free from the CO-poisoning, the Pt<sub>92</sub>Bi<sub>8</sub> shows a much better activity and durability than that of Pt NPs. We have proven the feasibility of this strategy in modifying the commercial Pt/C catalyst from perspectives of both catalytic performance and practical production. This work emphasizes the origin of the CO-tolerance capacity of PtBi catalysts in the alkaline electrolyte and the possibility for successful industrial applications.

## 4.5 References

- (1) Kakati, N.; Maiti, J.; Lee, S. H.; Jee, S. H.; Viswanathan, B.; Yoon, Y. S. Anode catalysts for direct methanol fuel cells in acidic media: Do we have any alternative for Pt or Pt-Ru? *Chemical Reviews* **2014**, *114* (24), 12397.
- (2) Yuda, A.; Ashok, A.; Kumar, A. A comprehensive and critical review on recent progress in anode catalyst for methanol oxidation reaction. *Catalysis Reviews* **2020**, *64* (1), 126.
- (3) Carrette, L.; Friedrich, K. A.; Stimming, U. Fuel cells-fundamentals and applications. *Fuel Cells* **2001**, *1* (1), 5.
- (4) Aricò, A. S.; Srinivasan, S.; Antonucci, V. DMFCs: From fundamental aspects to technology development. *Fuel Cells* **2001**, *1* (2), 133.
- (5) Kaur, A.; Kaur, G.; Singh, P. P.; Kaushal, S. Supported bimetallic nanoparticles as anode catalysts for direct methanol fuel cells: A review. *International Journal of Hydrogen Energy* **2021**, *46* (29), 15820.
- (6) Tong, Y.; Yan, X.; Liang, J.; Dou, S. X. Metal-based electrocatalysts for methanol electro-oxidation: Progress, opportunities, and challenges. *Small* **2021**, *17* (9), e1904126.
- (7) Wasmus, S.; Küver, A. Methanol oxidation and direct methanol fuel cells: A selective review. *Journal of Electroanalytical Chemistry* **1999**, *461* (1), 14.
- (8) Chen, Y. X.; Miki, A.; Ye, S.; Sakai, H.; Osawa, M. Formate, an active intermediate for direct oxidation of methanol on Pt electrode. *Journal of the American Chemical Society* **2003**, *125* (13), 3680.
- (9) Zhong, W.; Liu, Y.; Zhang, D. Theoretical study of methanol oxidation on the PtAu(111) bimetallic surface: CO pathway vs non-CO pathway. *The Journal of Physical Chemistry C* **2012**, *116* (4), 2994.
- (10) Huang, W.; Wang, H.; Zhou, J.; Wang, J.; Duchesne, P. N.; Muir, D.; Zhang, P.; Han, N.; Zhao, F.; Zeng, M.; Zhong, J.; Jin, C.; Li, Y.; Lee, S. T.; Dai, H. Highly

- active and durable methanol oxidation electrocatalyst based on the synergy of platinum-nickel hydroxide-graphene. *Nature Communications* **2015**, *6*, 10035.
- (11) Li, L.; Xing, Y. Pt–Ru nanoparticles supported on carbon nanotubes as methanol fuel cell catalysts. *The Journal of Physical Chemistry C* **2007**, *111* (6), 2803.
- (12) Du, W.; Yang, G.; Wong, E.; Deskins, N. A.; Frenkel, A. I.; Su, D.; Teng, X. Platinum-tin oxide core-shell catalysts for efficient electro-oxidation of ethanol. *Journal of the American Chemical Society* **2014**, *136* (31), 10862.
- (13) Yuan, X.; Jiang, X.; Cao, M.; Chen, L.; Nie, K.; Zhang, Y.; Xu, Y.; Sun, X.; Li, Y.; Zhang, Q. Intermetallic PtBi core/ultrathin Pt shell nanoplates for efficient and stable methanol and ethanol electro-oxidation. *Nano Research* **2018**, *12* (2), 429.
- (14) Dubale, A. A.; Zheng, Y.; Wang, H.; Hubner, R.; Li, Y.; Yang, J.; Zhang, J.; Sethi, N. K.; He, L.; Zheng, Z.; Liu, W. High-performance bismuth-doped nickel aerogel electrocatalyst for the methanol oxidation reaction. *Angewandte Chemie International Edition* **2020**, *59* (33), 13891.
- (15) Yang, M. Catalytic activities of PtBi nanoparticles toward methanol electrooxidation in acid and alkaline media. *Journal of Power Sources* **2013**, *229*, 42.
- (16) Liao, H.; Zhu, J.; Hou, Y. Synthesis and electrocatalytic properties of PtBi nanoplatelets and PdBi nanowires. *Nanoscale* **2014**, *6* (2), 1049.
- (17) Yuan, X.; Jiang, B.; Cao, M.; Zhang, C.; Liu, X.; Zhang, Q.; Lyu, F.; Gu, L.; Zhang, Q. Porous Pt nanoframes decorated with Bi(OH)<sub>3</sub> as highly efficient and stable electrocatalyst for ethanol oxidation reaction. *Nano Research* **2020**, *13* (1), 265.
- (18) Chen, W.; Luo, S.; Sun, M.; Tang, M.; Fan, X.; Cheng, Y.; Wu, X.; Liao, Y.; Huang, B.; Quan, Z. Hexagonal PtBi intermetallic inlaid with sub-monolayer Pb oxyhydroxide boosts methanol oxidation. *Small* **2022**, DOI:10.1002/sml.202107803, e2107803.
- (19) Zhao, F.; Ye, J.; Yuan, Q.; Yang, X.; Zhou, Z. Realizing a CO-free pathway and enhanced durability in highly dispersed Cu-doped PtBi nanoalloys towards methanol full electrooxidation. *Journal of Materials Chemistry A* **2020**, *8* (23), 11564.
- (20) Gasteiger, H. A.; Markovic, N.; Ross Jr, P. N.; Cairns, E. J. Methanol electrooxidation on well-characterized platinum-ruthenium bulk alloys. *The Journal of Physical Chemistry* **1993**, *97* (46), 12020.
- (21) Park, K.-W.; Choi, J.-H.; Kwon, B.-K.; Lee, S.-A.; Sung, Y.-E.; Ha, H.-Y.; Hong, S.-A.; Kim, H.; Wieckowski, A. Chemical and electronic effects of Ni in Pt/Ni

- and Pt/Ru/Ni alloy nanoparticles in methanol electrooxidation. *The Journal of Physical Chemistry B* **2002**, *106* (8), 1869.
- (22) Ouyang, Y.; Cao, H.; Wu, H.; Wu, D.; Wang, F.; Fan, X.; Yuan, W.; He, M.; Zhang, L. Y.; Li, C. M. Tuning Pt-skinned PtAg nanotubes in nanoscales to efficiently modify electronic structure for boosting performance of methanol electrooxidation. *Applied Catalysis B: Environmental* **2020**, *265*, 118606.
- (23) Tsung, C.-K.; Kuhn, J. N.; Huang, W.; Aliaga, C.; Hung, L.-I.; Somorjai, G. A.; Yang, P. Sub-10 nm platinum nanocrystals with size and shape control: Catalytic study for ethylene and pyrrole hydrogenation. *Journal of the American Chemical Society* **2009**, *131* (16), 5816.
- (24) Osawa, M. Dynamic processes in electrochemical reactions studied by surface-enhanced infrared absorption spectroscopy (SEIRAS). *Bulletin of the Chemical Society of Japan* **1997**, *70* (12), 2861.
- (25) Zhu, C.; Lan, B.; Wei, R.-L.; Wang, C.-N.; Yang, Y.-Y. Potential-dependent selectivity of ethanol complete oxidation on Rh electrode in alkaline media: A synergistic study of electrochemical ATR-SEIRAS and IRAS. *ACS Catalysis* **2019**, *9* (5), 4046.
- (26) Li, J.-T.; Zhou, Z.-Y.; Broadwell, I.; Sun, S.-G. In-situ infrared spectroscopic studies of electrochemical energy conversion and storage. *Accounts of Chemical Research* **2012**, *45* (4), 485.
- (27) Wang, C.; Peng, B.; Xie, H.-N.; Zhang, H.-X.; Shi, F.-F.; Cai, W.-B. Facile fabrication of Pt, Pd and Pt-Pd alloy films on Si with tunable infrared internal reflection absorption and synergetic electrocatalysis. *The Journal of Physical Chemistry C* **2009**, *113* (31), 13841.
- (28) Zhang, H.-X.; Wang, S.-H.; Jiang, K.; André, T.; Cai, W.-B. In situ spectroscopic investigation of CO accumulation and poisoning on Pd black surfaces in concentrated HCOOH. *Journal of Power Sources* **2012**, *199*, 165.
- (29) Liu, Y.; Lan, B.; Jia, W.-S.; Yang, Y.-Y. Ethanol selective electrooxidation following the C2 pathway with superior activity and stability at RhBi alloy surface in alkaline media. *Available at SSRN 4097385*.
- (30) Zhu, F.; Tu, K.; Huang, L.; Qu, X.; Zhang, J.; Liao, H.; Zhou, Z.; Jiang, Y.; Sun, S. High selectivity PtRh/RGO catalysts for ethanol electro-oxidation at low potentials: Enhancing the efficiency of CO<sub>2</sub> from alcoholic groups. *Electrochimica Acta* **2018**, *292*, 208.
- (31) Ferrin, P.; Mavrikakis, M. Structure sensitivity of methanol electrooxidation on transition metals. *Journal of the American Chemical Society* **2009**, *131* (40), 14381.

- (32) Rizo, R.; Fernandez-Vidal, J.; Hardwick, L. J.; Attard, G. A.; Vidal-Iglesias, F. J.; Climent, V.; Herrero, E.; Feliu, J. M. Investigating the presence of adsorbed species on Pt steps at low potentials. *Nature Communications* **2022**, *13* (1), 2550.
- (33) Koponen, U.; Peltonen, T.; Bergelin, M.; Mennola, T.; Valkiainen, M.; Kaskimies, J.; Wasberg, M. The impinging jet flow cell — a novel method for the study of PEM fuel cell material. *Journal of Power Sources* **2000**, *86* (1), 261.
- (34) Simões, M.; Baranton, S.; Coutanceau, C. Influence of bismuth on the structure and activity of Pt and Pd nanocatalysts for the direct electrooxidation of NaBH<sub>4</sub>. *Electrochimica Acta* **2010**, *56* (1), 580.
- (35) Schmidt, T. J.; Stamenkovic, V. R.; Lucas, C. A.; Markovic, N. M.; Ross Jr, P. N. Surface processes and electrocatalysis on the Pt(hkl)/Bi-solution interface. *Physical Chemistry Chemical Physics* **2001**, *3* (18), 3879.
- (36) Mahesh, I.; Jaithaliya, R.; Sarkar, A. Efficient electrooxidation of ethanol on Bi@Pt/C nanoparticles: (i) effect of monolayer Bi deposition on specific sites of Pt nanoparticle (ii) calculation of average number of e-s without help of chemical analysis. *Electrochimica Acta* **2017**, 258, 933.
- (37) Wang, J. Y.; Zhang, H. X.; Jiang, K.; Cai, W. B. From HCOOH to CO at Pd electrodes: A surface-enhanced infrared spectroscopy study. *Journal of the American Chemical Society* **2011**, *133* (38), 14876.
- (38) Kowal, A.; Port, S. N.; Nichols, R. J. Nickel hydroxide electrocatalysts for alcohol oxidation reactions: An evaluation by infrared spectroscopy and electrochemical methods. *Catalysis Today* **1997**, *38* (4), 483.
- (39) Li, J.; Wei, R.; Wang, X.; Zuo, Y.; Han, X.; Arbiol, J.; Llorca, J.; Yang, Y.; Cabot, A.; Cui, C. Selective methanol-to-formate electrocatalytic conversion on branched nickel carbide. *Angewandte Chemie International Edition* **2020**, *59* (47), 20826.
- (40) Christensen, P.; Linares-Moya, D. The role of adsorbed formate and oxygen in the oxidation of methanol at a polycrystalline Pt electrode in 0.1 M KOH: An in situ fourier transform infrared study. *The Journal of Physical Chemistry C* **2010**, *114* (2), 1094.
- (41) Chen, Q.-S.; Sun, S.-G.; Zhou, Z.-Y.; Chen, Y.-X.; Deng, S.-B. CoPt nanoparticles and their catalytic properties in electrooxidation of CO and CH<sub>3</sub>OH studied by in situ FTIRS. *Physical Chemistry Chemical Physics* **2008**, *10* (25), 3645.
- (42) Yajima, T.; Uchida, H.; Watanabe, M. In-situ ATR-FTIR spectroscopic study of electro-oxidation of methanol and adsorbed CO at Pt–Ru alloy. *The Journal of Physical Chemistry B* **2004**, *108* (8), 2654.

- (43) Miki, A.; Ye, S.; Osawa, M. Surface-enhanced ir absorption on platinum nanoparticles: An application to real-time monitoring of electrocatalytic reactions. *Chemical Communications (Cambridge)* **2002**, 1500.
- (44) Ataka, K.-i.; Yotsuyanagi, T.; Osawa, M. Potential-dependent reorientation of water molecules at an electrode/electrolyte interface studied by surface-enhanced infrared absorption spectroscopy. *The Journal of Physical Chemistry* **1996**, *100* (25), 10664.



## Chapter 5

# 5 Unveiling the Local Structure and Electronic Properties of PdBi Surface Alloy for Selective Hydrogenation of Propyne

## 5.1 Introduction

Olefins produced by steam cracking inevitably contain a few percent of alkynes and dienes, which are detrimental to the downstream polymerization and thus must be removed.<sup>1-3</sup> Thus, selective hydrogenation of unsaturated hydrocarbons has a significant role in the petrochemical and fine chemical industry.<sup>4-6</sup> Pd is the most used catalyst to selectively hydrogenate alkynes to alkenes due to its efficiency in activating hydrogen molecules.<sup>7,8</sup> However, it is still facing the challenge of over-hydrogenation to alkanes, a thermodynamically favorable reaction, especially in the front-end process with a high concentration of hydrogen.<sup>9,10</sup> To improve selectivity toward desired alkenes, substantial effort has been focused on Pd catalyst modification, including passivating with additives (such as CO and Pb/CaCO<sub>3</sub>),<sup>11-13</sup> creating intermetallic structures,<sup>14-17</sup> and producing a strong metal-support interaction (SMSI) effect.<sup>18-20</sup>

Beyond that, modifying Pd catalysts with a surface alloy structure provides another way to address the selectivity issue, while remaining high activity.<sup>10,21,22</sup> More specifically, a second metal inserts into the parent metal surface by forming a thin alloy layer, which results in a unique surface structure and variegates the behavior of catalysts in reaction.<sup>23-25</sup> From the structural perspective, the surface alloy strategy is capable of preserving the initial facets of the parent substrate, which is of significance to facet-sensitive reactions.<sup>26</sup> From the functional perspective, due to different electronegativity, the insertion of a second metal can efficiently tune the surface electronic properties, directly modulating the adsorption strength of intermediates and enhancing selectivity toward targeted products.<sup>27</sup> For example, grafting Bi terminated by Bi<sub>2</sub>O<sub>3</sub> on the Pd surface results in the electrons transferring from Bi to Pd atoms, which can weaken the ethylene adsorption without comprising the hydrogen activation.<sup>28</sup> Meanwhile, incorporating Au atoms into the surface of Pd nanocrystals induces electrons to transfer from Pd to Au atoms, which

can also weaken the adsorption of alkene.<sup>21</sup> The debate indicates the difficulty of building a reliable relationship between the electronic structure and catalytic performance because of the entanglement from other factors, such as size, facets, local morphology, etc. Therefore, it is necessary and vital to find a “clean” surface and deepen the understanding of the electronic properties for building a reliable relationship between the electronic structure and catalytic performance.

In this work, we contrive a PdBi surface alloy structure model by changing the deposition rate of Bi relative to the atomic interdiffusion rate at the interface. Combining X-ray diffraction (XRD), X-ray photoelectron spectroscopy (XPS), and X-ray absorption spectroscopy (XAS), a precise and comprehensive understanding of its local structure and electronic properties is provided. The electronic structure of Pd can be continuously tuned by varying the Bi content in the PdBi alloy, underlying the optimization of catalytic performance. The selective hydrogenation of propyne is used as a representative reaction, in which the PdBi model catalysts show superior selectivity over the pure Pd counterpart catalyst, originating from preventing the formation of saturated  $\beta$ -hydrides in the subsurface layers and weakened propene adsorption on the surface. This work provides a precise and comprehensive understanding of the electronic properties of the PdBi surface alloy structure, offering guidance for analyzing electronic structure in a bimetallic system.

## 5.2 Experimental section

### 5.2.1 Chemicals

Sodium tetrachloropalladate (II) ( $\text{Na}_2\text{PdCl}_4$ ), bismuth neodecanoate ( $\text{Bi}(\text{NE})_3$ ), polyvinylpyrrolidone (PVP,  $\text{MW} = 55000 \text{ g}\cdot\text{mol}^{-1}$ ), diethylamine, and L-ascorbic acid were purchased from Sigma-Aldrich. Diethylene glycol was purchased from Alfa Aesar. Ethanol, acetone, potassium bromide, and potassium chloride were bought from Sinopharm Chemical Reagent Co., Ltd. All reagents were used as received without further purification.

### 5.2.2 Synthesis of Pd cubes

Pd cubes with a diameter of around 16 nm were prepared through a previously reported method.<sup>29</sup> In a typical synthesis process, 105 mg PVP, 60 mg L-ascorbic acid, 185 mg potassium chloride, and 600 mg potassium bromide were added into 8 mL deionized water in a 20 mL vial and pre-heated to 85 °C under stirring in a water bath. And then, 3 mL  $\text{Na}_2\text{PdCl}_4$  (64 mM) solution was quickly injected into the vial. The vial was then capped and heated at 85 °C for 3 hours. The resulting product was collected with centrifugation (10000 rpm) and washed with acetone and water (acetone: water = 2 mL: 8 mL).

### 5.2.3 Synthesis of PdBi nanoparticles with a surface alloy structure

The as-prepared Pd cubes and 222 mg PVP were added into 17 mL diethylene glycol. The mixture was degassed at 60 °C for 30 min to remove low boiling point solvent and dissolved oxygen, and then switched to  $\text{N}_2$  atmosphere and heated to 180 °C. A certain amount of  $\text{Bi}(\text{NE})_3$  dissolved in 3 mL DEG was quickly injected into the solution. The solution was kept at 180 °C for 15 min. The resulting product was collected by centrifugation and washed with ethanol ten times. The amount of  $\text{Bi}(\text{NE})_3$  are 2.83 mg, 7.30 mg, and 15.4 mg for  $\text{Pd}_{98.8}\text{Bi}_{1.2}$ ,  $\text{Pd}_{96.9}\text{Bi}_{3.1}$ , and  $\text{Pd}_{94.2}\text{Bi}_{5.8}$ , respectively. For the synthesis of PdBi/ $\text{Al}_2\text{O}_3$  catalysts, the as-prepared PdBi nanoparticles were supported on  $\gamma\text{-Al}_2\text{O}_3$  using a wet impregnation method, and the loading amount of Pd was fixed to 5 wt.%.

### 5.2.4 Synthesis of PdBi nanoparticles with a surface island structure

The synthesis procedure of PdBi surface islands is the same as that of PdBi surface alloy except for replacing  $\text{Bi}(\text{NE})_3$  with bismuth acetate (0.01mmol).

### 5.2.5 Characterization

Transmission electron microscopy (TEM) images were collected on a FEI TECNAI G2 operated at 200 kV. The elemental mapping and high-angle angular dark field (HAADF)

images were recorded with a TECNAI G2 F20 electron microscope equipped with energy dispersive spectroscopy (EDS). Empyrean diffractometer operated at 40 kV, and 30 mA with Cu K $\alpha$  as a light source was used to collect the X-ray diffraction (XRD) patterns. X-ray photoelectron spectroscopy (XPS) was performed on a Kratos AXIS Untraded ultrahigh vacuum (UHV) surface analysis system with an Al K $\alpha$  light source. Inductively coupled plasma-optical emission spectrometry (ICP-OES, Avio 200) was used to determine the elemental composition. XAFS spectra at Pd K-edge and Bi L<sub>3</sub>-edge were collected using a fluorescence yield (FY) mode at the 20 BM beamline of the Advanced Photon Source (APS) operated by Argonne National Laboratory, United States. XANES spectra at Pd L<sub>3</sub>-edge were collected using a total electron yield (TEY) mode at the SXRMB beamline of Canadian Light Source (CLS), Canada. H<sub>2</sub>-temperature-programmed desorption (H<sub>2</sub>-TPD) was measured by an automatic chemical adsorption instrument (FINETEC/FINE-SORB-3010). In detail, 10 mg PdBi/Al<sub>2</sub>O<sub>3</sub> catalyst was added into a U-shape tube reactor. The sample was first flushed with Ar at a gas flow rate of 40 mL/min for 10 min at room temperature to remove the physically adsorbed gas impurities and then exposed to the H<sub>2</sub> atmosphere (80 mL/min) for 20 min. Following, Ar was used to flush away the physically adsorbed H<sub>2</sub> for 10 min. The reactor was then heated to 700 °C with a heating rate of 10 °C/min in the Ar flow (40 mL/min). The desorbed H<sub>2</sub> was detected by a thermal conductivity detector (TCD), with the working temperature and current being equal to 60 °C and 90 mA, respectively.

### 5.2.6 Catalytic evaluation of supported Pd and PdBi catalysts.

The catalytic properties were performed in a fixed quartz reactor with an inner diameter of 8 mm. 5 mg of supported catalyst on  $\gamma$ -Al<sub>2</sub>O<sub>3</sub> was physically mixed with 200 mg quartz sand (powder size: 60–80 mesh) fixed in the middle of the reactor. The reaction temperature was raised in a 15/44 mL/min H<sub>2</sub>/N<sub>2</sub> flow from room temperature to the targeted condition, followed by the C<sub>3</sub>H<sub>4</sub> introduction to initiate the propyne semi-hydrogenation. All the gas flow rates were controlled by three mass flow controllers. The outlet products were quantitatively analyzed by two online gas chromatographs (GCs). Specifically, the hydrocarbon products were detected by a flame ionization detector (FID) using a capillary column of TM-Al<sub>2</sub>O<sub>3</sub>/S, while the H<sub>2</sub> and N<sub>2</sub> were measured by a

thermal conductivity detector (TCD) through a packed column of TDX-01. The  $C_3H_4$  conversion,  $C_3H_6/C_3H_8$  selectivity, and  $C_3H_6$  space-time yield (STY) were calculated by the following equations:

$$C_3H_4 \text{ conversion (\%)} = \frac{n(C_3H_4)_{in} - n(C_3H_4)_{out}}{n(C_3H_4)_{in}} \times 100\% \quad (5.1)$$

$$C_3H_6 \text{ selectivity (\%)} = \frac{n(C_3H_6)_{out}}{n(C_3H_4)_{in} - n(C_3H_4)_{out}} \times 100\% \quad (5.2)$$

$$C_3H_8 \text{ selectivity (\%)} = \frac{n(C_3H_8)_{out}}{n(C_3H_4)_{in} - n(C_3H_4)_{out}} \times 100\% \quad (5.3)$$

$$C_3H_6 \text{ STY} = \frac{m(C_3H_6)_{out}}{m(\text{catalyst}) \times t} \quad (5.4)$$

### 5.2.7 XPS spectrum fitting

CasaXPS was used to fit XPS spectra at Pd 3d orbitals, in which a Shirley background and Gaussian-Lorentzian line shape modified with an exponential function (GL(m)T( $\alpha$ )) were used, where m indicates the portion of Lorentzian in the Gaussian-Lorentzian function, while  $\alpha$  is the asymmetric parameter. To compare the asymmetric parameter, m was fixed to 60. The fitting window was between 333 to 345 eV.

### 5.2.8 XAFS data analysis

Athena software was used to do the energy calibration and background subtraction. The XAFS spectra were calibrated referring to the standard metal foil. EXAFS spectra in k space were obtained by subtracting an arctangent background. The EXAFS spectra in R space were obtained by Fourier transform of the  $\chi(k)$  with a  $k^3$  weighting, and the k range was set to 3 to 12.9  $\text{\AA}^{-1}$ . Artemis software was used to fit the EXAFS spectra in R space. Amplitude was set to 0.7 based on the fitting result of Pd foil. To compare the coordination number reasonably, we fixed the Debye-Waller factors of Bi-O and Bi-Pd scattering paths to 4.00 and 7.80, respectively.

## 5.2.9 DFT simulations

The ab initio quantum mechanical (QM) calculations were performed using Vienna Ab initio Simulation Package (VASP) at a version of 5.4.4 with the projector augmented wave (PAW) method and a plane wave basis set. The method is density functional theory (DFT) with generalized gradient approximations (GGA) of Perdew-Burke-Ernzerhof (PBE) functional. A dispersion correction, the DFT-D3 method with Becke-Jonson damping, was included in the calculations. The energy cut-off was set to 400 eV. Here, the binding energy of adsorbates was simulated. For the pure Pd model, we used the experimental lattice parameter 3.85 Å to construct a 4×4×4 Pd (100) surface slab with the bottom two layers fixed and the top two layers relaxed. For PdBi (100) model, it was sampled by replacing one surface Pd atom in 4×4×4 Pd (100) with one Bi atom to represent the experimental PdBi alloy. The vacuum layers were set up at least 15 Å to minimize possible interactions between the replicated cells. The extended lattice change was neglected due to the very small doping ratio.

## 5.3 Results and discussion

### 5.3.1 Growth mechanism

To modulate the electronic structure of Pd by inserting a second metal, one issue that should be considered is whether it is miscible with Pd, which is determined by thermodynamics. Typically, the seed-based epitaxial growth follows the layer-by-layer growth mode (Frank-van der Merwe) or island-like growth mode (Volmer-Weber).<sup>30</sup> This process has been described as the chemical potential of the system (Eq. 5.5),<sup>30,31</sup>

$$\mu(n) = \mu_{3D}^0 + [E_{aa} - E_{ab}(n)] \quad (5.5)$$

where  $\mu_{3D}^0$  is the bulk chemical potential of the core material and  $E_{aa}$  and  $E_{ab}$  are the interatomic energies per atom describing the adhesion strength of the newly formed atoms on the same crystal (a) and the metallic seed (b), respectively. In a specific system,  $\mu_{3D}^0$  and  $E_{aa}$  are constant, while  $E_{ab}$  is determined by the adhesion strength between a and b and the strain energy, both of which are related to the number of atomic layers ( $n$ ) of a. In the first few layers of the heterogeneous epitaxial growth, it is driven by a higher

chemical potential ( $\mu_{soln}$ ) of the atoms of a in solution than  $\mu(n)$  of the nanoparticle, following the layer-by-layer growth mode (FM) with a coherent lattice structure. However, the weak interaction and a large lattice mismatch between a and b result in the rise in  $\mu(n)$ , and it quickly reaches a critical value ( $\mu_c$ ) where the layer-by-layer growth stops. Following this, the lattice dislocation may take place to reduce the interface energy. Then the growth will switch to the VW mode to form islands on the crystal surface.<sup>32</sup> Previous reports have proven that Bi and Pd can form intermetallic structures,<sup>33,34</sup> therefore, inserting Bi atoms into Pd lattice to tune the electronic structure of Pd is feasible from the perspective of thermodynamics.

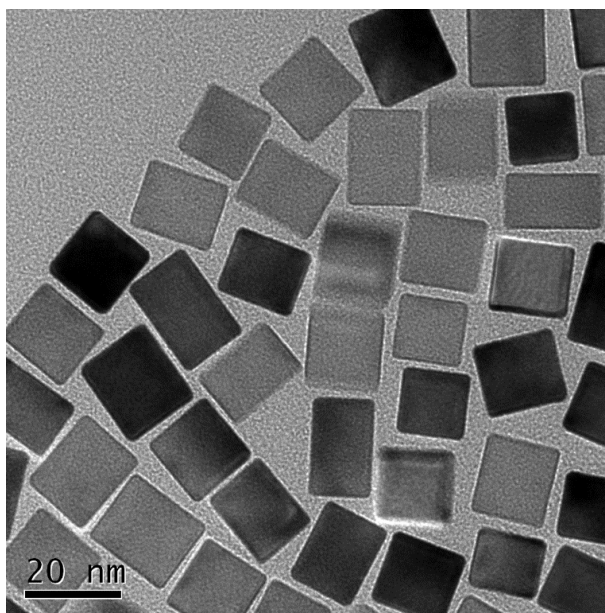


**Figure 5-1. TEM image of Pd cubes.**

### 5.3.2 Morphology and composition studies

Experimentally, Pd cubes with a diameter of  $\sim 16$  nm were firstly synthesized according to a previously reported method (**Figure 5-1**),<sup>29,35</sup> and used as the substrate for the deposition of Bi. The introduction of Bi precursors used a hot-injection method to guarantee a good structural uniformity, in which the as-prepared Pd cubes, diethylene glycol, and polyvinylpyrrolidone (PVP) were used as a substrate, reductant, and surfactant, respectively. Even though the insertion of Bi atoms into the Pd lattice is supported by thermodynamics, it is also a kinetically controlled process. Predictably, the

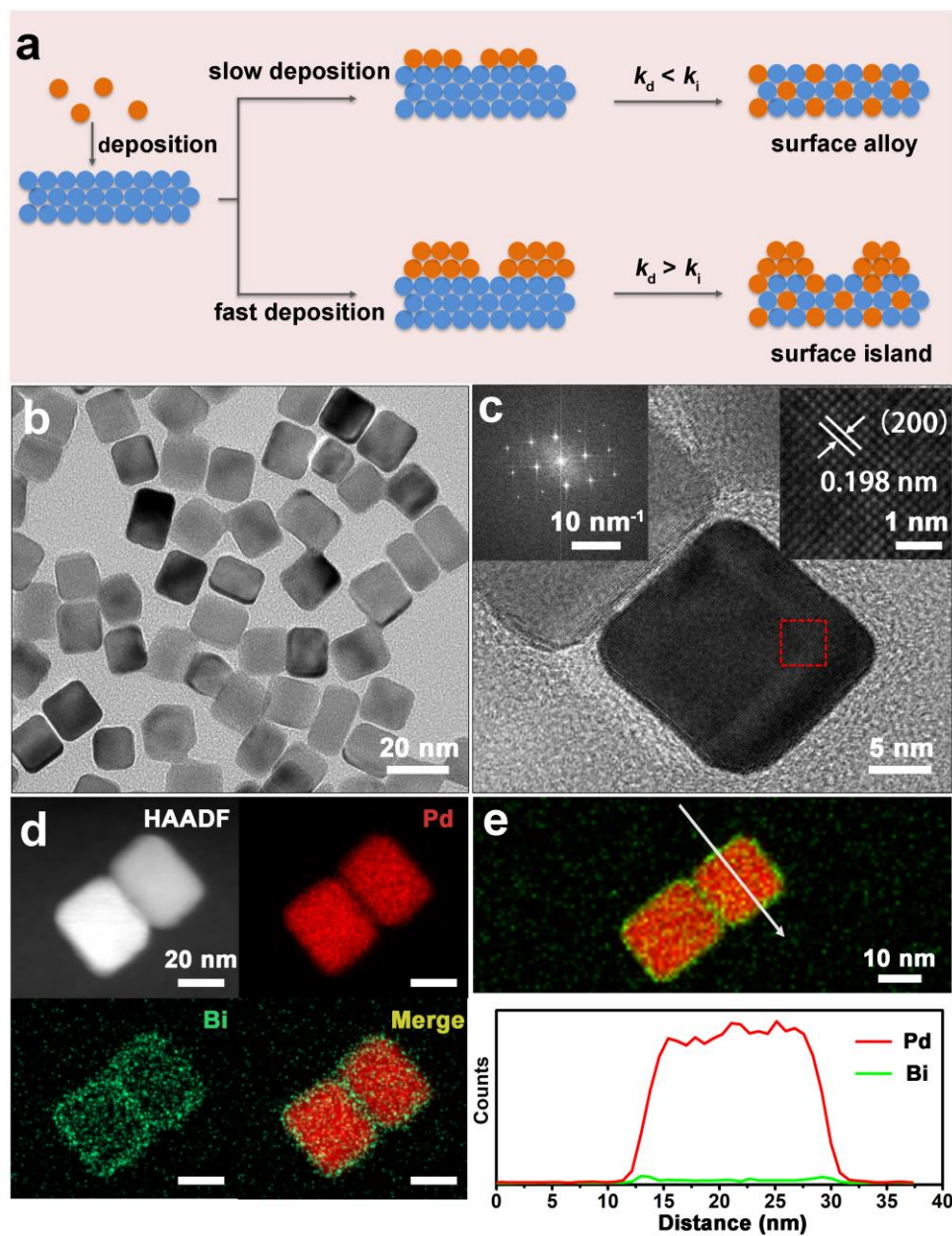


**Figure 5-2.** a) The schematic illustration of epitaxial growth modes. b) and c) are the TEM and HRTEM images of Pd<sub>96.9</sub>Bi<sub>3.1</sub>, respectively. Insets in c) are the fast Fourier transform (top left) and zoom-in image (top right) of the selected area (red dash square), respectively. d) and e) indicate the elemental mapping images and line scanning analysis of Pd<sub>96.9</sub>Bi<sub>3.1</sub>, respectively.

epitaxial growth mode is determined by the deposition rate ( $k_d$ ) and atomic interdiffusion rate ( $k_i$ ), which usually occurs in the high-temperature synthesis of bimetallic catalysts.



As schematically illustrated in **Figure 5-2a**, when the atomic interdiffusion rate at the interface is faster than the deposition rate (i.e.,  $k_d < k_i$ ), the foreign atoms will diffuse into the lattice of parent substrate to form a surface alloy structure. The alloying effect will relax the strain caused by the lattice mismatch and keep the present growth mode. On the contrary, an over-fast deposition rate will quickly saturate the substrate surface (i.e.,  $k_d > k_i$ ), which leads to the formation of islands on an alloyed surface. The reaction temperature was set constant at 180 °C to fix the interdiffusion rate, and the entangled experimental parameters were simplified to control the Bi deposition rate. Given that different ligands endow metal precursors with variable stability, that makes it possible to tune the deposition rate by changing precursor ligands.<sup>36</sup> To get a slow deposition rate of Bi, bismuth neodecanoate, a Bi precursor coordinated with three 8-carbon-length tails, was introduced into the system.

Herein, Pd<sub>96.9</sub>Bi<sub>3.1</sub> was taken as an example to study the surface structure, in which the subscripts indicate the molar ratio of corresponding elements determined by inductively coupled plasma-optical emission spectroscopy (ICP-OES). As shown in **Figure 5-2b**, the average diameter of particles is about 16 nm, similar to that of the initial Pd seeds. However, rounded vertexes and edges are observed, and some of the particles are connected at vertex sites, verifying the existence of the interdiffusion phenomenon. The high-resolution transmission electron microscopy (HRTEM) image shows that the lattice spacing is 0.198 nm, close to that of the (200) facet of fcc-phase Pd. The fast Fourier transform of the selected area in **Figure 5-2c** indicates its single crystalline nature and further confirms its fcc-phase structure. The energy-dispersive X-ray spectroscopy (EDS) shows that Pd dominates in the core while Bi exclusively deposits on the whole particle surface (**Figure 5-2d**). The two bumps appearing on both sides of the line scanning profile suggest a core-shell structure consisting of a Pd core and a PdBi bimetallic shell (**Figure 5-2e**). However, when bismuth acetate was used as the precursor, which possesses a fast deposition rate under the same reaction condition, Bi species coalesced on the Pd surface to form islands (**Figure 5-3**).

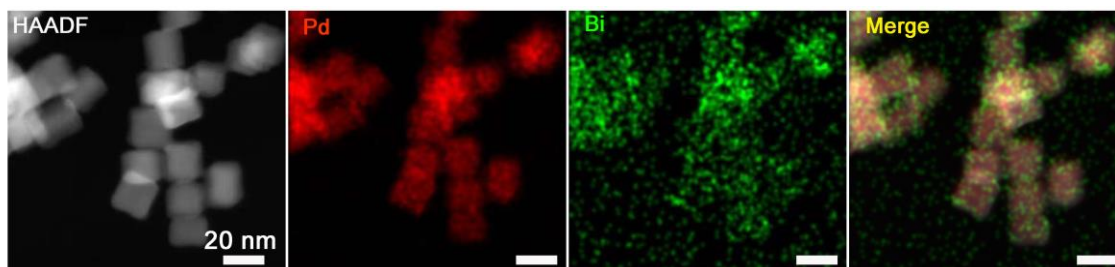


**Figure 5-3. Elemental mapping images of PdBi nanoparticles with bismuth acetate used as the precursor.**

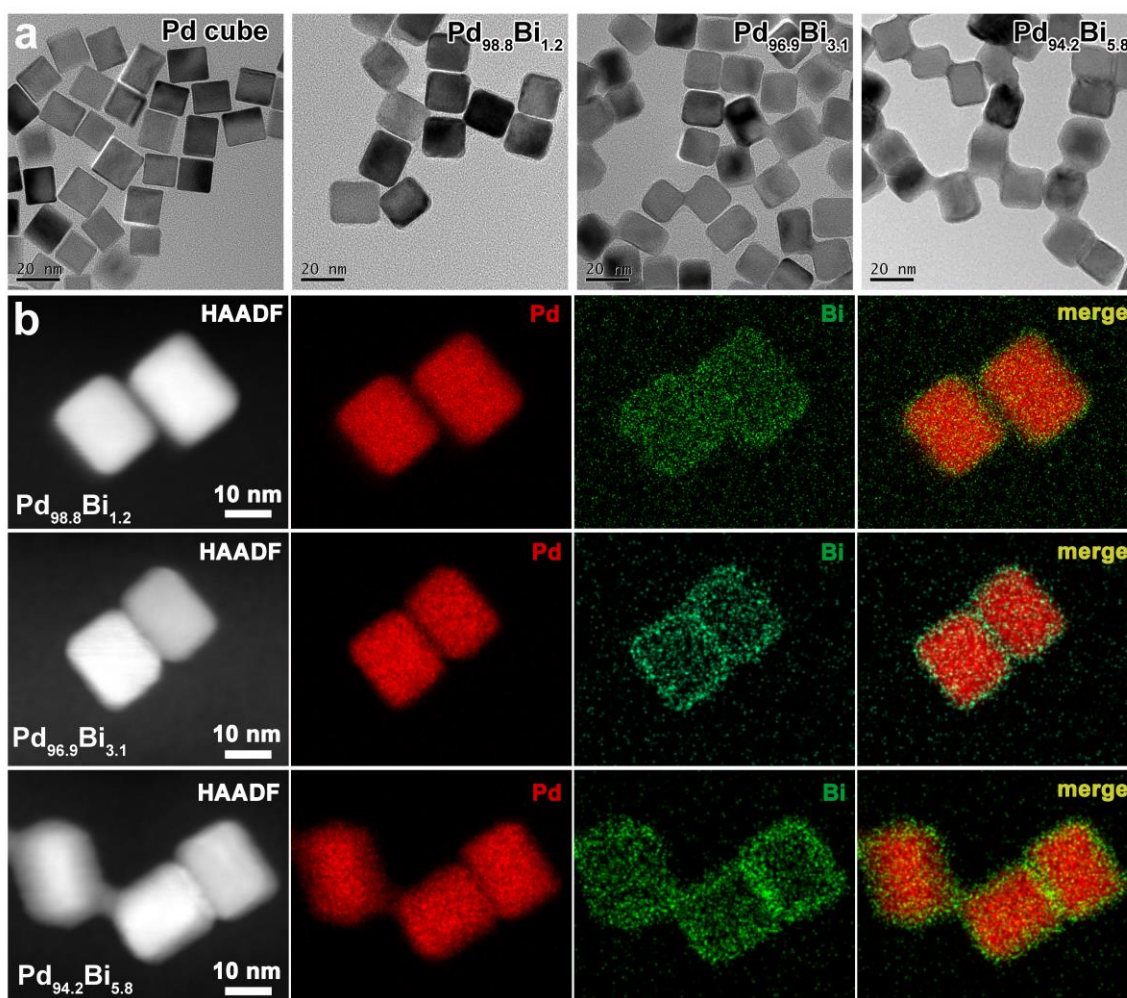


**Figure 5-4. a) TEM images of Pd cube, Pd<sub>98.8</sub>Bi<sub>1.2</sub>, Pd<sub>96.9</sub>Bi<sub>3.1</sub>, and Pd<sub>94.2</sub>Bi<sub>5.8</sub>. b) Elemental mapping images of Pd<sub>98.8</sub>Bi<sub>1.2</sub>, Pd<sub>96.9</sub>Bi<sub>3.1</sub>, and Pd<sub>94.2</sub>Bi<sub>5.8</sub>.**

### 5.3.3 Crystalline structure study

To verify the formation of PdBi surface alloy structure, a series of PdBi samples with different Pd/Bi ratios have been prepared by adjusting the feeding ratio of Pd and Bi precursors. All the samples exhibit a similar particle size of ~16 nm, with Bi species located on the surface of Pd cubes (**Figures 5-4**). X-ray diffraction characterization was firstly used to investigate the crystalline structure of PdBi samples. As shown in the **Figure 5-5a**, all PdBi samples possess a fcc crystalline phase like that of Pd cubes, and the diffraction peaks around  $2\theta = 40.1^\circ$ ,  $46.7^\circ$ ,  $68.2^\circ$ ,  $82.1^\circ$ , and  $86.8^\circ$  are assigned to the (111), (200), (220), (311), and (222) facets, respectively. However, the diffraction peaks shift to the lower diffraction angle for PdBi samples compared to that of Pd cubes. Taking the (111) facet as an example, the diffraction peak shifts to  $40.10^\circ$ ,  $40.08^\circ$ , and  $40.02^\circ$  when the Bi content increases to 1.2 %, 3.1 %, and 5.8 %, respectively. The peak shift indicates that Bi atoms diffuse into the Pd lattice and expand the lattice parameters as the Bi atom has a larger atomic size than that of the Pd atom, suggesting the formation of a surface alloy structure.

### 5.3.4 Electronic structure study

As a powerful surface-sensitive characterization technique, X-ray photoelectron spectroscopy was performed to probe the surface chemistry of PdBi samples. **Figure 5-5b** shows that the metallic Pd  $3d_{5/2}$  core levels of PdBi samples (334.50, 334.40, and 334.36 eV for Pd<sub>98.8</sub>Bi<sub>1.2</sub>, Pd<sub>96.9</sub>Bi<sub>3.1</sub>, and Pd<sub>94.2</sub>Bi<sub>5.8</sub>, respectively) shift to the lower binding energy compared to that of Pd cubes (334.56 eV), and a higher Bi content induces a more obvious shift, which indicates a charge redistribution between Pd and Bi atoms, and an electron-rich state is reached at Pd sites. Four sets of peaks in **Figure 5-5c** are ascribed to the  $4f_{5/2}$  and  $4f_{7/2}$  core levels of metallic bismuth and bismuth oxide species. With an oxophilic property, Bi metal is prone to be oxidized upon exposure to the air, and that explains the bismuth oxides dominate in the XPS spectra, and only a weak signal of metallic Bi can be detected in the case of Bi powder. When Bi is incorporated into the Pd system, the metallic Bi  $4f_{7/2}$  core levels (156.60, 156.54, and 156.46 eV for Pd<sub>98.8</sub>Bi<sub>1.2</sub>, Pd<sub>96.9</sub>Bi<sub>3.1</sub>, and Pd<sub>94.2</sub>Bi<sub>5.8</sub>, respectively) shift to the higher

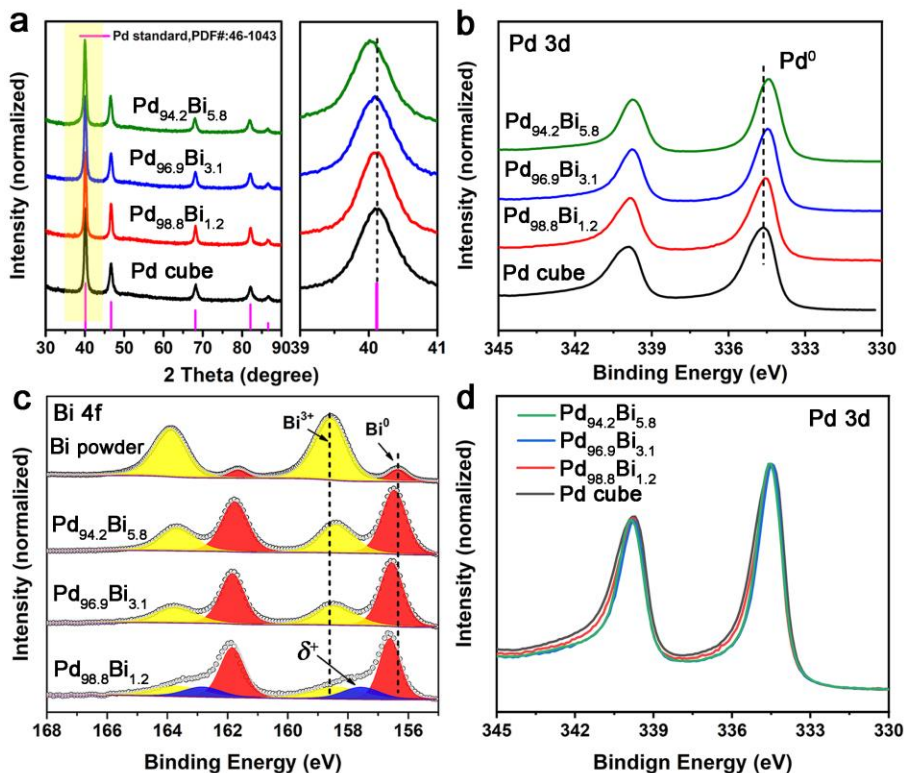


**Figure 5-5. a) XRD patterns (left) of PdBi samples and the zoom-in image of the selected yellow region from  $2\theta = 39^\circ$  to  $41^\circ$  (right). b) and c) are XPS spectra of PdBi samples at Pd 3d and Bi 4f core levels, respectively. d) Comparison of line shapes of Pd 3d peaks after aligning peaks together and ignoring the binding energy shift**

binding energy compared to that of Bi powder (156.35 eV), demonstrating electron transfer from Bi to Pd atoms. This trend is consistent with the information from the aspect of Pd 3d core level shift. Noticeably, different from the domination of oxides in the case of Bi powder, the majority of Bi species exist in a metallic state for the PdBi samples, verifying the strong interaction between Bi and Pd atoms. Besides, when the Bi content decreases, the shifting trend toward the higher binding energy becomes more obvious, which can be easily understood that Bi atoms have more Pd atoms surrounded in this situation.

Another characteristic of the formation of a PdBi alloy is shown in the change of symmetry of Pd 3d peaks. For monometallic Pd, the asymmetric line shape of Pd 3d peaks stems from the many-body effect, which is linked to the presence of narrow

unoccupied 4d states at the Fermi level. It has been proven that upon alloying, the charge redistribution due to the hybridization of valence orbitals changes the valence band structure of Pd, which may bring new features into spectroscopic properties.<sup>37</sup> To compare the symmetry of Pd 3d peaks, we align all peaks together for convenience, and the binding energy shift is not taken into consideration in this situation. As shown in **Figure 5-5d**, the skew many-body line shape (known as the Doniach-Sunjic line shape) of Pd 3d peaks in the Pd cube becomes more symmetric in the PdBi samples.<sup>38</sup> To quantitatively analyze the asymmetric parameters, CasaXPS was used to fit Pd 3d peaks in which a Shirley background and Gaussian-Lorentzian line shape modified with an exponential function (GL(m)T( $\alpha$ )) were used (see details in Supporting Information), where m indicates the portion of Lorentzian in the Gaussian-Lorentzian function, while  $\alpha$  is the asymmetric parameter (a larger  $\alpha$  has a more symmetric feature). The fitting results are shown in **Table 5-1**, respectively. The asymmetric parameter,  $\alpha$ , changes to 1.05, 1.18, and 1.62 for Pd<sub>98.8</sub>Bi<sub>1.2</sub>, Pd<sub>96.9</sub>Bi<sub>3.1</sub>, and Pd<sub>94.2</sub>Bi<sub>5.8</sub>, respectively, compared to 0.98 of the Pd cube, which means that the line shape of Pd 3d peaks becomes more symmetric with increasing Bi content. This observation indicates that the Pd gains d charge upon surface alloying, in good accord with XPS core level observation. Here, we did not consider the line shape of Bi 4f peaks because of the interference of the oxide components. Meanwhile, there are no narrow unoccupied densities of the d state above the Fermi level, and asymmetric peak shape is also not expected. Combining the binding energy shift and the changes in the symmetry of the Pd 3d line shape, the XPS results provide solid evidence for the formation of a PdBi surface alloy.

**Table 5-1. XPS fitting results of Pd cube and PdBi samples.**

Sample	Pd 3d <sub>3/2</sub> (eV)	Pd 3d <sub>5/2</sub> (eV)	$\alpha$ <sup>[a]</sup>
Pd cube	339.85	334.56	0.98
Pd <sub>98.8</sub> Bi <sub>1.2</sub>	339.79	334.50	1.05
Pd <sub>96.9</sub> Bi <sub>3.1</sub>	339.69	334.40	1.18
Pd <sub>94.2</sub> Bi <sub>5.8</sub>	339.65	334.36	1.62

[a] Asymmetric parameters.

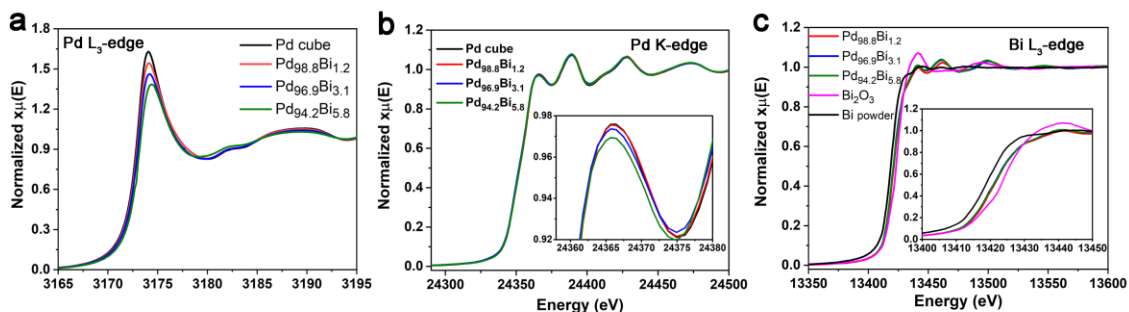


**Figure 5-6. XANES spectra of PdBi samples at a) Pd L<sub>3</sub>-edge, b) Pd K-edge, and c) Bi L<sub>3</sub>-edge.**

In order to obtain a deeper understanding of its electronic states as well as the local structure, X-ray absorption fine structure, including X-ray absorption near edge structure (XANES) and extended X-ray absorption fine structure (EXAFS), were collected at both the Pd L<sub>3</sub>-edge and Bi L<sub>3</sub>-edge. **Figure 5-6a** shows the XANES spectra recorded in surface-sensitive total electron yield (TEY) at the Pd L<sub>3</sub>-edge in which the sharp peak at the edge jump is known as a whitenline, and it arises from the transition from the Pd 2p<sub>3/2</sub> to the narrow unoccupied states just above the Fermi level with 4d<sub>5/2,3/2</sub> character (dipole transition). The intensity of the whitenline decreases upon alloying compared to the Pd cube. The weakened whitenline intensity indicates charge transfer to the Pd 4d state has taken occurred in the alloys (reduction in 4d hole count just above the Fermi level). In other words, Pd gains d charge from the less electronegative Bi. This observation is entirely consistent with the binding energy shift and the asymmetry of the Pd 3d peaks.

### 5.3.5 Local structure study

To probe the local structural information, we also collected the XANES and EXAFS spectra at Pd K-edge (**Figure 5-6b**). However, little change can be found in both the XANES and EXAFS. This is because compared to the Pd L<sub>3</sub>-edge, which is in the soft X-ray region, the X-ray penetrates the shallow region; more important, with TEY detection, only the surface alloy contributes. At the K-edge, however, the X-ray samples the entire core (transmission and fluorescence yield mode). Hence, the Pd atoms in the core dominate the signal. At the Bi L<sub>3</sub>-edge, the absorption threshold, related to the transition

from  $2p_{3/2}$  to  $6s$  character at the Fermi level of PdBi samples, locates between that of Bi powder and  $\text{Bi}_2\text{O}_3$ , indicating a different electronic state from that of Bi powder of Bi (0) and  $\text{Bi}_2\text{O}_3$  of Bi (III) oxidation state (the inset in **Figure 5-6c**). In the EXAFS region, new emerging oscillations in the spectra suggest a change in the local environment which will be discussed in detail in the following section. To extract the local structure information, an arctangent background was subtracted from the EXAFS spectra, and a sinusoidal oscillation arising from the interference of outgoing and backscattering electron waves was obtained, in which the amplitude is element-specific while the  $k_{\text{max}}$  separation (the distance between two neighboring peaks, indicated by dash lines in the **Figure 5-7a**) is associated with the interatomic distance. It is found that the Bi EXAFS spectra in  $k$  space show a similarity with that of Pd cube, but much different from that of Bi powder and  $\text{Bi}_2\text{O}_3$ , which means Bi atoms in PdBi alloys adopt the Pd fcc structure. In other words, Bi atoms diffuse into the Pd surface lattice, forming a layer of PdBi alloy without changing the fcc crystal structure of Pd. The similarity in the Pd K edge and Bi  $L_3$ -edge EXAFS arises from the fact that Bi is in a Pd environment with only Pd nearest neighbors. Another finding is that the oscillations are compressed along the  $k$  range when increasing the Bi content, i.e., shifting toward a lower  $k$ , which indicates the Bi-scatterer interatomic distances are lengthened.

To better interpret the spectra, the  $\chi(k)$  with  $k^3$  weighting was Fourier transformed into  $R$  space, where the peak position is associated with the radial distance between the absorber and surrounding atoms (with a phase correction term), and the magnitude is proportional to the coordination number of surrounding atoms (**Figure 5-7b**). From the perspective of the Bi  $L_3$ -edge, different from scattering paths in Bi powder and  $\text{Bi}_2\text{O}_3$ , new peaks emerge around 2.5 Å (the blue zone in **Figure 5-7b**) and 5.0 Å (the yellow zone in the **Figure 5-7b**) for the PdBi samples. These new features have a good similarity with that of the Pd cube. Therefore, we would propose that peaks at 2.5 and 5.0 Å should be assigned to the Bi-Pd scattering paths in the first shell and the third shell, respectively.

To substantiate this assumption, wavelet transform (WT), a parallel mathematic transform with Fourier transform, was conducted on the EXAFS spectra, and its advantage lies in bringing a third dimension, i.e., energy, into the system to help identify



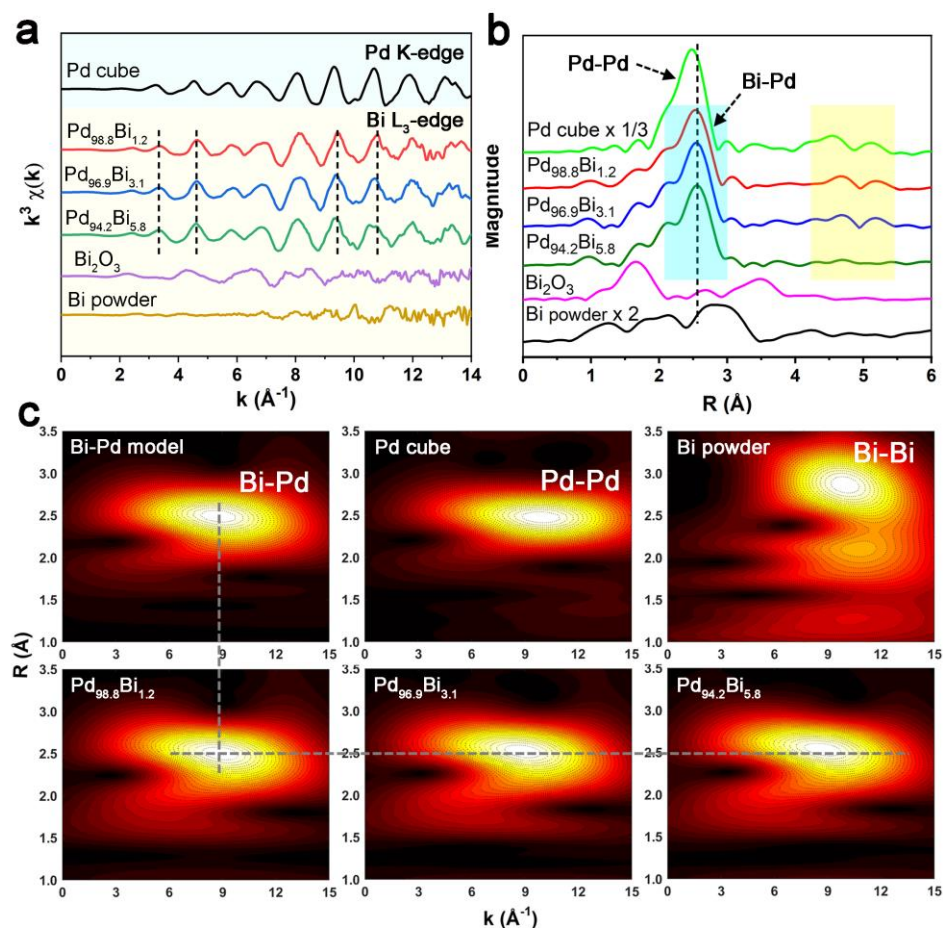


**Figure 5-7.** a) and b) are the EXAFS spectra of PdBi samples and references in  $k$  and  $R$  space, respectively. A  $k^3$  weighting is used in the Fourier transform. c) The WT contour plots of the Bi-Pd model, Pd cube, Bi powder, and PdBi samples. A  $k^3$  weighting is used.

the atomic species of the scatterer.<sup>39</sup> **Figure 5-7c** shows WT contour plots of PdBi samples as well as references. Taking  $\text{Pd}_{98.8}\text{Bi}_{1.2}$  as an example, the intensity maximum appears at  $k = 8.92 \text{ \AA}^{-1}$ ,  $R = 2.5 \text{ \AA}$ , very close to  $k = 8.75 \text{ \AA}^{-1}$ ,  $R = 2.5 \text{ \AA}$  of Bi-Pd scattering model, but different from that of Pd-Pd and Bi-Bi scattering paths (appear at  $k = 9.95 \text{ \AA}^{-1}$ ,  $R = 2.5 \text{ \AA}$  and  $k = 10 \text{ \AA}^{-1}$ ,  $R = 2.85 \text{ \AA}$ , respectively). Therefore, it should be assigned to the Bi-Pd scattering path. And for all PdBi samples, the intensity maxima locate at the same  $k$  position (**Figures 5-8**), which provides another solid evidence for the formation of a PdBi surface alloy. The compressed oscillation in the  $k$  space also has a



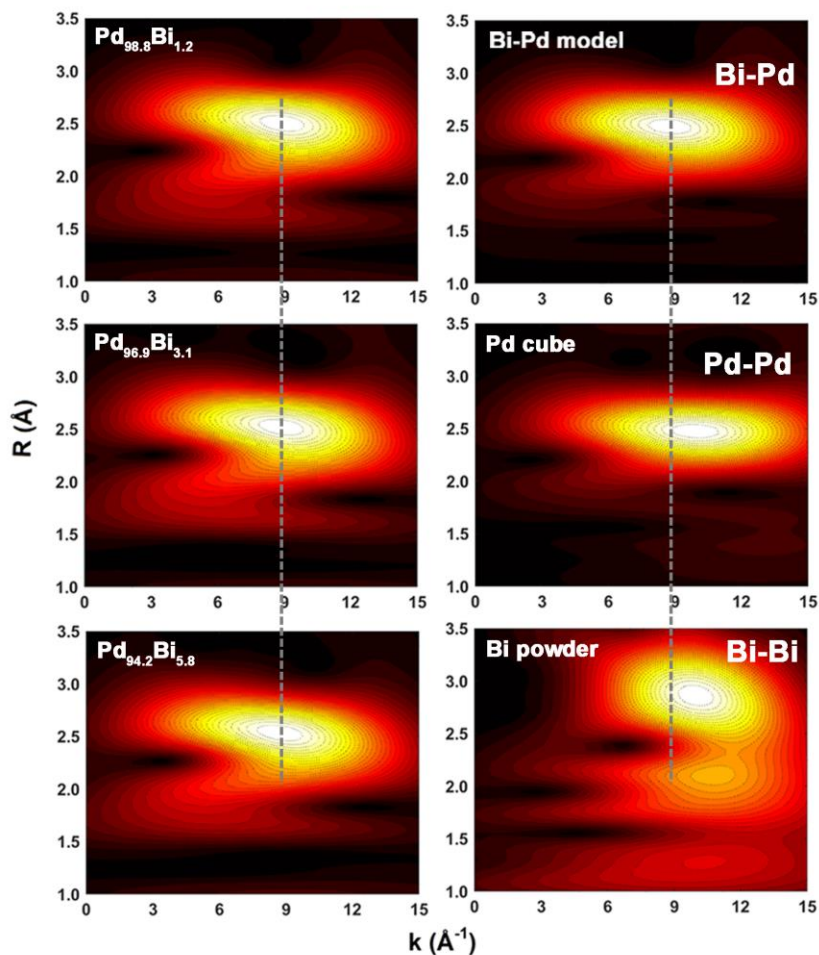


**Figure 5-8. WT contour plots of PdBi samples and references.**

reflection in the R space and WT contour as the peak or intensity maximum shifts to a high R when increasing Bi content. This shifting trend indicates an expanded lattice parameter after the insertion of Bi atoms, keeping in line with XRD data.

To quantitatively analyze the local structure of PdBi surface alloy, we fitted the EXAFS spectra in R space, and the fitting results are shown in **Table 5-2**. All samples have a similar Pd coordination number of around 12, and it is easy to understand that Pd in the core contributes to the majority of the signal at the Pd K-edge. From the perspective of Bi that provides the information on the surface alloy layer, it only contains two scattering paths, Bi-O and Bi-Pd. The O coordination number is less than one, which should be assigned to the trace amount of O sitting on surface Bi sites due to its oxophilicity. This is

consistent with the XPS observation of a small Bi oxide peak. Pd has a coordination number of four to five, much less than completely coordinated Pd (CN = 12) in the fcc phase, indicating that Bi atoms are mostly situated in the surface and subsurface layers, significantly reducing the coordination number. The radial distances between Bi and Pd are 2.72, 2.73, and 2.74 Å for Pd<sub>98.8</sub>Bi<sub>1.2</sub>, Pd<sub>96.9</sub>Bi<sub>3.1</sub>, and Pd<sub>94.2</sub>Bi<sub>5.8</sub>, respectively, demonstrating that Bi atoms diffuse into Pd lattices and expand lattice parameters. Finally, all the information points to the formation of a PdBi surface alloy with pure Pd in the core. The introduction of Bi leads to electron-rich Pd sites due to the hybridization of valence orbitals, and it expands the lattice parameters but keeps its original fcc phase structure. These unique characteristics will have a profound influence on its catalytic properties.

**Table 5-2. EXAFS fitting results in R space at Pd K-edge and Bi L<sub>3</sub>-edge.**

Scattering Paths	CN <sup>[a]</sup>	R (Å) <sup>[b]</sup>	$\sigma^2$ (10 <sup>-3</sup> Å <sup>2</sup> ) <sup>[c]</sup>	$\Delta E_0$ (eV) <sup>[d]</sup>
<b>Pd cube</b>				
Pd-Pd	12	2.74 ± 0.05	5.68 ± 0.3	1.33 ± 0.3
<b>Pd<sub>98.8</sub>Bi<sub>1.2</sub></b>				
Pd-Pd	12.18 ± 0.5	2.74 ± 0.07	5.71 ± 0.2	1.33 ± 0.2
Bi-O	0.86 ± 0.4	2.17 ± 0.01	4.09 ± 5	6.43 ± 0.6
Bi-Pd	4.39 ± 0.2	2.72 ± 0.07	7.80 (fixed)	6.43 ± 0.6
<b>Pd<sub>96.9</sub>Bi<sub>3.1</sub></b>				
Pd-Pd	11.57 ± 0.5	2.74 ± 0.06	5.66 ± 0.2	1.18 ± 0.3
Bi-O	0.76 ± 0.2	2.17 ± 0.01	4.00 ± 1	6.27 ± 0.6
Bi-Pd	4.93 ± 0.4	2.73 ± 0.06	7.80 ± 0.6	6.27 ± 0.6
<b>Pd<sub>94.2</sub>Bi<sub>5.8</sub></b>				
Pd-Pd	12.33 ± 0.4	2.74 ± 0.05	5.96 ± 0.2	1.02 ± 0.2
Bi-O	0.78 ± 0.1	2.17 ± 0.01	4.00 (fixed)	6.12 ± 0.6
Bi-Pd	4.91 ± 0.2	2.74 ± 0.05	7.80 (fixed)	6.12 ± 0.6

[a] Coordination number. [b] Interatomic distance. [c] Debye-Waller factor. [d] Energy deviation.

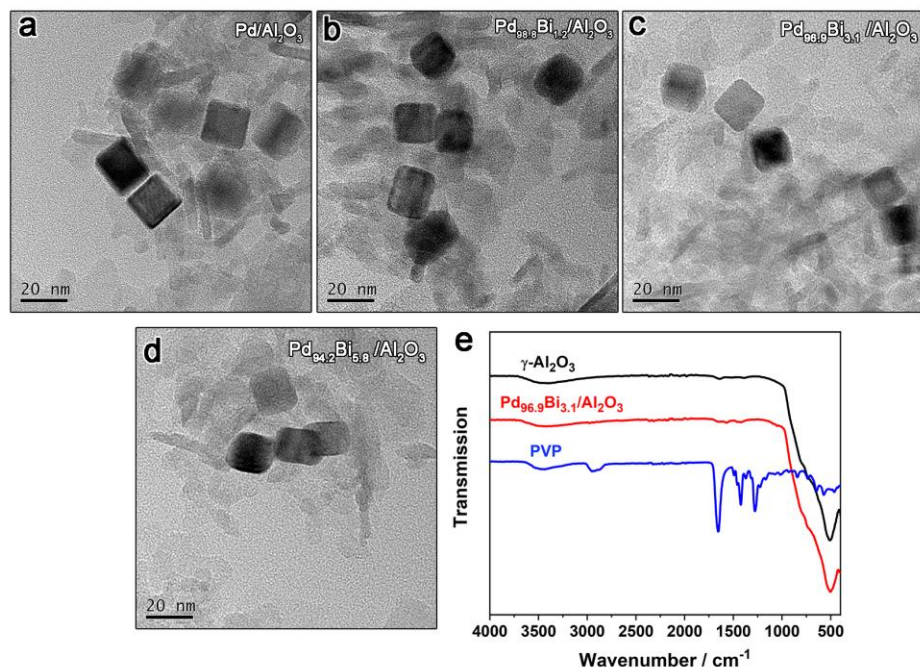


**Figure 5-9.** TEM images of a) Pd/Al<sub>2</sub>O<sub>3</sub>, b) Pd<sub>98.8</sub>Bi<sub>1.2</sub>/Al<sub>2</sub>O<sub>3</sub>, c) Pd<sub>96.9</sub>Bi<sub>3.1</sub>/Al<sub>2</sub>O<sub>3</sub>, and d) Pd<sub>94.2</sub>Bi<sub>5.8</sub>/Al<sub>2</sub>O<sub>3</sub>, respectively. e) The FTIR spectra of PVP,  $\gamma$ -Al<sub>2</sub>O<sub>3</sub>, and Pd<sub>96.9</sub>Bi<sub>3.1</sub>/Al<sub>2</sub>O<sub>3</sub>.

### 5.3.6 Selective hydrogenation of propyne

The catalytic properties of the as-prepared PdBi catalysts were evaluated in the selective hydrogenation of propyne. The as-prepared PdBi nanoparticles were firstly subjected to washing to circumvent the influence of PVP and then supported on the  $\gamma$ -Al<sub>2</sub>O<sub>3</sub> substrate (**Figure 5-9a-d**). The Fourier-transform infrared (FTIR) spectra show that no residual PVP was found on the surface to block the active sites (**Figure 5-9e**). The catalytic performance test of the PdBi catalysts was conducted in a fixed bed reactor with an inner diameter of 8 mm. As shown in **Figure 5-10a** that the introduction of Bi can efficiently enhance the selectivity toward propene. The propene selectivity has an upgoing trend with the Bi content increasing, from 67.8 % for Pd/Al<sub>2</sub>O<sub>3</sub> to 87.4, 93.3, and 98.7% for Pd<sub>98.8</sub>Bi<sub>1.2</sub>/Al<sub>2</sub>O<sub>3</sub>, Pd<sub>96.9</sub>Bi<sub>3.1</sub>/Al<sub>2</sub>O<sub>3</sub>, and Pd<sub>94.2</sub>Bi<sub>5.8</sub>/Al<sub>2</sub>O<sub>3</sub>, respectively. The propyne conversion is nearly 100 % for samples with a low Bi content ( $\leq 3.1$  %). However, it drops to 36.6 % when the Bi content reaches 5.8 %. The conversion drop is supposed to result from the dilution effect as the higher Bi content will decrease the portion of Pd

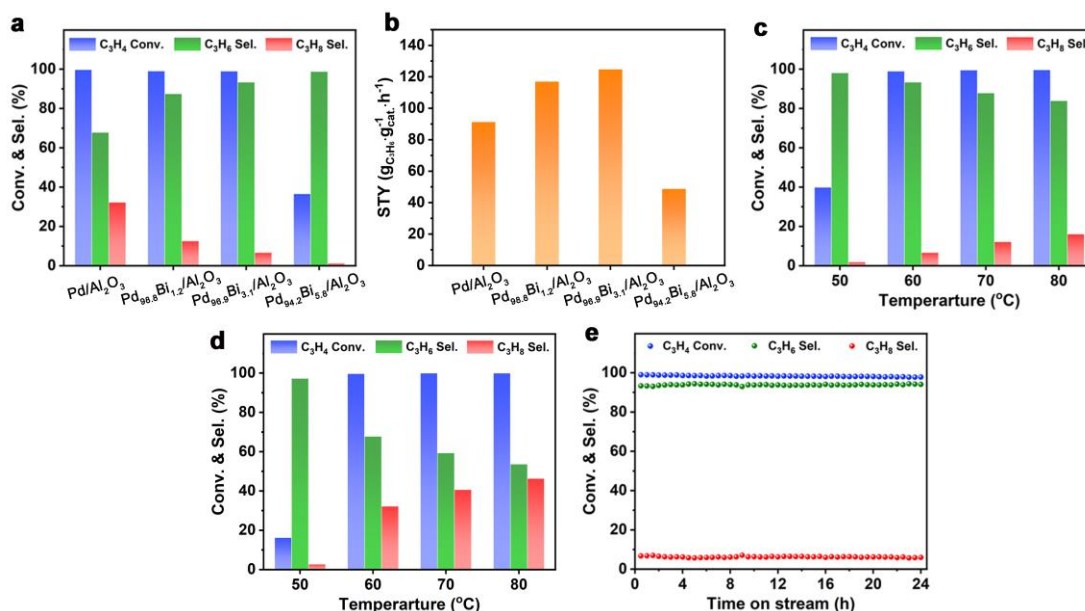


**Figure 5-10.** Catalytic performance of selective hydrogenation of propyne on various PdBi catalysts. a) The histogram of propyne conversion, propene, and propane selectivity over different PdBi samples. b) The histogram of propene STY over different PdBi samples. c) and d) The histogram of propyne conversion, propene and propane selectivity at different temperatures on Pt<sub>96.9</sub>Bi<sub>3.1</sub>/Al<sub>2</sub>O<sub>3</sub> and Pd cube/Al<sub>2</sub>O<sub>3</sub>, respectively. e) Stability test of Pt<sub>96.9</sub>Bi<sub>3.1</sub>/Al<sub>2</sub>O<sub>3</sub> over 24 hours on stream. Reaction conditions: C<sub>3</sub>H<sub>6</sub>/H<sub>2</sub>/N<sub>2</sub> = 6/15/44 mL/min, T = 60 °C except when investigating the influence of reaction temperature, P = 0.1 MPa and catalyst weight = 5 mg.

atoms on the surface while Pd is the active site for this reaction. Given that propyne conversion and propene selectivity have an opposite trend when changing the Bi content, the space-time yield (STY) of propene was used to evaluate their catalytic performance (**Figure 5-10b**). It is found that increasing Bi content results in a volcano shape of the propene STY. Pd<sub>96.9</sub>Bi<sub>3.1</sub>/Al<sub>2</sub>O<sub>3</sub> shows the highest propene STY of 124.9 g<sub>C<sub>3</sub>H<sub>6</sub></sub>·g<sub>cat.</sub><sup>-1</sup>·h<sup>-1</sup> compared to 91.4, 117.1, and 48.9 g<sub>C<sub>3</sub>H<sub>6</sub></sub>·g<sub>cat.</sub><sup>-1</sup>·h<sup>-1</sup> for Pd/Al<sub>2</sub>O<sub>3</sub>, Pd<sub>98.8</sub>Bi<sub>1.2</sub>/Al<sub>2</sub>O<sub>3</sub>, and Pd<sub>94.2</sub>Bi<sub>5.8</sub>/Al<sub>2</sub>O<sub>3</sub>, respectively.

The degree of alkynes hydrogenation is also thermodynamically oriented.

Macroscopically, it is sensitive to the reaction temperature. To investigate the influence

of surface alloying on the resistance toward over-hydrogenation, Pd<sub>96.9</sub>Bi<sub>3.1</sub>/Al<sub>2</sub>O<sub>3</sub> was evaluated in the hydrogenation of propyne at different temperatures, and Pd/Al<sub>2</sub>O<sub>3</sub> was used for comparison (**Figures 5-10c and 5-10d**). As the temperature increases from 50 to 80 °C, the propene selectivity of Pd<sub>96.9</sub>Bi<sub>3.1</sub>/Al<sub>2</sub>O<sub>3</sub> exhibits a slight decrease from 98.1 to 84 %, while a dramatic drop from 97.2 to 53.7 % takes place in the case of Pd/Al<sub>2</sub>O<sub>3</sub>, demonstrating the significant role of Bi in suppressing over-hydrogenation. In addition to the conversion and selectivity, the stability of catalysts is another important criterion for choosing an efficient catalyst. Herein, the best catalyst, Pd<sub>96.9</sub>Bi<sub>3.1</sub>/Al<sub>2</sub>O<sub>3</sub>, was subjected to a 24-hour stability test on stream (**Figure 5-10e**). It is apparent from Figure 5-4 that there is no noticeable drop in both propyne conversion and propene selectivity as they are nearly constant at 98.3 % and 93.8 %, respectively, and the selectivity of over-hydrogenation product, propane, keeps at a low value of around 6.2 %, which verifies its good stability. Therefore, PdBi catalysts with a unique and tunable surface alloy structure can be used as an active, selective, and stable catalyst for selective hydrogenation of propyne.

### 5.3.7 Simulation results

In order to study further the impact of Bi insertion on the catalytic properties, density functional theory (DFT) simulations were conducted based on two structure models, i.e., the Pd (100) and PdBi (100) surfaces (see more details in the Supporting Information). As reported previously, the dissociative adsorption of hydrogen is closely related to the activity of catalysts in the hydrogenation reaction.<sup>40,41</sup> As shown in **Figure 5-11a**, on PdBi (100) the adsorption of hydrogen is slightly enhanced with the binding energy decreasing from -0.443 (on Pd) to -0.490 eV (on PdBi), which indicates that the introduction of Bi can strengthen the adsorption of surface hydrogen on Pd. The strengthened hydrogen adsorption is of help to increase the surface coverage of hydrogen to facilitate the following hydrogenation reaction steps. However, hydrogen atoms not only adsorb on surface sites but also dissolve into the subsurface.<sup>42,43</sup> Indeed, those bulk dissolved hydrogen species are more energetic and can hydrogenate surface adsorbates upon migrating to the surface, blamed for the over-hydrogenation.<sup>44</sup> To monitor the hydrogen adsorption behavior, hydrogen temperature-programed desorption (H<sub>2</sub>-TPD)

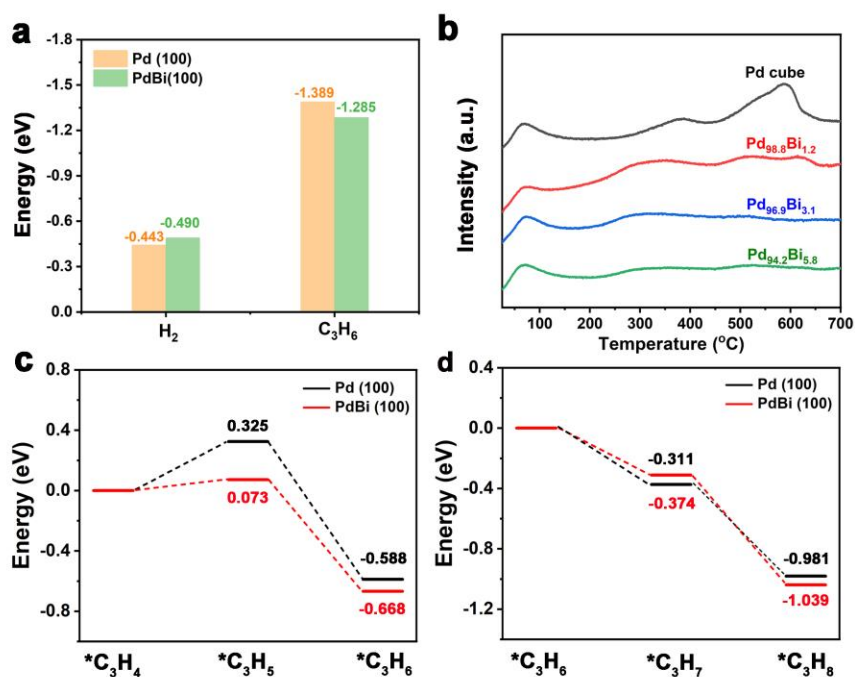


**Figure 5-11. a) DFT simulations of dissociative adsorption energy of hydrogen and adsorption energy of propene on Pd (100) and PdBi (100) surfaces, respectively. b) H<sub>2</sub>-TPD curves of Pd cube and PdBi samples. Energy profile of the first hydrogenation step c) and the second hydrogenation step d) on Pd (100) and PdBi (100) surfaces, respectively.**

was performed on Pd cube and PdBi nanoparticles. As shown in **Figure 5-11b**, hydrogen desorption at low temperature ( $\leq 150$  °C), assigned to the surface adsorbed hydrogen,<sup>45</sup> has little change after Bi insertion. Peaks in the range of 200 to 650 °C should be assigned to hydrogen species dissolved into subsurface layers.<sup>46,47</sup> Those peaks diminish in intensity and shift to a relatively lower temperature compared to that of the Pd cube, which indicates that Bi can efficiently suppress the formation of saturated  $\beta$ -hydrides in subsurface layers and is beneficial to the selectivity toward propene.

The adsorption strength of propene is another factor that determines the degree of hydrogenation. DFT simulation illustrates that the adsorption energy of propene on the PdBi surface is -1.285 eV, which is 0.104 eV weaker than that on the pure Pd surface (-1.389 eV, **Figure 5-11a**), demonstrating that propene can be much easier to desorb from

the surface without subjecting to further hydrogenation. We also simulated the energy profiles of the step-by-step hydrogenation process from propyne to propane to evaluate the effect of inserted Bi on preventing the over-hydrogenation, in which chemical formulas are used to represent the intermediates for convenience and the star (\*) means an adsorbed state. It should be noted that the  $C_3H_4$  on the PdBi surface is much easier to get the first H and hydrogenated to  $*C_3H_6$  (**Figure 5-11c**). However, it becomes harder for the  $*C_3H_6$  to get the second H in the formation of  $*C_3H_7$ , even though the following step from  $*C_3H_7$  to  $*C_3H_8$  is more favorable compared to Pd (100) surface (**Figure 5-11d**). Thus, we can safely conclude that the hydrogenation process on the PdBi surface is prone to halt at the  $*C_3H_6$  state, releasing  $C_3H_6$  molecules subsequently, which is in good agreement with the aforementioned experimental observations.

## 5.4 Conclusions

In summary, we arrive at a PdBi surface alloy structure model by tuning the deposition rate of Bi atoms relative to the atomic interdiffusion rate at the interface. The electronic structure of Pd can be continuously tuned by varying the Bi content in the PdBi alloy, which provides a good platform for systematically analyzing the electronic properties of bimetallic catalysts and underlies the optimization of their catalytic performance. In the selective hydrogenation of propyne, the optimal catalyst exhibits a STY yield of  $124.9 \text{ g}_{C_3H_6} \cdot \text{g}^{-1}_{\text{cat}} \cdot \text{h}^{-1}$ , which is superior to the Pd counterpart, and has a good stability over a 24-hour on-stream test. Practical experiments and theoretical simulations unveil that the insertion of Bi atoms can slightly enhance the H adsorption on the surface but suppress the formation of saturated  $\beta$ -hydrides in the subsurface layers; in the meanwhile, it also weakens the adsorption strength of propene, both contributing to the high propene selectivity. Through careful matching synchrotron capabilities with scientific issues, we have succeeded in determining the structure and electronic properties of the surface PdBi alloy and the bulk Pd in a core-shell structure. This work deepens the understanding of the surface alloy structure and offers new opportunities for the rational design of bimetallic catalysts.

## 5.5 References

- (1) Trotus, I. T.; Zimmermann, T.; Schuth, F. Catalytic reactions of acetylene: A feedstock for the chemical industry revisited. *Chemical Reviews* **2014**, *114* (3), 1761.
- (2) Wehrli, J. T.; Thomas, D. J.; Wainwright, M. S.; Trimm, D. L.; Cant, N. W. Selective hydrogenation of propyne over supported copper catalysts: Influence of support. *Applied Catalysis* **1991**, *70* (1), 253.
- (3) Derrien, M. L. In *Studies in surface science and catalysis*; Elsevier, 1986; Vol. 27.
- (4) Zhang, L.; Zhou, M.; Wang, A.; Zhang, T. Selective hydrogenation over supported metal catalysts: From nanoparticles to single atoms. *Chemical Reviews* **2020**, *120* (2), 683.
- (5) Takht Ravanchi, M.; Sahebdehfar, S.; Komeili, S. Acetylene selective hydrogenation: A technical review on catalytic aspects. *Reviews in Chemical Engineering* **2018**, *34* (2), 215.
- (6) Crespo-Quesada, M.; Cárdenas-Lizana, F.; Dessimoz, A.-L.; Kiwi-Minsker, L. Modern trends in catalyst and process design for alkyne hydrogenations. *ACS Catalysis* **2012**, *2* (8), 1773.
- (7) McCue, A. J.; Anderson, J. A. Recent advances in selective acetylene hydrogenation using palladium containing catalysts. *Frontiers of Chemical Science and Engineering* **2015**, *9* (2), 142.
- (8) Xu, Y.; Bian, W.; Pan, Q.; Chu, M.; Cao, M.; Li, Y.; Gong, Z.; Wang, R.; Cui, Y.; Lin, H.; Zhang, Q. Revealing the active sites of Pd nanocrystals for propyne semihydrogenation: From theory to experiment. *ACS Catalysis* **2019**, *9* (9), 8471.
- (9) Mei, D.; Neurock, M.; Smith, C. M. Hydrogenation of acetylene–ethylene mixtures over Pd and Pd–Ag alloys: First-principles-based kinetic Monte Carlo simulations. *Journal of Catalysis* **2009**, *268* (2), 181.
- (10) Yang, B.; Burch, R.; Hardacre, C.; Headdock, G.; Hu, P. Influence of surface structures, subsurface carbon and hydrogen, and surface alloying on the activity and selectivity of acetylene hydrogenation on Pd surfaces: A density functional theory study. *Journal of Catalysis* **2013**, *305*, 264.
- (11) Park, Y. H.; Price, G. L. Deuterium tracer study on the effect of carbon monoxide on the selective hydrogenation of acetylene over palladium/alumina. *Industrial & engineering chemistry research* **1991**, *30* (8), 1693.



- (12) García-Mota, M.; Bridier, B.; Pérez-Ramírez, J.; López, N. Interplay between carbon monoxide, hydrides, and carbides in selective alkyne hydrogenation on palladium. *Journal of Catalysis* **2010**, *273* (2), 92.
- (13) Lindlar, H. A new catalyst for selective hydrogenation. *Helvetica Chimica Acta* **1952**, *35*, 446.
- (14) Chen, M.; Yan, Y.; Gebre, M.; Ordonez, C.; Liu, F.; Qi, L.; Lamkins, A.; Jing, D.; Dolge, K.; Zhang, B.; Heintz, P.; Shoemaker, D. P.; Wang, B.; Huang, W. Thermal unequilibrium of PdSn intermetallic nanocatalysts: From in situ tailored synthesis to unexpected hydrogenation selectivity. *Angewandte Chemie* **2021**, *133* (33), 18457.
- (15) Shao, L.; Zhang, W.; Armbruster, M.; Teschner, D.; Girgsdies, F.; Zhang, B.; Timpe, O.; Friedrich, M.; Schlogl, R.; Su, D. S. Nanosizing intermetallic compounds onto carbon nanotubes: Active and selective hydrogenation catalysts. *Angewandte Chemie International Edition* **2011**, *50* (43), 10231.
- (16) Feng, Q.; Zhao, S.; Wang, Y.; Dong, J.; Chen, W.; He, D.; Wang, D.; Yang, J.; Zhu, Y.; Zhu, H.; Gu, L.; Li, Z.; Liu, Y.; Yu, R.; Li, J.; Li, Y. Isolated single-atom Pd sites in intermetallic nanostructures: High catalytic selectivity for semihydrogenation of alkynes. *Journal of the American Chemical Society* **2017**, *139* (21), 7294.
- (17) Li, R.; Yue, Y.; Chen, Z.; Chen, X.; Wang, S.; Jiang, Z.; Wang, B.; Xu, Q.; Han, D.; Zhao, J. Selective hydrogenation of acetylene over Pd-Sn catalyst: Identification of Pd<sub>2</sub>Sn intermetallic alloy and crystal plane-dependent performance. *Applied Catalysis B: Environmental* **2020**, *279*, 119348.
- (18) Kang, J. H.; Shin, E. W.; Kim, W. J.; Park, J. D.; Moon, S. H. Selective hydrogenation of acetylene on TiO<sub>2</sub>-added Pd catalysts. *Journal of Catalysis* **2002**, *208* (2), 310.
- (19) Wu, P.; Tan, S.; Moon, J.; Yan, Z.; Fung, V.; Li, N.; Yang, S. Z.; Cheng, Y.; Abney, C. W.; Wu, Z.; Savara, A.; Momen, A. M.; Jiang, D. E.; Su, D.; Li, H.; Zhu, W.; Dai, S.; Zhu, H. Harnessing strong metal-support interactions via a reverse route. *Nature Communications* **2020**, *11* (1), 3042.
- (20) Lee, S.; Shin, S.-J.; Baek, H.; Choi, Y.; Hyun, K.; Seo, M.; Kim, K.; Koh, D.-Y.; Kim, H.; Choi, M. Dynamic metal-polymer interaction for the design of chemoselective and long-lived hydrogenation catalysts. *Science Advances* **2020**, *6* (28), eabb7369.
- (21) Li, X.; Wang, Z.; Zhang, Z.; Yang, G.; Jin, M.; Chen, Q.; Yin, Y. Construction of Au-Pd alloy shells for enhanced catalytic performance toward alkyne semihydrogenation reactions. *Materials Horizons* **2017**, *4* (4), 584.

- (22) Wang, H.; Luo, Q.; Liu, W.; Lin, Y.; Guan, Q.; Zheng, X.; Pan, H.; Zhu, J.; Sun, Z.; Wei, S.; Yang, J.; Lu, J. Quasi Pd<sub>1</sub>Ni single-atom surface alloy catalyst enables hydrogenation of nitriles to secondary amines. *Nature Communications* **2019**, *10* (1), 4998.
- (23) Han, S.; Mullins, C. B. Surface alloy composition controlled O<sub>2</sub> activation on Pd-Au bimetallic model catalysts. *ACS Catalysis* **2018**, *8* (4), 3641.
- (24) Li, X.; Wang, X.; Liu, M.; Liu, H.; Chen, Q.; Yin, Y.; Jin, M. Construction of Pd-M (M = Ni, Ag, Cu) alloy surfaces for catalytic applications. *Nano Research* **2017**, *11* (2), 780.
- (25) Zhou, H.; Yang, X.; Li, L.; Liu, X.; Huang, Y.; Pan, X.; Wang, A.; Li, J.; Zhang, T. PdZn intermetallic nanostructure with Pd-Zn-Pd ensembles for highly active and chemoselective semi-hydrogenation of acetylene. *ACS Catalysis* **2016**, *6* (2), 1054.
- (26) Wang, X.; Figueroa-Cosme, L.; Yang, X.; Luo, M.; Liu, J.; Xie, Z.; Xia, Y. Pt-based icosahedral nanocages: Using a combination of {111} facets, twin defects, and ultrathin walls to greatly enhance their activity toward oxygen reduction. *Nano Letters* **2016**, *16* (2), 1467.
- (27) Huang, D. C.; Chang, K. H.; Pong, W. F.; Tseng, P. K.; Hung, K. J.; Huang, W. F. Effect of Ag-promotion on Pd catalysts by XANES. *Catalysis Letters* **1998**, *53* (3), 155.
- (28) Zou, S.; Lou, B.; Yang, K.; Yuan, W.; Zhu, C.; Zhu, Y.; Du, Y.; Lu, L.; Liu, J.; Huang, W.; Yang, B.; Gong, Z.; Cui, Y.; Wang, Y.; Ma, L.; Ma, J.; Jiang, Z.; Xiao, L.; Fan, J. Grafting nanometer metal/oxide interface towards enhanced low-temperature acetylene semi-hydrogenation. *Nature Communications* **2021**, *12* (1), 5770.
- (29) Cao, M.; Tang, Z.; Liu, Q.; Xu, Y.; Chen, M.; Lin, H.; Li, Y.; Gross, E.; Zhang, Q. The synergy between metal facet and oxide support facet for enhanced catalytic performance: The case of Pd-TiO<sub>2</sub>. *Nano Letters* **2016**, *16* (8), 5298.
- (30) Prieto, J. E.; Markov, I. Thermodynamic driving force of formation of coherent three-dimensional islands in Stranski-Krastanov growth. *Physical Review B* **2002**, *66* (7).
- (31) Zhong, Q.; Feng, J.; Jiang, B.; Fan, Y.; Zhang, Q.; Chen, J.; Yin, Y. Strain-modulated seeded growth of highly branched black Au superparticles for efficient photothermal conversion. *Journal of the American Chemical Society* **2021**, *143* (48), 20513.
- (32) Kwon, S. G.; Krylova, G.; Phillips, P. J.; Klie, R. F.; Chattopadhyay, S.; Shibata, T.; Bunel, E. E.; Liu, Y.; Prakashenka, V. B.; Lee, B.; Shevchenko, E. V.

Heterogeneous nucleation and shape transformation of multicomponent metallic nanostructures. *Nature Materials* **2015**, *14* (2), 215.

- (33) Wang, X.; Luo, M.; Lan, J.; Peng, M.; Tan, Y. Nanoporous intermetallic Pd<sub>3</sub>Bi for efficient electrochemical nitrogen reduction. *Advanced Materials* **2021**, *33* (18), e2007733.
- (34) Chen, W.; Luo, S.; Sun, M.; Tang, M.; Fan, X.; Cheng, Y.; Wu, X.; Liao, Y.; Huang, B.; Quan, Z. Hexagonal PtBi intermetallic inlaid with sub-monolayer Pb oxyhydroxide boosts methanol oxidation. *Small* **2022**, DOI:10.1002/sml.202107803, e2107803.
- (35) Jin, M.; Liu, H.; Zhang, H.; Xie, Z.; Liu, J.; Xia, Y. Synthesis of Pd nanocrystals enclosed by {100} facets and with sizes <10 nm for application in CO oxidation. *Nano Research* **2010**, *4* (1), 83.
- (36) Zhou, M.; Wang, H.; Vara, M.; Hood, Z. D.; Luo, M.; Yang, T. H.; Bao, S.; Chi, M.; Xiao, P.; Zhang, Y.; Xia, Y. Quantitative analysis of the reduction kinetics responsible for the one-pot synthesis of Pd-Pt bimetallic nanocrystals with different structures. *Journal of the American Chemical Society* **2016**, *138* (37), 12263.
- (37) Chen, J.; Yiu, Y. M.; Wang, Z.; Covelli, D.; Sammynaiken, R.; Finprock, Y. Z.; Sham, T.-K. Elucidating the many-body effect and anomalous Pt and Ni core level shifts in X-ray photoelectron spectroscopy of Pt-Ni alloys. *The Journal of Physical Chemistry C* **2020**, *124* (4), 2313.
- (38) Doniach, S.; Sunjic, M. Many-electron singularity in X-ray photoemission and X-ray line spectra from metals. *Journal of Physics C: Solid State Physics* **1970**, *3* (2), 285.
- (39) Wang, X.; Xie, M.; Lyu, F.; Yiu, Y. M.; Wang, Z.; Chen, J.; Chang, L. Y.; Xia, Y.; Zhong, Q.; Chu, M.; Yang, H.; Cheng, T.; Sham, T. K.; Zhang, Q. Bismuth oxyhydroxide-Pt inverse interface for enhanced methanol electrooxidation performance. *Nano Letters* **2020**, *20* (10), 7751.
- (40) Lucci, F. R.; Darby, M. T.; Mattera, M. F.; Ivimey, C. J.; Therrien, A. J.; Michaelides, A.; Stamatakis, M.; Sykes, E. C. Controlling hydrogen activation, spillover, and desorption with Pd-Au single-atom alloys. *Journal of Physical Chemistry Letters* **2016**, *7* (3), 480.
- (41) Lucci, F. R.; Liu, J.; Marcinkowski, M. D.; Yang, M.; Allard, L. F.; Flytzani-Stephanopoulos, M.; Sykes, E. C. Selective hydrogenation of 1,3-butadiene on platinum-copper alloys at the single-atom limit. *Nature Communications* **2015**, *6*, 8550.

- (42) Rieder, K. H.; Baumberger, M.; Stocker, W. Selective transition of chemisorbed hydrogen to subsurface sites on Pd(110). *Physical Review Letters* **1983**, *51* (19), 1799.
- (43) Wilde, M.; Matsumoto, M.; Fukutani, K.; Aruga, T. Depth-resolved analysis of subsurface hydrogen absorbed by Pd(100). *Surface Science* **2001**, *482-485*, 346.
- (44) Teschner, D.; Borsodi, J.; Wootsch, A.; Révay, Z.; Hävecker, M.; Knop-Gericke, A.; Jackson, S. D.; Schlögl, R. The roles of subsurface carbon and hydrogen in palladium-catalyzed alkyne hydrogenation. *Science* **2008**, *320*, 86.
- (45) Khan, N. A.; Shaikhutdinov, S.; Freund, H. J. Acetylene and ethylene hydrogenation on alumina supported Pd-Ag model catalysts. *Catalysis Letters* **2006**, *108* (3-4), 159.
- (46) Witońska, I.; Karski, S.; Frajtak, M.; Krawczyk, N.; Królak, A. Temperature-programmed desorption of H<sub>2</sub> from the surfaces of Pd/support and Pd-Ag/support catalysts (support = Al<sub>2</sub>O<sub>3</sub>, SiO<sub>2</sub>). *Reaction Kinetics and Catalysis Letters* **2008**, *93* (2), 241.
- (47) Conrad, H.; Ertl, G.; Latta, E. E. Adsorption of hydrogen on palladium single crystal surfaces. *Surface Science* **1974**, *41* (2), 435.

## Chapter 6

### 6 Conclusions and Future Work

#### 6.1 Conclusions

This thesis investigates approaches to modifying the surface structure of noble metal-based nanocatalysts. In heterogeneous catalysis, noble metal-based catalysts suffer from the high-cost issue and unsatisfied catalytic performance. Alloying noble metals with cheap metals is one of the solutions to these issues. In this thesis, we use Bi to modify the surface structures of Pt and Pd nanocatalysts. We aim to unveil the role of Bi in improving the catalytic performance of noble metal catalysts both experimentally and theoretically.

In methanol electrooxidation reaction, Pt-based electrocatalysts suffer from the CO-poisoning issue due to the strong intrinsic adsorption of CO at Pt active sites. To alleviate the CO-poisoning effect, Bi was used to modify the Pt catalysts through an electrochemical reconstruction strategy (Chapter 3). It was found that the bismuth hydroxide species formed on the Pt surface can efficiently weaken the CO adsorption while strengthening the OH adsorption at Pt sites. Following this finding, a PtBi model catalyst with a PtBi surface alloy and a Pt-rich core was contrived to further study the roles of Bi in improving the methanol electrooxidation of Pt (Chapter 4). Combining electrochemistry and spectroscopy characterizations, we found that Bi-modified Pt catalysts can completely inhibit the CO-pathway while enhancing the formate-pathway, thereby circumventing the CO-poisoning. More importantly, we have successfully extended this concept to modify the commercial Pt/C catalyst and realize its facile and large-scale production by a microwave-assisted method. This work deepens the understanding of the CO-poisoning issue and offers new opportunities for the design and practical production of CO-tolerance electrocatalysts in an industrial orientation

In selective hydrogenation of propyne, the over-hydrogenation occurring on Pd catalysts is blamed for the poor selectivity toward propene. In Chapter 5, a PdBi surface alloy structural model, by tuning the deposition rate of Bi atoms relative to the atomic

interdiffusion rate at the interface, realizes a continuous modulation of the electronic structure of Pd. Using advanced X-ray characterization techniques, we provide a precise depiction of the electronic structure of the PdBi surface alloy. As a result, the PdBi catalysts show enhanced propene selectivity compared with the pure Pd catalyst in the selective hydrogenation of propyne. The prevented formation of saturated  $\beta$ -hydrides in the subsurface layers and weakened propene adsorption on the surface contribute to the high selectivity. This work emphasizes the in-depth understanding of the electronic properties of surface alloy structure and underlies the study of the electronic structure-performance relationship in bimetallic catalysts.

## 6.2 Future work

Even though extensive work has been focused on the modification of noble metal nanocatalysts and achieves substantial improvements in their catalytic performance, large-scale industrial production is still the biggest obstacle to their widespread applications. From the perspective of cost, it will save a lot by directly modifying presently available commercial catalysts compared to designing new catalysts because there is no necessity to install production equipment again. The surface alloy strategy proposed in this thesis offers opportunities for the large-scale modification of commercial noble metal catalysts, especially with a microwave-assisted method. It is not only applicable to Bi, but can also be extended to other metals, such as Fe, Co, Ni, and Cu, thereby meeting the requirements of different reaction systems.


The successful commercialization of electrocatalysts depends on their performance in real working conditions. Therefore, assembling the full cell is necessary to determine whether the catalysts are suitable for practical applications. The surface alloy concept with a microwave-assisted synthesis method guarantees the facile and large-scale production of catalysts, making it possible to assemble the full cell from the aspect of the required catalyst amount. While this thesis mainly focuses on the fundamental study based on model catalysts, the underlying principles elucidated and strategies developed herein will certainly facilitate their future practical applications.

## Appendices

### Appendix A: Copyright release from ACS publications.


6/26/22, 7:05 PM

Rightslink® by Copyright Clearance Center



[Home](#) | [Help](#) | [Email Support](#) | [Sign in](#) | [Create Account](#)

---



**Bismuth Oxyhydroxide-Pt Inverse Interface for Enhanced Methanol Electrooxidation Performance**

**Author:** Xuchun Wang, Miao Xie, Fenglei Lyu, et al

**Publication:** Nano Letters

**Publisher:** American Chemical Society

**Date:** Oct 1, 2020

*Copyright © 2020, American Chemical Society*

**PERMISSION/LICENSE IS GRANTED FOR YOUR ORDER AT NO CHARGE**

This type of permission/license, instead of the standard Terms and Conditions, is sent to you because no fee is being charged for your order. Please note the following:

- Permission is granted for your request in both print and electronic formats, and translations.
- If figures and/or tables were requested, they may be adapted or used in part.
- Please print this page for your records and send a copy of it to your publisher/graduate school.
- Appropriate credit for the requested material should be given as follows: "Reprinted (adapted) with permission from {COMPLETE REFERENCE CITATION}. Copyright (YEAR) American Chemical Society." Insert appropriate information in place of the capitalized words.
- One-time permission is granted only for the use specified in your RightsLink request. No additional uses are granted (such as derivative works or other editions). For any uses, please submit a new request.

If credit is given to another source for the material you requested from RightsLink, permission must be obtained from that source.

BACK
CLOSE WINDOW

## Curriculum Vitae

**Name:** Xuchun Wang

**Post-secondary Education and Degrees:** Soochow University  
Suzhou, Jiangsu, China  
2009-2013 B.A.

Soochow University  
Suzhou, Jiangsu, China  
2014-2017 M.A.

University of Western Ontario  
London, Ontario, Canada  
2018-2022 Ph.D.

**Related Work Experience**

Teaching Assistant  
The University of Western Ontario  
2018-2019, 2021-2022

Research Assistant  
The University of Western Ontario  
2018-2019, 2021-2022

### Publications:

1. **Wang, Xuchun;** Xie, Miao; Lyu, Fenglei; Yiu, Yun-Mui; Wang, Zhiqiang; Chen, Jiatang; Chang, Lo-Yueh; Xia, Yujian; Zhong, Qixuan; Chu, Mingyu; Yang, Hao; Cheng, Tao; Chen, Jinxing; Sham, Tsun-Kong; Zhang, Qiao. Bismuth oxyhydroxide-Pt inverse interface for enhanced methanol electrooxidation performance. *Nano Letters* **2020**, 20 (10), 7751.
2. **Wang, Xuchun;** Liu, Yu; Ma, Xingyu; Chang, Lo-Yueh; Zhong, Qixuan; Pan, Qi; Wang, Zhiqiang; Yuan, Xiaolei; Yang, Yaoyue; Zhang, Qiao; Chen, Jinxing; Sham, Tsun-Kong. The Role of Bismuth in Suppressing the CO-poisoning in Alkaline Methanol Electrooxidation: Switching the Reaction from the CO to Formate Pathway. **2022**. (In preparation)
3. **Wang, Xuchun;** Chu, Mingyu; Wang, Mengwen; Zhong, Qixuan; Chen, Jiatang; Wang, Zhiqiang; Cao, Muhan; Yang, Hao; Cheng, Tao; Zhang, Qiao; Chen, Jinxing; Sham, Tsun-Kong. Unveiling the Local Structure and Electronic Properties of PdBi Surface Alloy for Selective Hydrogenation of Propyne. **2022**. (In preparation)



4. Zhong, Qixuan; **Wang, Xuchun**; Chu, Mingyu; Qiu, Yinghua; Yang, Di; Sham, Tsun - Kong; Chen, Jinxing; Wang, Lu; Cao, Muhan; Zhang, Qiao. Ultra - Stable CsPbX<sub>3</sub>@ Pyrophosphate Nanoparticles in Water over One Year. *Small* **2022**, *18* (13), 2107548.
5. Chu, Mingyu; Huang, Jialu; Gong, Jin; Qu, Yi; Chen, Guoling; Yang, Hu; **Wang, Xuchun**; Zhong, Qixuan; Deng, Chengwei; Cao, Muhan; Chen, Jinxing; Yuan, Xiaolei; Zhang, Qiao. Synergistic combination of Pd nanosheets and porous Bi(OH)<sub>3</sub> boosts activity and durability for ethanol oxidation reaction. *Nano Research* **2022**, *15* (5), 3920.
6. Xu, Yong; **Wang, Xuchun**; Yang, Di; Tang, Zeyuan; Cao, Muhan; Hu, Huicheng; Wu, Linzhong; Liu, Lijia; McLeod, John; Lin, Haiping; Li, Youyong; Lifshitz, Yeshayahu; Sham, Tsun-Kong; Zhang, Qiao. Stabilizing Oxygen Vacancies in ZrO<sub>2</sub> by Ga<sub>2</sub>O<sub>3</sub> Boosts the Direct Dehydrogenation of Light Alkanes. *ACS Catalysis* **2021**, *11* (16), 10159.
7. Jiang, Xiaojing; Chen, Jianian; Lyu, Fenglei; Cheng, Chen; Zhong, Qixuan; **Wang, Xuchun**; Mahsud, Ayaz; Zhang, Liang; Zhang, Qiao. In situ surface-confined fabrication of single atomic Fe-N<sub>4</sub> on N-doped carbon nanoleaves for oxygen reduction reaction. *Journal of Energy Chemistry* **2021**, *59*, 482.
8. Chu, Mingyu; Liu, Yu; Gong, Jin; Zhang, Congyang; **Wang, Xuchun**; Zhong, Qixuan; Wu, Linzhong; Xu, Yong. Suppressing Dehydroisomerization Boosts n - Butane Dehydrogenation with High Butadiene Selectivity. *Chemistry–A European Journal* **2021**, *27* (45), 11643.
9. Hu, Huicheng; Guan, Wenhao; Xu, Yafeng; **Wang, Xuchun**; Wu, Linzhong; Chen, Min; Zhong, Qixuan; Xu, Yong; Li, Youyong; Sham, Tsun-Kong; Zhang, Xiaohong; Wang, Lu; Cao, Muhan; Zhang, Qiao. Construction of Single-Atom Platinum Catalysts Enabled by CsPbBr<sub>3</sub> Nanocrystals. *ACS Nano* **2021**, *15* (8), 13129.
10. Zhang, Yong; Yuan, Xiao-Lei; Lyu, Feng-Lei; **Wang, Xuchun**; Jiang, Xiao-Jing; Cao, Mu-Han; Zhang, Qiao. Facile one-step synthesis of PdPb nanochains for high-performance electrocatalytic ethanol oxidation. *Rare Metals* **2020**, *39* (7), 792.
11. Xu, Yong; Chu, Mingyu; Liu, Fangfang; **Wang, Xuchun**; Liu, Yu; Cao, Muhan; Gong, Jin; Luo, Jun; Lin, Haiping; Li, Youyong; Zhang, Qiao. Revealing the correlation between catalytic selectivity and the local coordination environment of Pt single atom. *Nano Letters* **2020**, *20* (9), 6865.
12. Xu, Yong; **Wang, Xuchun**; Cheng, Liang; Liu, Zhuang; Zhang, Qiao. High-yield synthesis of gold bipyramids for in vivo CT imaging and photothermal cancer therapy with enhanced thermal stability. *Chemical Engineering Journal* **2019**, *378*, 122025.

**Presentations:**

1. “Facile synthesis of Pt-Bi nanoparticles and their applications in direct methanol fuel cells (DMFCs)” Poster Presentation, 102nd Canadian Chemistry Conference and Exhibition, Quebec City, QC, Canada, June 2019.